Chapter 2
Investigations of the Water Body Biogeochemistry and Phytoplankton Biomass Variability in Time and Space

2.1 Atlantic Ocean

2.1.1 Bay of Biscay

2.1.1.1 General Characteristics

The Bay of Biscay is a gulf of the northeast Atlantic Ocean lying along the western coast of France from Brest southwards to the Spanish border, and the northern coast of Spain in the Spanish Basque Country. Its limits are defined as a line joining Cap Ortegal (43° 46′N, 7° 52′W) to Penmarch Point (47° 48′N, 4° 22′W) (International Hydrographic Organization 1971).

Extending far into the Bay, the continental shelf causes rough seas, for which the region is known, being the arena of severe storms, especially during late autumn–early spring. The ecosystem of the pelagic region of the Bay sustains numerous species of whales and dolphins as well as fish such as sardine and mackerel, which play a significant role in the French and Spanish fishing industries (ICES 2010).

The Bay's coastline is highly diversified with estuaries, rias, and wetlands, which all support extremely productive ecosystems. The coastal strip has an increasing high population density. Industries of various types, agriculture, and other land-based activities are located along the coasts. The main human activities in the region include, among others, tourism, fishing and aquaculture, shipping, sand and gravel extraction, and the new developments of wave, tide, and wind power generation.

The Bay's bathymetry pre-determines two distinct areas. The one adjoining the land constitutes the shelf zone and is separated from the pelagic zone by the 200 m isobath: it is about 160 km wide off the coast of Brittany but narrows down to less than 65 km off the Spanish shore (see Fig. 2.1). The edge of the shelf and the

D. Pozdnyakov et al., *Exploring the Marine Ecology from Space*,
Springer Remote Sensing/Photogrammetry,
DOI 10.1007/978-3-319-30075-7_2

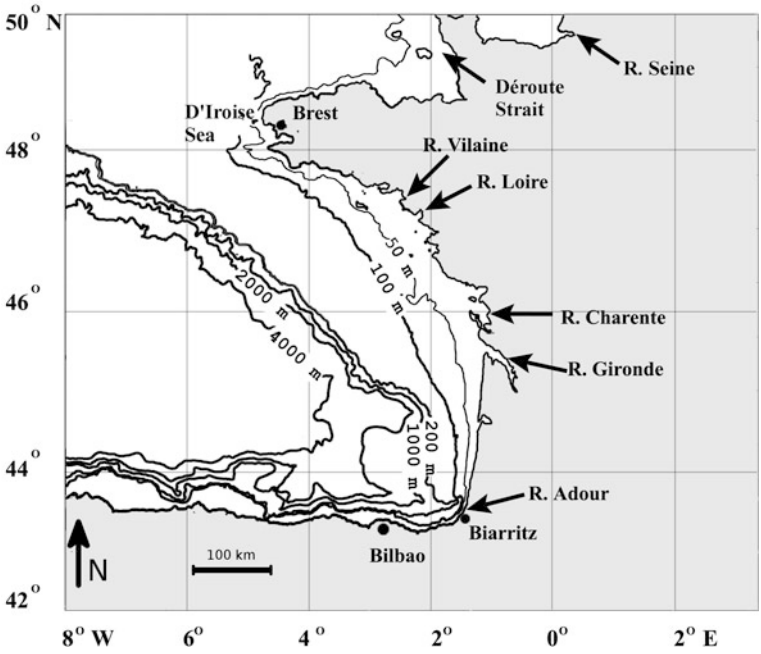

Fig. 2.1 Bathymetric map of the Bay of Biscay (wikipidea.org)

continental slope are dissected by numerous submarine canyons. Beyond the continental slope, lies the Biscay Abyssal Plain with depths of about 4550 m, which occupies about half the area of the Bay.

The hydrological (and also biogeochemical) properties inherent in shelf and pelagic regions differ from each other significantly. The gently sloping shelf zone is the area that is subject to river discharge seasonal variations, determining the input of suspended minerals and nutrients as well as fresh water (Tyrrell and Merico 2004; Guillaud et al. 2008). The main rivers flowing into the Bay from the French coast are the Vilaine, Loire, Charente, and Gironde (a confluence of the Garonne and Dordogne Rivers), accounting for $\sim$60% of the total terrigenous suspended matter deposited within the shelf zone, and Adour. The rivers bringing their waters from the Spanish coast are Bidasoa, Urola, Nevron, Pas, Deva, Nalon, Navira, and Sor. The Loire and Gironde are the most full-flowing rivers (Lampert et al. 2002).

This zone experiences strong tide-driven water motions and sea-level variations (3.5 m at Biarritz up to 6 m near Brittany). Frequent strong winds result in bottom sediment resuspension and upwellings in the vicinity of the French Brittany coast and the Spanish Finisterre Cap (42° 52′ 57″N, 9° 16′ 20″E), and in summer, between southern Brittany and the Landes coast in the far south west of France (Puillat et al. 2004). With the exception of autumn, when the horizontal movements are oriented from north to south, the water circulation patterns in other seasons are

predominantly directed from south to north (Castaing et al. 1999; Rodriguez et al. 2003). Although the thermal regime in this zone is spatially and temporally highly variable, there is an annually recurrent thermohaline front (100 km wide in the north and only 50 km wide to the west of the Gironde estuary) forming up in winter (November/December) and persisting through half of spring (till mid-April) and extending over the 100 m isobath on the opposite side of the Gironde Estuary. This front is a barrier for the transport of terrigenous suspended matter, retaining up to 65% of the suspended matter either re-suspended or coming from land (Castaing and Allen 1981).

2.1.1.2 Remote Sensing Observations

Within the shelf zone (Fig. 2.1), our satellite-borne data (Morozov et al. 2012) [processed with our NN algorithm, see Chap. 1] confirm the findings of numerous previous reports (e.g. Garcia-Soto and Pingree 2009) that there are two major phytoplankton blooms in the study area—in spring and in autumn.

Figure 2.2 illustrates the temporal variations in the spatial distribution of monthly mean *chl* and *tsm* concentrations across the Bay's shelf zone around the year (Morozov et al. 2012). The year 2001 was chosen for illustration because the cloudiness conditions were such that we could observe most amply the wintertime re-suspension events. There are a number of plume-like features in the distribution of both *chl* and *tsm* with the concentrations varying in large ranges: 13–4 and 15–5 mg l^{-1}, respectively. These plumes originate from the estuaries of rivers discharging into the Bay: moving from north to south, these are the Vilaine, Loir, Gironde, and Adour (see Fig. 2.1). An important difference between the two distributions in Fig. 2.2 is the extent of plumes off the coastline: *tsm* plumes are more restricted to the respective estuaries (not exceeding 100 km), whereas *chl* plumes practically reach the outer boundary of the coastal/shelf zone (i.e. almost the lay of the 200 m isobath). This is easily explainable: suspended matter (mostly mineral) brought in with riverine waters settles down in the relative vicinity of the estuary due to gravitational sedimentation, whereas *chl* plumes rise from the dissolved river-borne nutrients that are not subject to physical removal from the water column (Pozdnyakov and Grassl 2003). In June, these distinguishing features become further accentuated as the aftermath of the highest phase of river discharge.

Further off-coast, the impact of river discharge rapidly declines. A pairwise comparison of the panels in Fig. 2.2 immediately reveals the seasonal variations in the river discharge: in May (the month of highest river discharge in the area), *chl* and *tsm* plumes extending off the coast (up to distances of 100–120 and 50–100 km, respectively) are most intense; contrarily, in July, when the river discharge is low, *chl* and *tsm* plumes are practically restricted to the estuaries of the rivers. For all this, *chl* plumes, however, extend over a slightly larger area than *tsm* plumes (e.g. about 150 km for *chl* against 100 km *tsm* for Loire river), which is in accordance with the above argument. The retrieved sequence of *chl* spatial distributions throughout the vegetation season reveals a rather slight secondary

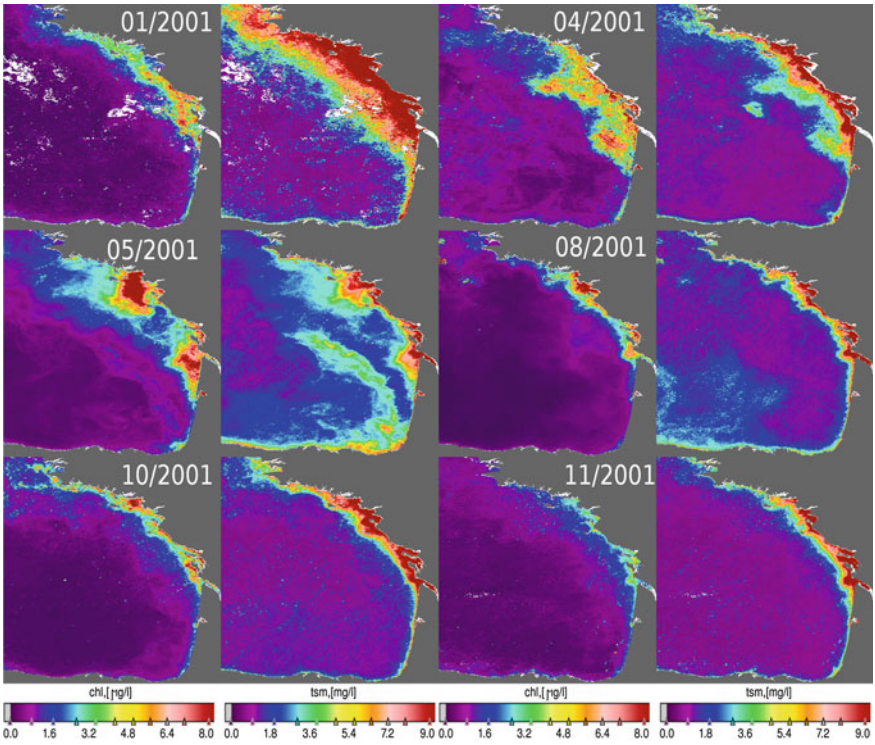

Fig. 2.2 Spatio-temporal variations in the extent and intensity of *chl* blooms and *tsm* plumes across the shelf zone of the Bay of Biscay as retrieved with our NN-based algorithms from data registered by SeaWiFS in 2001

maximum of the phytoplankton growth cycle in autumn (October, with *chl* concentrations in local areas up to 8–10 μg l^{-1}), which falls in line with the reported in situ data (Lavender et al. 2008).

In January, the river discharge in this area is the highest, *tsm* plumes are most pronounced, whereas the water temperature derived from AVHRR (10–12 °C across most of the shelf zone, AVHRR) and Sun illumination conditions are unfavorable for the growth of ingenious phytoplankton.

Thus, the SeaWiFS- and MODIS-based products developed by us for *chl* and *tsm* yield the spatial distributions of these water constituents in complete consistency with the intrinsic phenomenology of the Bay of Biscay, which substantiates their performance efficiency and lays down the foundation for merging and bridging of data from these ocean colour sensors.

The bridging performed and the time series developed (Fig. 2.3a, b) are substantiated by veritably high correlation coefficients between the retrieved and in situ match-ups for *chl* and *tsm* as well as by taking into account the mean absolute error

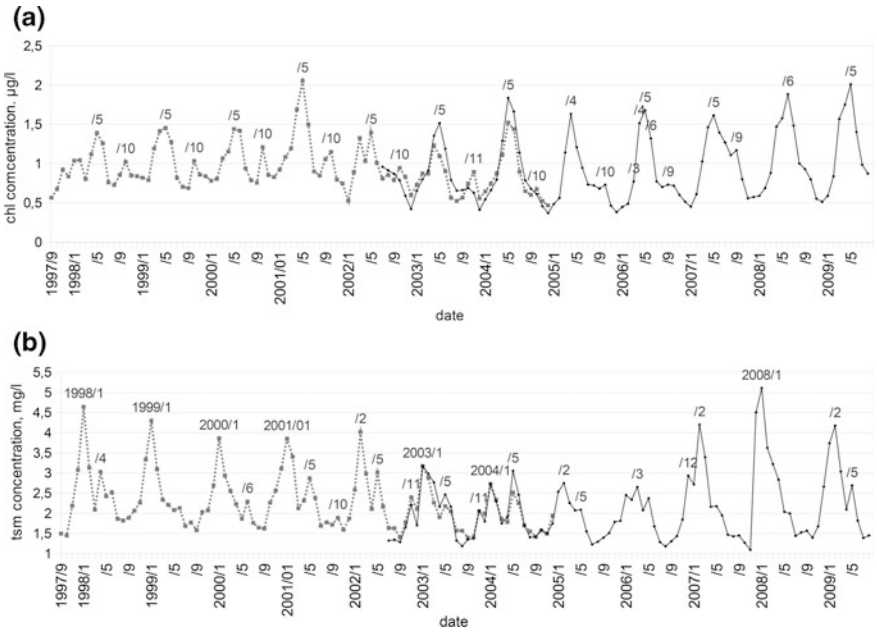

Fig. 2.3 Two overlapping time series of monthly mean concentrations of **a** *chl* (µg l^{-1}) and **b** *tsm* (mg l^{-1}) retrieved from SeaWiFS (*dashed line*) and MODIS (*solid line*) data with our NN algorithms and averaged over the shelf zone of the Bay of Biscay

and correlation coefficients for the overlapping time period (July 2002–December 2004), which proved to be, respectively, 18.42 and 0.91% for *chl*, and 8.63 and 0.93% for *tsm* (Morozov et al. 2012).

The bridged SeaWiFS–MODIS data on the monthly mean concentrations of *chl* and *tsm* within the shelf zone for the period 1997–2009 reveal (see Fig. 2.3a) some notable features. First and foremost, there are two distinct patterns in the functioning of the ecosystem: the first (lasting between 1997 and 2003) is characterized by a slow decline in primary productivity, which, as we point out in the introductory section, can be characterized by its proxy, i.e. concentration of *chl* (approximately—0.36 µg *chl* l^{-1} per 6 years), while during 2004–2009 the trend switches to a positive value of about +0.58 µg *chl* l^{-1} per 5 years.

The prevailing pattern (see Fig. 2.3b) of the *tsm* time series resembles in general lines that of *chl* (see Fig. 2.3a) during the period 1997–2009: there was a span of time (2003–2006) characterized by an appreciable slowing down in the input of *tsm* in the shelf zone. Further on, this feature was replaced by a rapid intensification of *tsm* supply, which, like in the case of *chl* (see Fig. 2.3a), eventually took the form of steadily building up notable seasonal oscillations (*tsm* maximum winter concentrations started to increase rather dramatically from 2.7–3.1 up to 4–5 mg l^{-1}, whereas *tsm* summer minimum concentrations began to decrease from 1.2–1.9 to 1.1–1.4 mg l^{-1}). The driving reason for the observed impoverishment in *chl* and

tsm is the same: it is known from coastal gauge records (HYDRO—Les principaux services proposés, available at: http://www.hydro.eaufrance.fr/) that in 2002 there was a significant drop in river discharge, which lasted up to about 2005 (with the exception of 2004). This regards, first and foremost, the full-flowing Rivers Loire, Dordogne, and Garonn. Figure 2.4a, b illustrate, with River Dordogne as an example, how closely the annually integrated *chl* and *tsm* concentrations follow the pattern of river discharge.

However, in interannual monthly mean variations, the aforementioned similitude between *chl* and *tsm* temporal variation patterns is only general: they significantly differ in details, which stems from respective underpinning processes. As Fig. 2.3a, b show, the *chl* abundance recovery in the shelf zone starts in 2004, whereas in the case of *tsm* it occurs much later, in 2007. Somavilla et al. (2009) attribute the *chl* concentration increase after 2004 to a profound transformation of the upper ocean hydrographic structure of the Bay of Biscay area: the strong winter cooling (water column between 200 and 300 dbar (2×10^6 and 3×10^6 Pa) cooled by about 0.5 °C) in 2004 caused an extreme buoyancy loss that, in turn, made the mixed layer reach exceptionally (at least since the 1960s) significant depths (well below 300 dbar), whereas in the whole series it seldom surpasses the 200 dbar level. In turn, the enhanced mixing resulted in nutrient enrichment of the upper waters due to the upward vertical transfer of nutrient-rich deep water. Further in spring, this enrichment drove the observed intense phytoplankton growth. Thus, the *chl* variation pattern, at least in 2004–2005, was controlled not solely by the river run-off nutrients input, but also by atmospheric forcing and the ensuing bringing up of nutrient-rich deep waters. At the same time, unlike the case with *chl*, the *tsm* pattern was dictated mainly by river discharge interannual variations.

A closer inspection of Fig. 2.3a, b reveals some details, which are also worth of consideration. For instance, Fig. 2.3a demonstrates that although the two major peaks in *chl* (as high as 1.4–2.5 μg l^{-1}) across the year occur generally in May and October (respectively, the major and secondary ones), but in 2008 the *chl* peak (1.88 μg l^{-1}) occurred in June with a strong shoulder in May. Similar features are discernible in the space-borne data for 2006 and in 2003. In 2004, the main *chl* peak

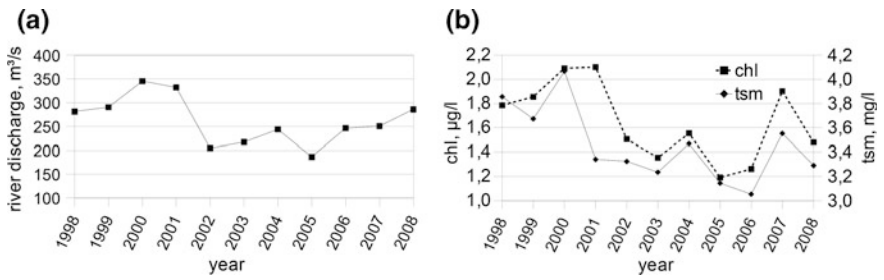

Fig. 2.4 Mean annual variations in **a** the Dordogne River discharge rate (m^3 s^{-1}) and **b** *chl* (*solid diamonds*) and *tsm* (*dashed squares*) concentrations (μg l^{-1} and mg l^{-1}, respectively) within the southern part of the shelf zone of the Bay of Biscay

(1.84 μg l^{-1}) is not preceded but followed by a strong shoulder. Analyses of contemporaneous AVHRR and MODIS as well as QuikSCAT data (see Fig. 2.5a, b) allowed us to explain the observed features falling out of the general regularity. In June of the above years, strong (~6–8 m s^{-1}) and very steady westerly to northwesterly winds (see prevailing winds in the inset in Fig. 2.5b) led to the formation of upwellings along the northern part of the Bay's coast (see the SST field in Fig. 2.5a), which are known to enrich the upper layers with nutrients (Puillat et al. 2004). The latter brought about some outbursts of phytoplankton growth (see Fig. 2.5b). Depending on the intensity and timing of the upwellings, the *chl* peak occurs either after or before May.

The *chl* autumnal peak (typically 0.8–1.2 μg l^{-1} and on average 1.0 μg l^{-1}) regularly occurring in October in some years is expressed in September, which must be due to temporal excursions of the month of highest precipitation in the fall (Lavender et al. 2008).

Some irregular features are also present in Fig. 2.3b, in particular, in 2005, 2006, 2007, and 2009 the *tsm* main peak (on average ~3.8 mg l^{-1}) occurred not in January as regularly happened in previous years but in February, and even in March (2006). The contemporaneous wind fields derived from QuikSCAT data (exemplified in Fig. 2.6 for 2007) indicate that in February 2006, 2007, and 2009 and in March 2006 there were strong winds (10–15 m s^{-1} and even higher) in the immediate vicinity of the Bay's coast. Such strong winds are known to provoke extensive zones of bottom sediment re-suspension (Froidefond et al. 2002). The latter can result in more enhanced *tsm* concentrations than those arising from the wintertime river run-off: the effect, which we observe in Fig. 2.4b.

It is noteworthy that the off-coastal extent of re-suspension-driven *tsm* plumes are not extended offshore as far as it could be expected from the near-surface wind force field (e.g. exemplified in Fig. 2.6). Obviously, this is due to the thermohaline front that is established during this time of year determines the light regime in the water column and hence it influences the biogeochemical processes developing in spring and summer. At the same time, a shipborne study in the Bay of Biscay, notorious for very hard cruising conditions, specifically in winter, and is seriously hampered. As shown above, the application of merged ocean colour data can be very useful, possibly offering the only efficient way of surveying and studying this phenomenon in terms of its spatial extent and duration.

Before leaving this part of the results discussion, it seems noteworthy to mention that the patterns of *chl* and *tsm* temporal variations depend on the area of integration. As Fig. 2.7 (upper and middle curve) illustrates, *chl* plots drawn separately for the northern (area 3) and southern (area 2) French provinces of the Bay differ, which is interpreted in terms of river discharge rates and area-specific temporal variations inherent in both provinces: the northern provinces are recipients of most full-flowing rivers, whereas the rivers flowing in the southern coastal zone are water-short. Figure 2.7 (lower curve) displays similar plots for the Spanish coastal zone (area 1). It is obvious that, first, the Spanish shelf zone is appreciably less productive in comparison with the French zone 2, and secondly, the *chl* main blooms occur there on average prior (by 1.5–2 months) to the timing of northern

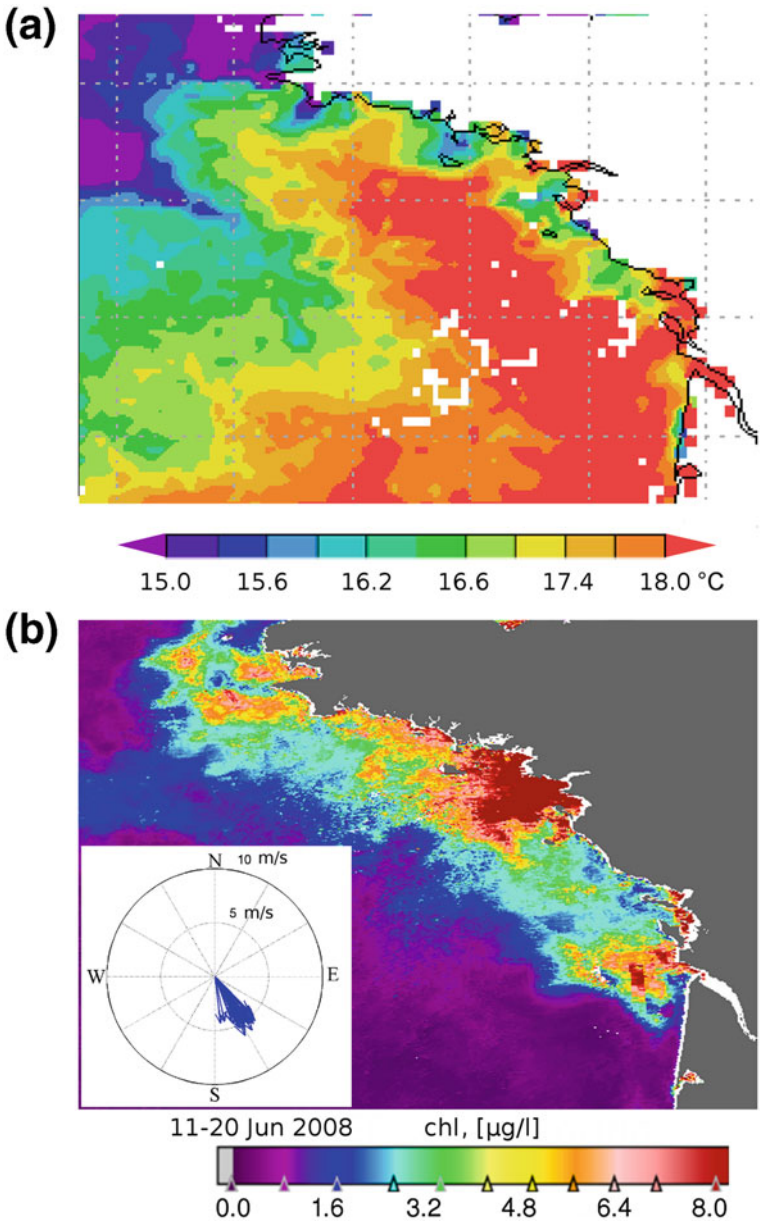

Fig. 2.5 Coastal wind-driven upwelling at the northeastern shore of the Bay of Biscay in June 2008. **a** Monthly mean MODIS SST (°C) (Giovanni online data system) and **b** *chl* concentration ($\mu g\ l^{-1}$) temporal average for 11–20 June 2008. In the *inset*: mean wind for each pixel in the upwelling area for 1–15 June 2008 as recorded by QuikSCAT in June 2008

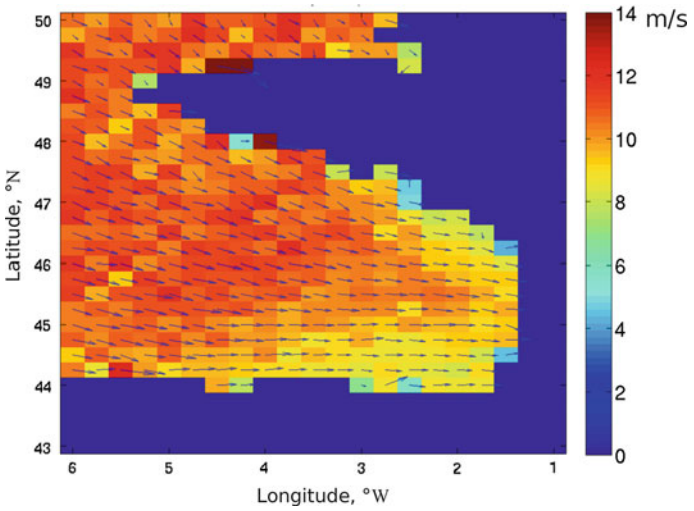

Fig. 2.6 Mapped mean monthly wind vector and prevailing direction for the February 2007, based on QuikSCAT data

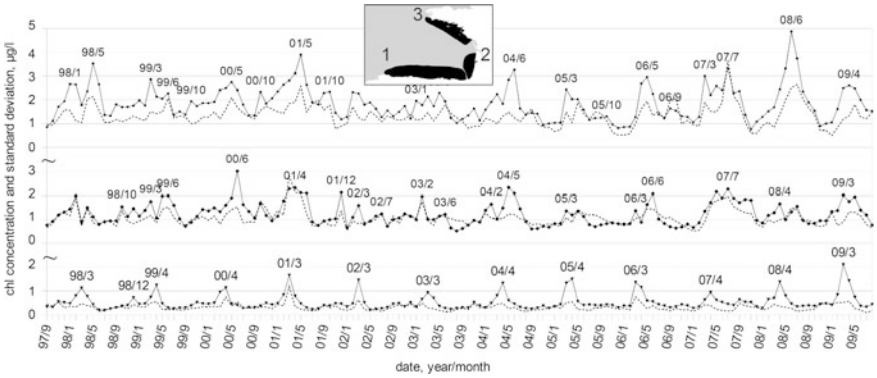

Fig. 2.7 Time series of monthly mean *chl* concentrations (µg l^{-1}) for areas 1, 2, and 3 (*lower*, *middle*, and *upper curve*, respectively) of the Bay of Biscay. In the *inset*: location of areas 1–3

blooms. This time shift decreases as we move from area 1 to area 2 and finally to area 3.

The decline in primary productivity (that is *chl*, as a proxy of productivity) and its duration are becoming respectively less expressed and progressively shortened when moving from area 3 to area 1 (see Figs. 2.7 and 2.8): the *chl* concentration and bloom duration as assessed from space constitute on average 0.53, 1.24, and 1.27 µg l^{-1}, and 3 months, 2 months and 1 month for areas 1, 2, and 3, respectively. The observed progressive dissimilitude is thought to be due to variations in discharge rates of the rivers flowing in areas 1, 2, and 3 as well as the specific

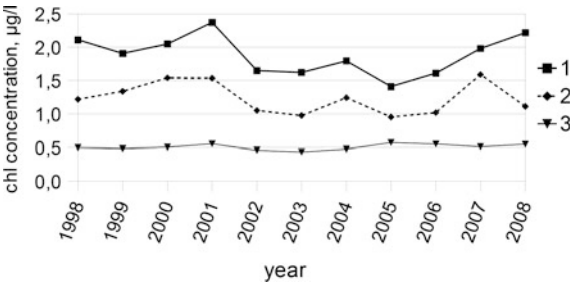

Fig. 2.8 Time series of annual mean *chl* concentrations (µg l^{-1}) for areas 1, 2, and 3 (*lower*, *middle*, and *upper curves*, respectively) of the Bay of Biscay. For locations of areas 1–3, see the *inset* in Fig. 2.7

thermal regime inherent in these areas (Gonzalez-Pola et al. 2005). These findings with respect to area 1 are in compliance with the results of the study conducted along the Santander section, located within the southern part of the Bay of Biscay (Somavilla et al. 2009). Figure 2.7 also illustrates the variations of the spatial standard deviation of monthly mean pixel values, s_{chl}, which characterizes the degree of *chl* data spatial homogeneity. For the entire period considered, the value of s_{chl} normalized to *chl* $\left(\sum_n (s_{chl}[chl])/n\right)$, where n is the length of monthly means time series proved to be 0.68, 0.71, and 0.93 for areas 1, 3, and 2, respectively.

2.1.2 Adriatic Sea

2.1.2.1 General Characteristics

Located between the Italian and Balkan peninsulae, the Adriatic Sea (~40°N to ~46°N, 12°E–20°E) is the northernmost arm of the Mediterranean. It is elongated in the NW-SE direction (the maximum length is 800 km) and should be rather classified as a semi-enclosed basin: only a fairly narrow Strait of Otranto (72-km wide) in the south separates it from the Ionian Sea Fig. 2.9. The average depth is about 250 m, but there are two pits (in mid-and south-Adriatic) where it significantly exceeds 1 km (Fig. 2.10). The surface area is about 140 thousand square kilometers, and the shore length is ~3.7 thousand kilometers (Sailot 2005).

Inflowing through the Strait of Otranto (located over the Otranto Sill, an underwater ridge) and further propagating along the eastern coast, the Mediterranean seawater constitutes a stable cyclonic circulation throughout the sea: it encompasses both surface and benthic currents, the later being most pronounced along the western coast of the sea. Upon entering the Adriatic Sea, the cyclonic current heads to the Bosnian coast, where it disintegrates: one brunch turns left to eventually follow the Italian coast, while the remaining flow circumvents the Croatian archipelago moving further to the north till the Gulf of Venice, turns left to join the mainstream of the cyclonic flow along the Italian coast. It is worth mentioning that in the Gulf of Venice there are paired small-scale cyclonic and anti-cyclonic circulations resulting in the formation of eddies (Sailot 2005).

Fig. 2.9 Map of the Adriatic Sea (wikipidea.org)

Tidal movements in the Adriatic are generally slight but occasionally happen to be very significant (Fain et al. 2007).

Due to low jaggedness of the Italian coast, the Western Adriatic Current has a smooth flow, which at the surface is constituted by relatively freshwater mass,

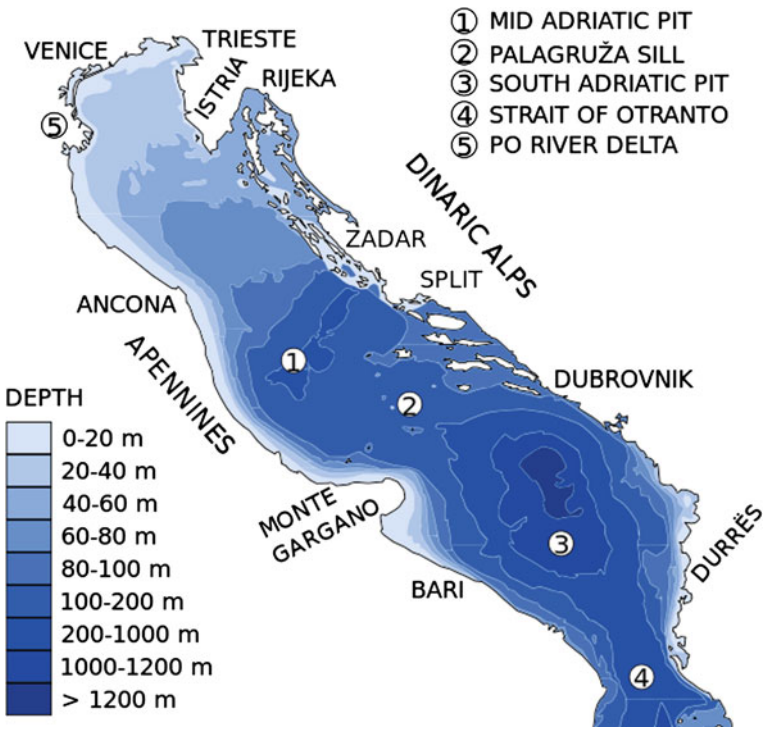

Fig. 2.10 The bathymetry of the Adriatic Sea (wikipidea.org)

whereas at the bottom the current is a cold and dense water mass. Closer to the coastal zone, there is a permanent coastal jet (Sailot 2005).

A salient feature of the western and northern coastal zone topography is an extensive shallow seafloor with depths less than 20 m. In some parts of the Adriatic shelf they form habitats for coralligenous outcrops, maeri (corrollines of loose-lying branches), Posidonia (seaweeds), Cystoseria (brown macroalga) (Martin et al. 2014). These communities are important elements of the marine ecosystem (Giakoumi et al. 2012) and their protection/conservations is one of the serious concerns of ecologists (e.g. Fraschetti et al. 2001; Airoldi and Beck 2007).

Contrarily, the eastern coastline by itself is far more indented and hence significantly less smooth, besides it incorporates a large number (more than one thousand) of islands ranging in size from large ones to islets. Due to strong water temperature gradients arising between the riparian strand and seawater, there is a formation of sustained local jets with a cyclonic direction of propagation towards to Croatia.

Both jets on the western and eastern sides of the Adriatic play important roles not solely in the coastal hydrology but also in the biogeochemistry of the marine environments (Fain et al. 2007).

The freshwater inflow to the Adriatic comes from two sources. Submarine springs constitute important input of freshwater into the Adriatic. It is assessed at 29% of the total fresh water flux. However the prime sources are river runoffs. The Adriatic is a recipient of many rivers (Fig. 2.11). The main inflows of fresh water on

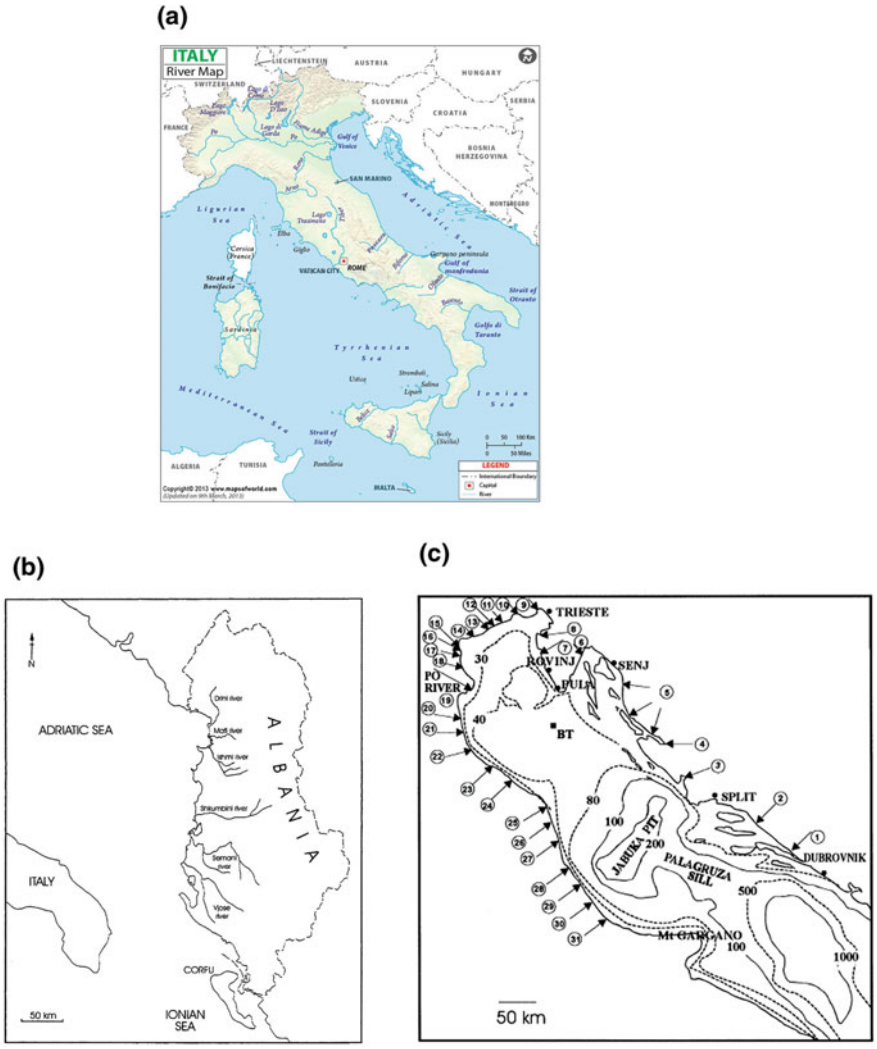

Fig. 2.11 Main rivers discharging in the Adriatic on the western (**a**) and eastern (**b**) coasts. Numbers in (**c**) stand for the following rivers (Paklar et al. 2001): *1* Neretva; *2* Cetina; *3* Krka; *4* Zrmanja; *5* Zrmanja to Rijeka Bay; *6* Rasa; *7* Mirna; *8* Dragonja; *9* Sosca; *10* Stella; *11* Tagliamento; *12* Livenza; *13* Piave; *14* Sile; *15* Brenta; *16* Agno-Gua; *17* Adige; *18* Canal Bianco; *19* Po; *20* Reno; *21* Lamone to Savio; *22* Po to Marechia; *23* Foglia; *24* Marecchia to Tronto; *25* Tronto; *26* Pescara; *27* Sangro; *28* Trigno; *29* Biferno; *30* Fortore; *31* Vibrata to Fortone

the western coast are Rivers Po, Adige, Pescara, Ofanto with a mean discharge rate of 1569; 200; ~46, and ~12 $m^3 s^{-1}$, respectively, and on the eastern coast—Rivers Vijose, Semani, and Shkumbini, Mati with the mean discharge, respectively, 145, ~38, 35 $m^3 s^{-1}$ but also Mirna, Krka, Cetina, Zrmanja with the respective discharge rates of 7.6; 53.4; 3 2,0; 37.6 (Ludwig et al. 2009; Parlar et al. 2001; Ciavola et al. 1999; Surian and Rinaldi 2003). In addition to full-flowing rivers, the Adriatic Sea is recipient of many rivers of smaller outflow both on the west-northern and the eastern coasts. (The entire climatological discharge rates of outfalling rivers at the end of the previous century were assessed at ~3000 $m^3 s^{-1}$ (Paklar et al. 2001; Fain et al. 2007; Ludwig et al. 2009)).

Notwithstanding the recorded significant interannual variations in this value (the recent ten years are marked by rendering the Adriatic climate more dry (Cozzi and Giani 2011)), the outfall of fresh water reduces the water salinity in the Adriatic so that this sea acts as a dilution basin for the Mediterranean.

Rivers discharging into the Adriatic on the western coast form its alluvial or terraced status. Contrarily, pronounced karstification is the reason of the highly indented line of the eastern coast: the eastern shores are predominantly rocky, except for the southernmost part of the shore located in Albania that consists of sandy coves and rocky capes.

Because of the water flows entering through the Strait of Otranto bring clear waters from the pelagic Mediterranean and a significant paucity of anthropogenic pressing, the eastern coast is appreciably less polluted and the inherent waters are appreciably clear. Being drawn by the prime counterclockwise circulation to the north along the coast and then turned southward along the Italian coast (with many cities and discharging rivers), the initially clear waters gradually accumulate all incoming admixtures becoming more polluted and turbid.

The climate of the Adriatic Sea and its catchment is a type of subtropical climate exhibiting a well-expressed seasonal variability: it is characterized by warm to hot dry summers and mild to cool wet winters. The air temperature fluctuates around 20 °C across the year. The predominant winter winds are the bora and sirocco. Coming to the northern Adriatic, the bora brings cold and dry continental air and may have peak speeds up to 180 km h^{-1}. The sirocco brings humid and warm air, often carrying Saharan sand causing rain dust (Cushman-Roisin et al. 2013; Fain et al. 2007).

2.1.2.2 Adriatic Sea: Ecological Challenges

Within the area of the Adriatic Sea, the natural environments, both aquatic and riparian terrestrial, are known for their remarkable, and in some cases, unique features. The geographical location of the sea, the watershed orography, bottom topography, hydrodynamic and hydrobiochemical communication with the Mediterranean as well as many other factors give rise to a great abundance and diversity of endemic flora and fauna. More than seven thousand animal and vegetation species are identified in the Adriatic Sea (Bianchi and Morri 2000).

The fish fauna is particularly diverse in the Northern Adriatic. Karst morphology, bottom relief, karst rivers, fresh water springs offer perfect habitats for fish with at least seven species endemic to the Adriatic.

The fluvial and terraced bottom along the western Italian coast determines the importance of this part in terms of both hydrobiology and tourist industry (Sailot 2005).

It is recognized that this natural environmental richness of the Adriatic Sea system requires protection against external forcing. Indeed, the Adriatic riparian area is populated by more than 3.5 million with large cities: the largest cities (first and foremost, Bari, Venice, Trieste and Split) are located on both sides of sea (Colombo 1992).

Waste water from cities, excessive fisheries and ever growing tourism, increasing marine transport and 19 seaports in the Adriatic as sources of ballast water discharge and occasionally oil spills, excessive inputs of nutrients due to both drainage from farming territories and river discharges—all these and many other man—driven factors endanger the ecosystem of the Adriatic and its strand areas (Giani et al. 2012).

Plans of putting on a wide scale of wind farming arise serious concerns with regard to bottom ecosystems: the associated infrastructure (e.g. digging trenches and laying electric cables) may destroy the benthic beds.

In light of the above endangering forcing, extensive national nature protection programs were conceived and put in realization. Protected areas were identified in all riparian countries. Many vast national parks and reserves encompassing river valleys, tide-controlled wetlands and marine coastal zones were established (see e.g. Anonymous 2007).

However, a successful realization of the above protection measures can't dispense with a regular monitoring of inevitable ongoing changes and a timely identification of hot spots.

Airborne and satellite remote sensing means offer an efficient way of reaching this goal. The present study describes an innovative method of zonation of the Adriatic marine coastal zone.

Spectrometric data from ocean color satellites like MERIS, MODIS, Sentinel 2 and forthcoming Sentinel 3 are at the base of the developed procedure to single out zones/areas with specific properties that are liable to close surveillance and, if applicable, protection. The method permits to perform the zonation on a fine scale, but also to upscale it in order to give a better insight in the hydrological and hydrobiochemical factors intrinsically related to the existence/formation of separate zones.

2.1.2.3 Satellite Data

The optical satellite data utilized in this study was acquired by the MEdium Resolution Imaging Spectrometer (MERIS) sensor aboard the ENVISAT satellite of the European Space Agency (ESA). The MERIS instrument has 14 spectral bands

covering the range from 400 to 900 nm at spatial resolutions of 300 and 1200 m (Rast et al. 1999). Remote sensing reflectance products at 300 m resolution are produced by the Ocean Biology Processing Group (OBPG) in 9 spectral bands centered at 413, 443, 490, 510, 560, 620, 665, 681 and 709 nm in the visible range. The number of bands and their spectral placement permit the retrieval of atmospherically corrected data for ultimate calculation of water constituents (Morel et al. 2002), namely concentrations of *chl*, *sm*, *doc* and coccoliths.

MERIS Level 2 data, covering the area of the Pilot Project (the Adriatic Sea) from 2002 until 2010, were downloaded from the NASA Ocean Color Web Portal hosted by the OBPG as 4456 HDF4 files (22 GB). The data encompass values of remote sensing reflectance, R_{rs} at all bands in the visible at a spatial resolution of 300 m and were generated by the MODIS L2 processor version 6.5.8 [http://oceancolor.gsfc.nasa.gov/DOCS/MSL12/master_prodlist.html/]. The data have gaps due to cloud coverage and incorrect atmospheric correction resulting in negative values of reflectance in the blue and red spectral region.

MERIS L2 data with gridded values remote sensing reflectance were reprojected onto a regular grid in cylindrical projection spanning from 15 to 20.5°E and from 39 to 42.5°N with a spatial resolution of 300 m using Nansat (open-source Python library for processing 2D geospatial data https://github.com/nansencenter/nansat, see Chap.6). Additionally, Nansat was utilized to generate 8-days climatological values (below also called weekly climatology) of R_{rs} in the Adriatic Sea. 23 mosaics were generated so that each mosaic is calculated as a linear average of all MERIS L2 images taken within the corresponding period in all years of observations.

2.1.2.4 Unsupervised Classification of the First 5 Principal Components

Unsupervised classification of the pixels in the space of principal components (PCs) was performed using the *k*-means cluster analysis (see Chap. 1), which splits a sample of points in N-dimensional space into groups (clusters) each containing points located close to each other and far from points of other groups.

Zonation is considered successful, when points within one cluster are also grouped geographically. This occurs, when values of a variable in neighbor pixels have similar dynamics, and the correlation between the considered parameter values is high and, therefore, values of PCs are also similar. If the dynamics of neighbor pixels is different (low correlation) then PCs values are also different, the pixels belong to different clusters, and a border is drawn between these zones of low correlative pixels.

Objective grouping of pixels with similar PCs values into groups is preformed with the *k*-means cluster analysis using the 'Scipy VQ' library (http://docs.scipy.org/doc/scipy-0.14.0/reference/cluster.vq.html). The cluster analysis (employing Scipy VQ library) was started 20 times, each time from 20 random positions of the

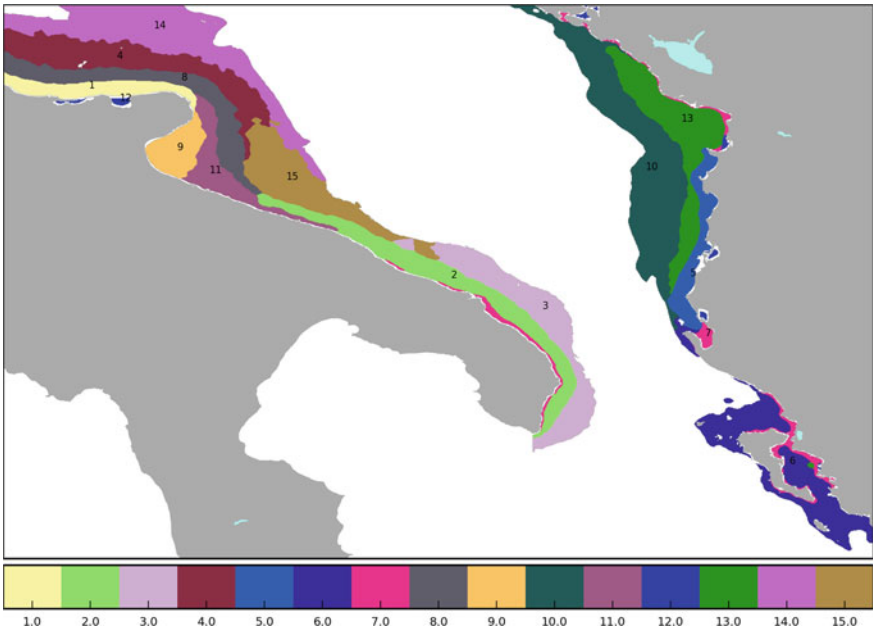

Fig. 2.12 Zonation map generated using the KMCA for the Adriatic Sea and based on the satellite observed heterogeneity of hydro-optical and biogeochemical properties of surface waters

cluster centers. The run resulting in the best convergence yielded centers of 15 clusters and a map with zones was generated.

As the map begins appearing slightly noisy and complicated for vectorization, we smoothed the borders, firstly, by applying the median filter from the 'Scipy NDImage' library (http://docs.scipy.org/doc/scipy-0.14.0/reference/ndimage.html) and, secondly, using minor manual extrapolation and removal of small artifacts (Fig. 2.12).

2.1.2.5 Dynamics of Water Quality Parameters in the Identified Zones

Values of water quality parameters were averaged over each zone and plotted against the time to which the figures pertained. The time-series plots made within one zone were grouped together (Fig. 2.13).

Based on the employment of solely ocean colour spaceborne data, the methodology developed in this study identified 15 separate zones that steadily persisted in the Adriatic shelf "belt-like" area over the period of observations (i.e. 2002–2010).

This was done through a completely computerized procedure analyzing both temporal and spatial variations in specific features exhibited by so called colour producing agents, CPAs. As CPAs, *chl*, *sm*, and *cdom* were considered. In addition,

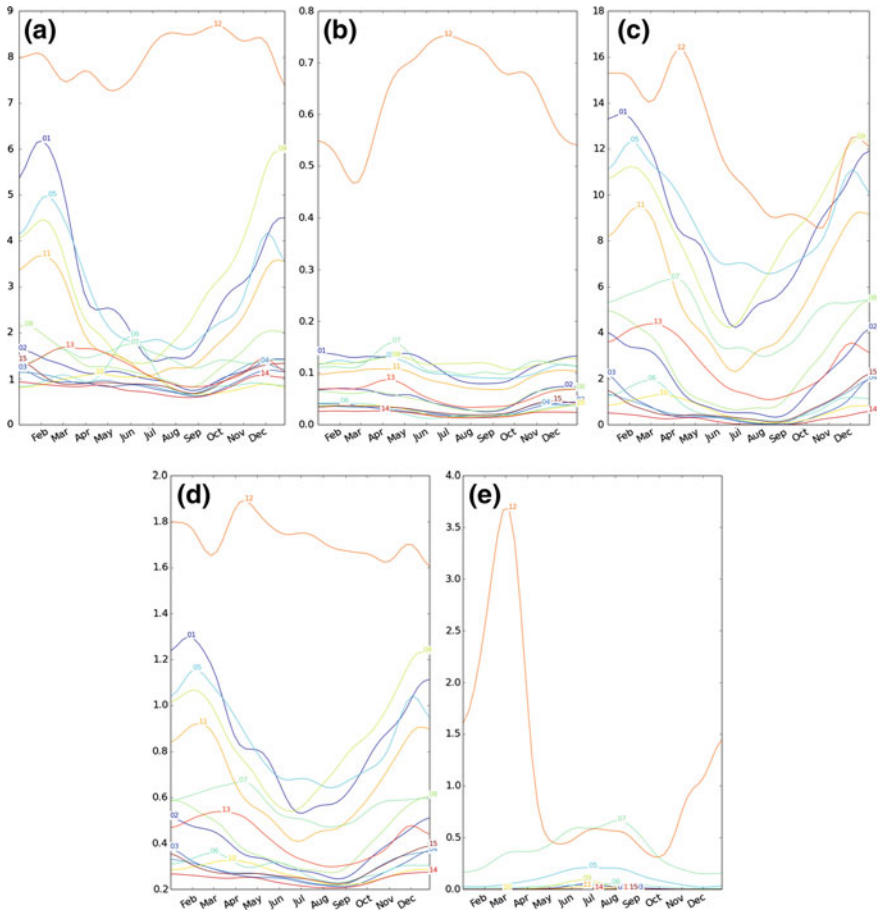

Fig. 2.13 Time series of zone-wise averaged values of concentration of chlorophyll-a [mg m^{-3}] (**a**), CDOM absorption [m^{-1}] (**b**), concentration of total suspended matter [g m^{-3}] (**c**), diffuse attenuation coefficient [m^{-1}] (**e**), and photosynthetically available radiation at bottom [μmol m^{-2} d^{-1} sr^{-1}] (**d**)

the optical transparency of the identified zones was inferred to quantitatively assess the sunlight availability at the bottom. This was done to identify and delineate the areas, which, potentially, might be habitats of bottom vegetation (for methodology see Sect. 2.1.6.

Finally, the available ocean color data were processed to check up if in the open Adriatic the ingenious forms coccolithophorids are present in the phytoplankton composition.

Because both hydrological and hydrooptical conditions typical of the western and eastern parts of the shelf area are substantially different, the further discussion is partitioned into respective subsections.

Western Coast

As Fig. 2.12 illustrates, in this study 10 individual zones have been identified on the western coast. A close concatenated inspection of each zone location and respective temporal variations of CPA concentrations (Fig. 2.13) permits to bring at least some of them in groups.

I. Indeed, with the exception of zones 12 and 9, all other zones, i.e. 1, 3, 8, 11 and 2, have many resembling features of CPA temporal variations:

   the concentrations of *chl* and *sm* as well as the value of diffuse attenuation coefficient, K_d are highest in January-February and rather rapidly drops down in summer, the value of PAR is low throughout the year,
   the absorption by *cdom* is relatively low, but slightly enhances in winter time, and frequently in late spring;
   the contours of these zones extend along the cost line.

II. Zone 12 and 7 are specific: zones 12 are small and very shallow indents cutoff from the sea by narrow land straps. These two zones exhibit specific features in terms of seasonal variations in *chl*, *sm* and *cdom* (Fig. 2.13). Zones 12 appear highly eutrophicated exhibiting high concentrations of *chl*, *sm* and *cdom*, and low water transparency i.e. high values of diffuse attenuation coefficient. Zone 7 remains fairly narrow along most of its extent from north to south, it has relatively low *chl* concentrations that come to a head in summer, and rather enhanced concentrations of *sm* and *cdom* culminating in mid-spring. This mismatch in timing of CPA content reaching their highest values distinguishes it from the zones of the first group.

Zones of Group I on the Western Coast

The pronounced enhancement of CPA concentrations in zones of group I around February is a result of a concerted forcing residing in several components.

Except for the Po River, which is most full-flowing in April–June, for rivers flowing down from the Apennine Mountains to the central western Adriatic coast the discharge rate is generally maximum in February and gradually declines down to low values in July–August (Raiucich 1994, 1996). The river flow can vary considerably from year to year (e.g. for the Po River the mean daily discharge was 8000 $m^3\ s^{-1}$ in 2002/2003 as compared to 3,000,000 $m^3\ s^{-1}$ in 2001–2002, Fain et al. 2007).

Entering the marine coastal zone, the river runoff enhances there the concentration of nutrients. The increase in nutrients drives a pronounced growth of microalgae, which manifest themselves through an intense rise in *chl* (Fig. 2.13). Besides, of all rivers falling out in the Adriatic, only those ones coming on the western coast discharge significant amounts of terrigenous/allochtonous dissolved organics and sediments: this is also evident in Fig. 2.13.

It is noteworthy that arriving to the river mouth, the flux of riverine suspended matter becomes retained there (up to 25–47%) forming mud wedges in the outer periphery of delta (Correggiari et al. 2001).

The general circulation in the Adriatic Sea is driven by thermohaline forcing, which in turn arises from freshwater input in the north (predominantly due to the Po River runoff) and inflow of saltwater from the Mediterranean in the south (Sailot 2005). As a result, a strong north and southward flow sets up along, respectively eastern and western Adriatic. The inflow of numerous rivers into the western Adriatic (Sect. 2.2) accentuates the boundary of the southward flow turning it into a wide "river" in the sea known (Zavatarelli et al. 2002) as the Western Adriatic Coastal Current (WACC). It is noteworthy that moving southward to the Gargano Peninsular (see Fig. 2.11), the WACC becomes stronger and narrower.

As mentioned in Sect. 2.2, named Bora and Scirocco two prevalent storm events annually unfold in the Adriatic. Coming from the northeast, cold winds of Bora (generally much higher than Scirocco and occurring more frequently) cause currents running along the western coast that might be conducive to downwelling motions.

Contrarily, Scirocco warmer winds blowing from the south are known to generate water flows leading to the formation of western coast upwellings (Wang and Pinardi 2002).

Bora and Scirocco winds are capable to strongly affect the WACC, commonly enhancing it. Thus, the winter period is characterized by strong along-shelf currents, which, nevertheless, cause on a local scale circulation pattern perturbations that are dictated by specific features of the local bottom topography (e.g. the Gulf of Venice or the Gulf of Manfredonia).

However, on the whole, along-shore currents in western Adriatic are consistently directed southward, regardless of wind direction (Orlic et al. 1994). Yet it does not exclude that for short periods some individual storm events that override the WACC might result in moving coastal water masses both to the north and to the south.

These two atmospheric phenomena individually, but especially conjointly, cause sediment-resuspention events predominantly within the winter period, which in some locations can extend even to mid-spring. Mostly expressed when the winds are blowing for 12 or more hours from the northeast and southwest, the resuspention events are characterized by high *sm* concentrations driven by enhanced (up to 9 cm s^{-1}) wave-orbital velocity (Komar and Miller 1975). Reportedly, the resuspention events do not strictly correlate with the duration of windstorms: generally, the former last on the order of weeks (Fain et al. 2007).

In situ observations reveal that in addition to suspended matter brought with river discharge, the resuspention events evacuate the sediment accumulations/mud wedges mentioned above, thus considerably increasing the amount of *sm* in the water masses advected southward. The band of current-dragged fine-grained sediments and *sm* extend from the Po River to the Cargano peninsular, and then, skirting it, stretch out further to the north passing by the delta of the Ofanto River,

and to finally tail off. The overall length of this band is assessed at 600 km (Correggiari et al. 1996).

Importantly, in situ studies confidently indicate that the along-shelf sediment flux is about 10 times stronger than the across-shelf flux, which is due to the aforementioned prevalence of along-shore currents moving southward. As a result, a continuous stretch of fine-grained sediments and *sm* becomes established close to the coastline at depths up to ~30 m. This substantiates the reports that the above band of fine-grained sediments is not found beyond areas with a ~30–40 m bottom depth (Faint et al. 2007).

The zones of group I explicitly illustrate the above specific features of the western Adriatic. In winter months a narrow band of enhanced concentrations of *sm* in zones 1, 9, and 11 become very pronounced, and corresponds to the period when river discharge and resuspension are at their highest level. This finds its further substantiation in increased concentrations of *chl* in zones 1, 9, and 11. However, unlike *sm* (prone to gravitational sedimentation), *chl* remains enhanced a bit further offcoast in zones 8 and 15. Also, the strong WACC entrains waters enriched in *chl* southward, where they receive some additional increment in *chl* due to the discharge of the Ofanto River (zone 2).

Further off-coast, the influence of nutrient-rich river waters progressively decrease and the concentration of *chl* in zones 4, 14, 15 and 3 declines. As the combined effect of the Po and Pescara Rivers discharge is far higher than that of the Ofanto River (Sect. 2.2), the extent of zones 4, 15 and 14 into the sea is much greater than in the case of zone 3.

In late spring and closer to summer, the concentrations of *chl* rapidly decline along the western Adriatic, however zones closest to the coast, i.e. 1, 9, and partly 11, retain some growth of phytoplankton. At the same time, the decline of *sm* in the same zones is much slower. This is due to different mechanisms of *chl* and *sm* generation: while the *chl* growth is predominantly governed by the seasonal pattern of river discharge rate, the *sm* content is mainly controlled by along-coast advection driven by both Bora (mostly in winter) and Scirocco (more frequently occurring in warmer seasons). That is why an increased concentration of *sm* persists (with variable intensity) nearly around the year in zones 1, 9, partly 11, and 2.

Similar spatio-temporal variations proceed with *cdom*, however, their magnitude and related excursions are much lower as the discharging riverine waters (originating in the Apennines) are not rich in dissolved organics.

Zone 9 might deserve an additional discussion: located in the very shallow Gulf of Manfredonia, it is prone to very intense wind-mixing, which is the reason why *sm* concentrations in zone 9 are notably high and persist over a longer time than in other zones of this group.

The field of retrieved values of the diffuse attenuation coefficient (Fig. 2.13) additionally emphasize the spatio-temporal variations in concentrations of CPAs, but especially of *sm*, as this CPA is known to be more absorptive than phytoplankton *chl* (Bukata et al. 1995).

Notwithstanding their general likeliness, the differentiation between zones of group I reside in their specific features regarding the typical concentration of CPAs

and their coexisting combinations, as well as the timing of reaching by CPAs their maximal and minimal values.

Thus, the developed technique permitted to make evident in zones of group I not only salient but also, as it might seem, fine distinctions, which, nevertheless, conjointly govern the ecological conditions in a variety of individual areas in the western Adriatic.

Zones of Group II on the Western Coast

Two zones 12 and 7 are attributed to group II. As discussed in the above subsection, zone 12 consists of two small and very shallow indents that are cutoff from the sea by narrow land straps.

As Fig. 2.13 illustrates, these waters are annually highly rich in *chl*, which indicates their high level of eutrophication. Obviously, availability of nutrients, isolation from the sea (assuring minimal dilution by marine waters), and favorable weather conditions determine the trophic status of zone 12.

However, seasonal variations in *sm* exhibit two distinct spans of enhancement: firstly in December-February, but then, more expressly, in mid-May. *cdom* levels are annually high but are highest in July.

It can be only conjectured that this specific timing of culmination of *cdom* absorption is indicative of its autochtonous origin (i.e. produced by phytoplankton ejections of dissolved organics, and hence should be contiguous with respect to the *chl* maximum occurrence, see Fig. 2.13).

The maxima of *sm* obviously regularly happening twice in December–February and Mid-May could be logically associated with the shallow bottom scavenging produced by Bora and Scirocco either respectively, or conjointly (at least in winter months).

It is also notable, that in seasonal variations of all three CPAs, there is a depression falling on a period about March. Moreover, a high spike in PAR at the bottom also falls on the same time period. Debatably, this rather steep increase (followed by an equally steep decrease) arises from two reasons, viz. a temporary intermission in stormy winds occurring rather regularly in this region, and a very small bottom depth. It implies that in such moments the incident solar light is only slightly attenuated by *sm* within a very shallow water column.

Zone 7 is a very narrow strip in the southern west coast. This zone is also rather shallow, but unlike zone 12, does not show any indications of eutrophication: possibly because of its remoteness from river discharges. The highest levels of *chl* and *cdom* occur very closely in time permitting to suppose that *cdom* in zone 7 is mostly autochtonous.

The concentrations of *sm* are rather significant and increase with the approach of warmer time to eventually culminate in late spring. Because of shallowness, this zone must be prone to resuspension processes driven by wind storms, only in this case the timing of highest concentration of *sm* in the warm period gives grounds to ascribe this effect primarily or even exclusively to Scirocco. Indeed, as was discussed above, its higher incidence falls on warm seasons.

Eastern Coast

As mentioned above, the application of our methodology yielded 5 zones, viz. 13, 10, 7, 6, and 5 in the Eastern Adriatic. Plots in Fig. 2.13 show that these zones differ considerably in terms of their optical properties.

Following the zone categorization approach applied to the Western Adriatic, the zones in the Eastern Adriatic also fall into two groups.

Zones of Group I on the Eastern Coast

The pattern of seasonal variations of CPA concentrations in zone 5 is akin to that in zones 10 and 13. Indeed, zone 5 is distinguished by high concentrations of *chl*, *sm*, and relatively enhanced values of *cdom*. Across the annual seasons, the content of *chl* and *sm* reaches highest values in Zone 5 in February–early March. The seasonal pattern of variations in *cdom* absorption also exhibits a rise in February, although this rise is mild against the general background of *cdom* absorption intensification towards the wintertime. Due to this synchrony in reaching the above maxima, the water is the least clear around February. Under these conditions, the sunlight in the PAR region practically does not reach the bottom, obviously implying that zone 5, by and large, is not favorable for benthonic vegetation growth notwithstanding a slight improvement in water transparency that occurs only in mid-summer to be then followed by autumnal and wintertime re-dimming of the water column light climate.

Zone 5 is a recipient of numerous Albanian rivers (Sect. 2.2, and Fig. 2.11c), whose discharge in the Eastern Adriatic is highest in February–March (Ciavola et al. 1999). Approaching the coast, these rivers flow through the hinterland encompassing, inter alia, alluvial and marshy areas.

River bank erosion and draining of waters with enhanced concentration of humic matter affect the composition of waters entering this part of the Eastern Adriatic. This explains the aforementioned hydro-optical properties in zone 5.

The pattern of seasonal variations in Zone 13 is generally consistent with the respective features discussed in relation to zone 5. Water in Zone 13 is also loaded with phytoplankton (*chl*), *sm*, and dissolved organics but at a significantly lower levels (it refers especially to *cdom* levels, Fig. 2.13). This is due to the dilution of fresh waters in marine waters. This dilution is particularly accentuated by the East Adriatic surface current carrying strongly saline and warm Mediterranean waters through the Straits of Otranto northward along the entire Eastern Adriatic (Manca et al. 2003). The seasonal pattern in CPAs variations is also controlled by inflowing rivers, most fullflowing of which are the Rivers Drin (Drini) in Albania and Buna in Bosnia and Herzegovina: the discharge rate of these rivers is also highest in late winter–early March, whereas the minimum falls on midsummer–early fall (Ciavola et al. 1999).

Compared to zone 13, water in Zone 10 is much clearer due to the dilution mechanisms discussed immediately above.

Zones of Group II on the Eastern Coast

Zone 6 is characterized by relatively high *chl* concentrations (culminating in June and slightly enhanced in February), moderate loading in *sm* (peaking in March), and low values of *cdom* absorption. It can be conjectured that the water movements within the area adjacent to the coastline are significantly slowed down due to the narrow strait between the mainland and island Corfu. Notably, the outer coast of Corfu is considerably irregular with several lagoons and prominences, which are also capable of rendering zone 6 as a whole rather stagnant. This can be an explanation of somewhat elevated concentrations of *chl* and to a lesser degree *sm*. It is noteworthy that the timings of highest concentrations of *chl* and *sm* are not mutually corresponding: midsummer and early spring, respectively. Given that the month of phytoplankton highest growth is retarded till midsummer, and hence not driven by nutrients input with river discharge (firstly, there are no rivers discharging nearby, and secondly, as we saw, the runoff of all rivers in this region is maximum in February–March), it might be supposed that this is a manifestation of secondary production (Mistri et al. 2001). *cdom* absorption levels are low indicating that there are at least no terrestrial sources of humic matter. Zone 6 is located within the area of significant depths, and low values of PAR at bottom (Fig. 2.13) allow to presume the absence of extensive benthonic vegetation colonies.

The fact that the culmination in *sm* content in this zone falls on March and November-mid December should be interpreted as strong indication that the driving mechanism here is land runoff from both the mainland and Island Corfu: indeed these two timings finally coincide with the month of most heavy rainfalls on the eastern coast of the Adriatic (Ciavola et al. 1999).

Zone 7: its specific hydro-optical features and presumable conditions conducive to its formation were discussed in Sect. 2.1.2.5.

Coccolithophores

The bio-optical retrieval algorithm BOREALI employed in our study permits to assess (in addition to CPAs traditionally assumed as water quality parameters, viz. *chl*, *sm* and *cdom*) also the counts per m^3 of coccoliths (Sect. 1.5.1) that are released by coccolithophores in the course of their life cycles (Thiersten and Young 2004). Balestra et al. (2008) investigated living coccolithophore distributions from the Gulf of Manfredonia (Fig. 2.9). They found, inter alia, *Emilinia huxleyi* cells with the coccosphere densities predominantly located above the thermocline between 25 and 30 m below the water surface. However, the coccolith counts were relatively low. This is in concordance with the reports by Aubry et al. (2004) based on a 10-year period of samplings in the Adriatic. The contribution of coccolithophores to the phytoplankton groups invariably accounted for 1% or even less: the dominant groups proved to be diatoms and nanoflagellate, whereas dinoflagellates are the third runners. Our satellite data (not illustrated here) are supportive of this shipborne information: the number of coccoliths is low throughout the year, slightly

increasing in the off-coastal direction (numbers of zone in the declining order: 14, 4, 3, 15, 2, 13, 11, 7, 1). Not being prone to photoinhibition, and preferring warm temperatures, coccolithophores (mostly presented by *E. huxleyi*) reveal a seasonal pattern of growth: their abundance is more enhanced in late summer–early fall.

Thus we emphasize that, based exclusively on ocean color satellite data, the technique developed permits to differentiate between marine zones taking into account not only the CPA concentrations and specific features of their seasonal variations, but also the light regime in both the water column and at the bottom.

The analysis of formation of the revealed zones in the Adriatic brings to light the role in this process of marine circulation patters on various spatial scales, episodic but fairly frequent and annually recurring strong wind phenomena conducive to massive sediment resuspention, predominantly southward water masses advection as well as some other factors such as specific features of bottom topography and landscape, etc.

The obtained zonation data, concertedly with other findings embedded into a dedicated GIS that was developed under the CoCoNet project, can be instrumental in a comprehensive characterization of the Adriatic Basin, its water quality present status and its expected dynamics in terms of (i) hydrobiotic processes and associated trophic interaction chains, and (ii) alterations to the marine ecosystem, especially in areas that are either already endangered or easily susceptible to degradation caused by anthropogenic pressing.

2.2 Arctic Ocean

2.2.1 White Sea

2.2.1.1 General Characteristics

The White Sea (Fig. 2.14) is a marginal shelf sea, with a total area of 90,800 km^2, including islands (Filatov et al 2005). The mean depth is 67 m and the maximum depth is 350 m (Anonymous 1994).

The White Sea is essentially a mediterranean sea, which is enclosed by surrounding land areas. Its watershed is about 715,000 km^2. Several biogeographic zones, from tundra to southern taiga, are found within the catchment area.

The northern part is connected to the Barents Sea through a strait called Voronka (Funnel). The southern and central parts of the White Sea, called Bassein (Pool) are the largest and deepest regions of the sea. There are also several large bays in the area, namely Dvinskiy, Onezhskiy, Mezenskiy and Kandalakshskiy Bays, called (with the exception of the latter one) after the respective inflowing rivers (Severnaya Dvina, Onega, and Mezen). It is the Niva River that flows into Kadalakshskiy Bay.

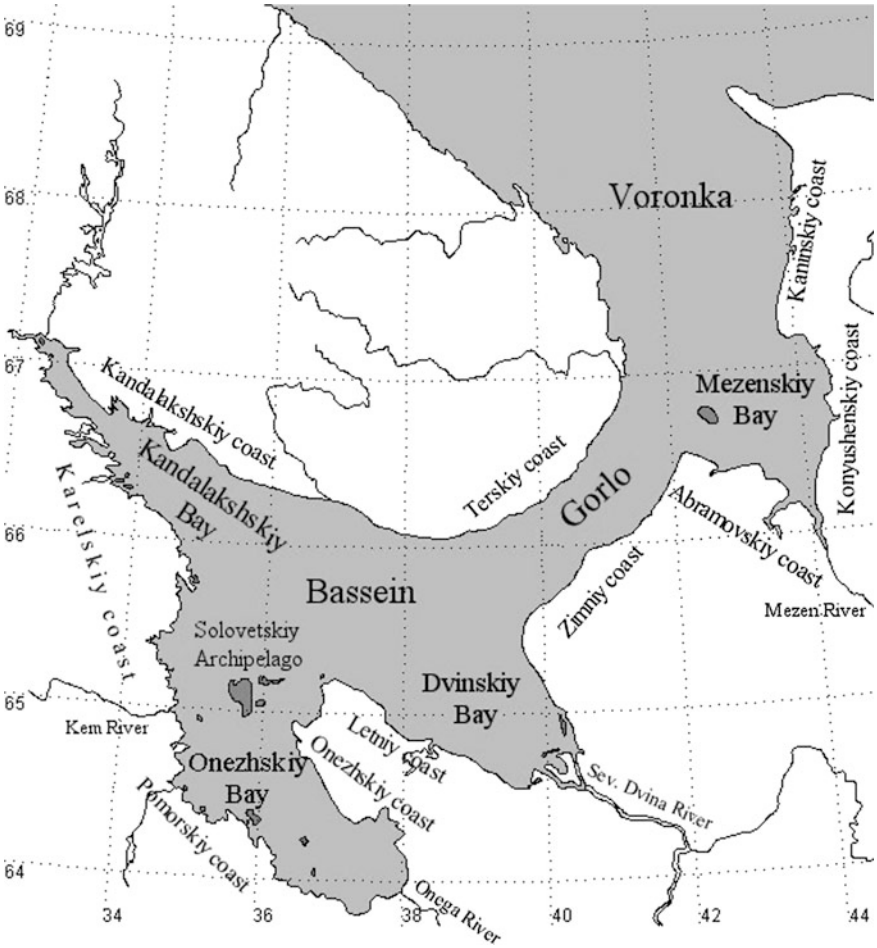

Fig. 2.14 The White Sea geographical location and regionalization. The specific areas specified in this figure are further referred to as I—Kandalakshskiy Bay, II—Onezhskiy Bay, III—Dvinskiy Bay, IV—Gorlo, V—Voronka, VI—Mezenskiy Bay

Bottom relief. The bottom relief of the sea is irregular (Fig. 2.15): the northern region is rather shallow, although in the northern margins of the Voronka depths can reach 60–70 m. In the off-shore part of Mezenskiy Bay, depths are less than 20 m. The average depth in the Gorlo is about 45 m, although there are troughs found along the middle part of the strait.

The morphometric features and the bottom relief of the sea determine the most important attributes of the inherent in-water processes such as the water exchange with the Barents Sea, a highly pronounced effect of river runoff, the formation of water masses and frontal zones, water circulation patterns, regular features of tidal wave propagation, and sea ice regime.

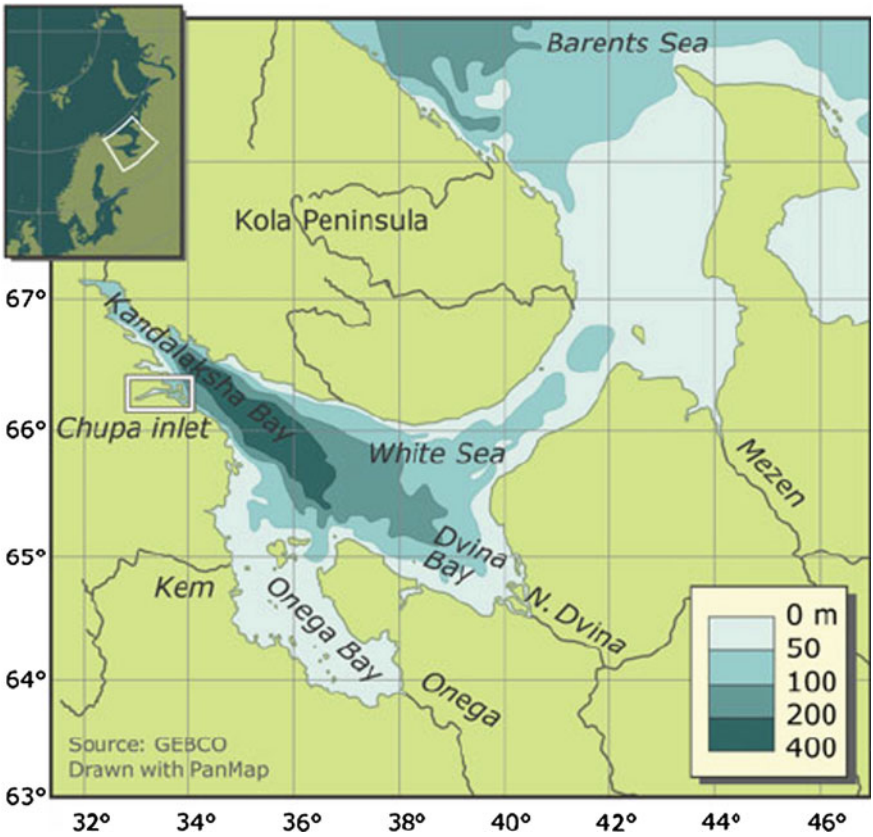

Fig. 2.15 Bathymetry of the White Sea

As compared to the White Sea total water volume, the freshwater discharge per year is small (only 5%), but has major consequences for the marine thermohydrodynamics and biogeochemistry.

In general, the river discharge is highest in May with a secondary enhancement in October. The water of the tributaries to the White Sea contains high amounts of humic substances, either dissolved or in the form of colloids. The concentration of dissolved organic matter in discharging riverine waters reaches up to 18.3 mg l^{-1} (the River Kem, southwestern coastline). The river waters also contain nutrients varying with season. In the open parts of the White Sea, the maximum concentration of dissolved organics is much lower (4–5 mg l^{-1}).

That is why the White Sea water is mostly greenish in colour. In river mouths, the water colour varies from yellow to brownish, depending on the presence and amount of soil humus substances brought in with riverine waters. The Secchi depth is 7–8 m in the open sea and 2–3 m in the delta areas.

Water temperature. The White Sea is characterized by both the presence of a well-pronounced vertical stratification and fairly large seasonal fluctuations of surface and bulk water temperature. However, the water column in the large bays (with the exception of Kandalakha Bay) is nearly homothermal at any time of the year.

The mean SST throughout the sea varies between +3.2 °C (in the middle part of Onezhskiy Bay) and +4.2 °C (in the Voronka). During the winter period (November–March) the SST in marine pelagic areas varies from +1.2 to +1.7 °C, and in the large bays from +0.5 to +0.7 °C. In spring, the water temperature rises, on average, by +2.0 °C in the Voronka and Gorlo, +4.0 °C in the Bassein and +6 °C in the bays. In summer, mean SST increases strongly reaching 14 to ~18 °C in August. In October, the coastal SST declines rapidly, becoming lower than in the open sea (The White Sea 2005).

Currents. Figure 2.16 displays the surface currents in the White Sea. In the Bassein and southern Kandalaksha Bay (the deepest regions of the sea) there are permanent eddies with cyclonic and anticyclonic directions. In addition, persistent *coastal* currents are characteristic of the White Sea: waters are drawn along the

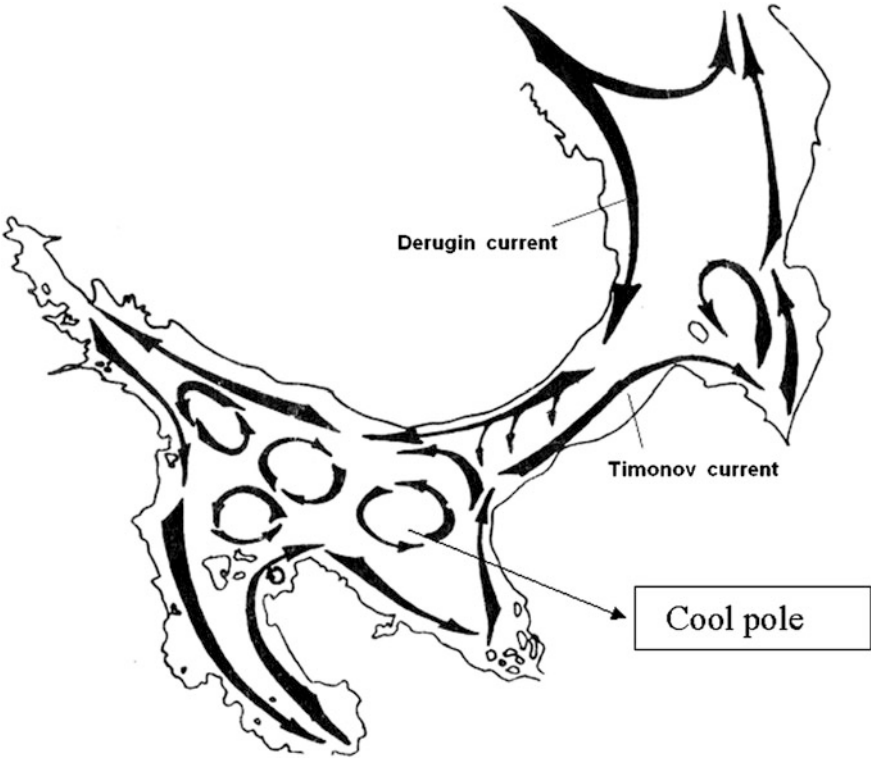

Fig. 2.16 System of persistent surface currents in the White Sea (after Naumov and Fedyakov 1993)

western coastline from north to south and further back to north in the east. The current speeds in the open sea reach 10–15 cm s^{-1}, in narrows and near capes they accelerate to 30–40 cm s^{-1}. In the Gorlo and Mezenskiy Bay they reach 250 cm s^{-1}. In Onezhskiy and Kandalakshskiy Bays, the speed typically reaches from 80 to 100 cm s^{-1} and from 30 to 35 cm s^{-1}, respectively (Dobrovolsky and Zalogin 1982).

Tides. Their amplitude varies across the sea between 0.7 and 8 m (Anonymous, 1994) influence sea water level, the water mass exchange between the White and the Barents Sea as well as front generation. A variety of marine *frontal zones* are found in the White Sea. Some are formed under the influence of river runoff (the runoff and estuarine fronts), whereas others are driven by tides, seasonal heating as well as by specific features of bottom relief and shoreline contours. The brackish water plumes extend most offshore in spring (when the river discharge peaks), but they shrink progressively until they nearly disappear in late autumn. Tidal fronts are the principal fronts in the White Sea. For instance, the tidal front separates the Gorlo from the Bassein, whereas the second one lies in Onezhskiy Bay in the vicinity of the Solovetskiy Archipelago. Both fronts originate in mid-May, and they are most pronounced in late July–early August. Fronts due to upwelling cold water are often found in the region of the Solovetskiy Archipelago. The White and the Barents Seas are also separated by a permanent front.

2.2.1.2 Remote Sensing Observations

The methodology of establishing from space spatial and temporal variations in *chl*, sm, *doc* and SST is described in Chap. 1. A comparison to historical in situ observations was employed to process SeaWiFS images over the White Sea for the entire period of the sensor operation, i.e. 1997–2004.

AVHRR data were processed for the same period. Animated distributions of *chl*, *sm*, *doc* and SST were obtained with a time interval of five days. Based on these data, monthly averages were calculated for the period April–September (Fig. 2.17).

The spring phytoplankton are mostly diatoms, which develop amply in cool water. *In April*, while some parts of the White Sea still remain covered by ice (The White Sea 2005), the phytoplankton start developing in the southern part of Onezhskiy Bay, and, to a lesser degree, upward to the north, in Dvinskiy Bay in the area immediately neighboring the delta of the Severnaya Dvina River (Fig. 2.17a).

There is an area of some enhanced *chl* concentrations to the south of the Solovetskiy Archipelago, this area being known as a stable upwelling zone (see the introductory subsection above).

These distributions are governed by both the nutrients and light availability. In the bays, the nutrients are brought in with river discharge, while in the vicinity of the Solovetskiy Archipelago, they are entrained upward by the upwelling movements. Some enhanced *chl* concentration can be observed along the southern coastline of the Gorlo. The concentrations of *doc* and *sm* are still very low throughout the sea.

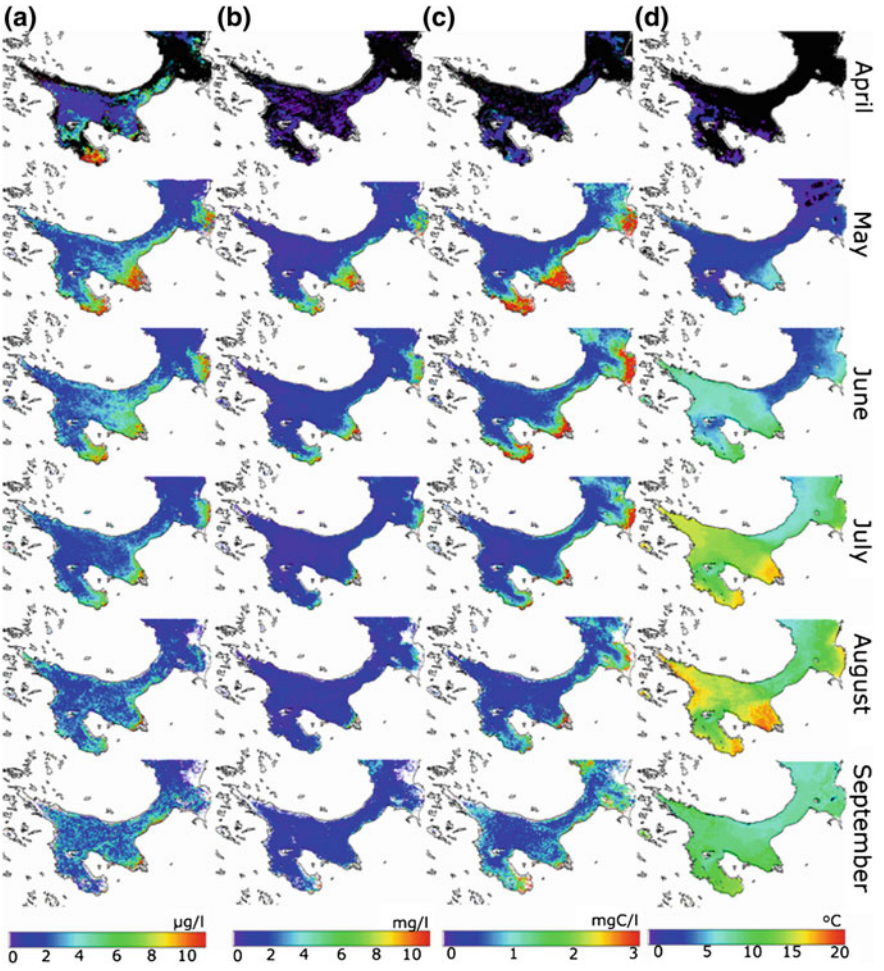

Fig. 2.17 Monthly averaged concentrations of **a** *chl* (µg m^{-1}), **b** *sm* (mg m^{-3}) and **c** *doc* (mgC m^{-3}) as well as **d** SST (°C) over the White Sea throughout the vegetation period as retrieved from space

In May, as SST gradually increases, but mostly in shallow Onezhskiy and Dvinskiy bays (however, not yet in Mezenskiy Bay, which is more to the north), and the river discharge is the highest (see the introductory subsection above), the pattern of CPA and SST distributions change accordingly (Fig. 2.17a–d).

The phytoplankton strongly develop in Onezhskiy and Dvinskiy Bays and also in the pelagic regions of the Sea. At the same time, the phytoplankton outbreak starts also in Mezenskiy Bay, mainly cold water diatoms that have already bloomed in the two southern bays. The concentrations of *sm* and *doc* increase appreciably in the bays due to the peaking river discharge, which is rich in both *sm* and dissolved and suspended soil humus fractions. Phytoplankton are abundant in the Gorlo,

mostly along its southern coastline, the algae being advected from Dvinskiy Bay by the Timonov coastal current (see Fig. 2.16).

Two frontal zones due to river discharge in Onezhskiy and Dvinskiy Bays (see the introductory subsection above) are distinctly discernible in the SST distribution (Fig. 2.17d).

In June, the concentrations of CPA start somewhat receding, which is due to the beginning depletion of nutrients for phytoplankton and lower river discharge for *sm* and *doc*.

At the same time, the frontal zone separating the Bassein and Gorlo as well as the tide-driven upwelling zone around the Solovetskiy Archipelago (see the introductory subsection above) become more obvious in the SST distribution (Fig. 2.17d). Warm water extends northwards, reaching the deep parts of the White Sea, i.e. Kadalakshskiy Bay and the Bassein. As a result, the thermal gradients across the frontal zones that are due to river discharge temporarily diminish.

In July, the SST in the main shallow bays continues to increase and reaches 17–18 °C in the innermost parts of Onezhskiy and Dvinskiy Bays. The thermal gradients within the river discharge frontal zones become again enhanced, whereas over vast areas covering Kandalakshskiy Bay and the Bassein but also Mezenskiy Bay the spatial distribution of SST becomes rather homogeneous. However, there is a strip of relatively cool water extending from the Voronka through the Gorlo along its northern coast (the Derugin current, Fig. 2.11), which is the residual of the frontal zone caused by the tides.

The phytoplankton concentration continues receding throughout the White Sea as the nutrient availability becomes progressively scarce. Low levels of river discharge result in shrinking of the associated frontal zones in Onezhskiy and Dvinskiy Bays as well as in a substantial decrease of content of *sm* and *doc* there.

The changes in SST observed in July continue into *August*: the water temperature increases further, reaching 20 °C not only in bays but also along the northwestern coastline of the White Sea. The thermal fronts persist in the bays, and the tidal front separating the Gorlo and Bassein becomes again expressed slightly stronger. The retrieved dynamics in the position of river discharge fronts and the extent of associated plumes is in very close agreement with the available in situ observations of SST (The White Sea 2005).

At the same time, in August the biogeochemical cycle in the White Sea reaches the phase when the nutrient concentrations increase slightly again after the mid-summer minimum. A second, although far less strong phytoplankton bloom begins. Concentrations of *sm* and *doc* remain at low levels.

The phytoplankton growth continues till *mid September*. The autumnal/secondary maximum is not characterized by a well-developed algal biomass peak, as it is influenced by the declining water temperature and lower solar irradiance, although the nutrients might remain fairly abundant during autumn (The White Sea 2005). Concentrations of *sm* begin to increase slightly, which is thought to be due to the second/autumnal increase in river discharge, peaking in October (see the introductory subsection above). However, apparently this does not entail a substantial enhancement of *doc* concentrations.

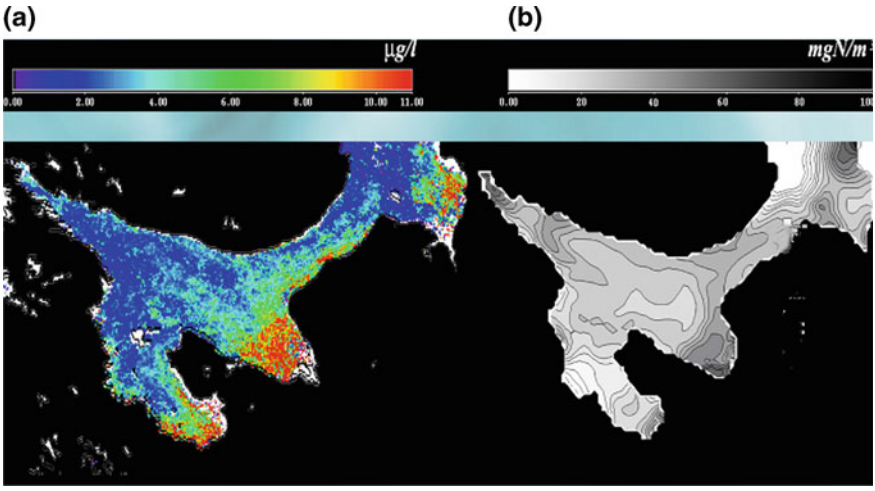

Fig. 2.18 A comparison of spatial distributions of *chl* (μg/l) and simulated phytoplankton biomass (mgN/m^3)

The surface thermal expressions of the upwelling front in Onezhskiy Bay as well as the tidal front, constituting the Bassein/Gorlo abutment, become further accentuated.

In October, the SST is distributed rather homogeneously throughout the sea. The phytoplankton activity comes to an end, which is indicated by the seawater transparency (Secchi depth) that increases to eventually reach its maximum of 7–8 m (The White Sea 2005).

Such are the major biogeochemical and thermohydrodynamic features retrievable from the collected satellite data in the visible and thermal infrared.

The retrieved spatial distributions of *SST* (°C) have been compared with the results of IO RAS modeling of SST. Mean monthly *chl* remote sensing data (MODIS, 2002–2004) for the summer period for Onezskiy Bay, Dvinskiy Bay and the entire White Sea are illustrated in Fig. 2.18, which displays the comparison of 2D distributions of *chl* and phytoplankton biomass for the White Sea. Table 2.1a, b illustrates the correlation coefficients for the simulated and retrieved *chl*-phytoplankton and SST data.

High levels of correlation coefficients in Table 2.1 a, b indicate a good concordance in spatial and temporal variability in phytoplankton *chl* and SST data provided by remote sensing and simulations.

Table 2.1 reveals, however, that specifically for Onezhskiy Bay, the correlation between the remotely sensed and simulated SST data, especially for the month of May, is slightly worse. It indicates that it is the model deficiency: for some reasons it fails to reproduce accurately the hydrodynamic situation in this bay. At the same time, as Table 2.1a illustrates, unlike SST, the phytoplankton abundance variance in this bay is simulated quite successfully.

Table 2.1 Coefficients of correlation between the simulated and retrieved values

(a) *chl* (μg l^{-1})-phytoplankton biomass (mgN l^{-1})					
Month	Simulated phytoplankton biomass, mgN m^{-3}				RS *chl*, μg l^{-1}
	Year				
	1998	1999	2000	Interannual mean	
5	17.6	16.5	15.2	16.4	5.6
6	10.3	9.7	9.3	9.8	5.1
7	6.8	5.5	5.2	5.8	4.2
8	5.2	4.2	3.8	4.4	3.7
9	4.8	4.7	4.4	4.6	3.5
Correlation coefficient, *r*	**0.96**	**0.95**	**0.96**	**0.96**	

(b) SST (°C)				
Marine region	Year			
	1998	1999	2000	Interannual mean
Dvinskiy Bay	0.96	0.91	0.95	**0.95**
Onezhskiy Bay	0.93	0.78	0.94	**0.90**
Entire White Sea	0.97	0.96	0.99	**0.97**

The satellite data are further used for assessing interannual variability and *tendencies* in water quality and marine trophy over a period of 7 years. The interannual variability in *chl*, *sm* and *doc*, established by us from the satellite data retrievals, shows a steady and fairly smooth variation of these constituents throughout the period 1998–2004. Based on this finding and according to the regionalization discussed above (Fig. 2.9), a seven-year trend was assessed for *chl*, *sm* and *doc* separately for five regions: Kandalakhshskiy, Onezhskiy and Mezenskiy Bays, the Bassein and Gorlo (for the Voronka and Mezenskiy Bay the data proved to be insufficient for this analysis). For each zone a separate polynomial dependence has been established to calculate the concentration of a CPA. The calculated concentrations were then averaged over each of the region. A relative change of CPA concentrations, $\Im$ was then obtained from the following expression:

$$\Im = \{[C_{CPA}(1998)] - [C_{CPA}(2004)]\}/\{[C_{CPA}(1998)] - [C_{CPA}(2004)]\}. \quad (2.1)$$

These estimations indicate (Fig. 2.19) that in two southern bays, the content of *sm and doc* increased significantly by a factor varying between 10 and 18%.

The northwestern-most bay, relatively deep and previously with very clear water, shows an even higher water turbidity (due to *sm*) and opacity (due to *doc*) increase (because the baseline was lower).

These changes in *sm* and allochthonous *doc* are to be expected if the river runoff increases due to the observed steady enhancement of atmospheric precipitation over land (Anonymous 2005). Due to the persistent coastal currents, the riverborne *sm* and *doc* are advected from the main bays into the central region and the Gorlo and spread there due to the persistent mesoscale eddies and strong tidal motions (see the introductory subsection above). Thus, the central part, i.e. an essentially pelagic

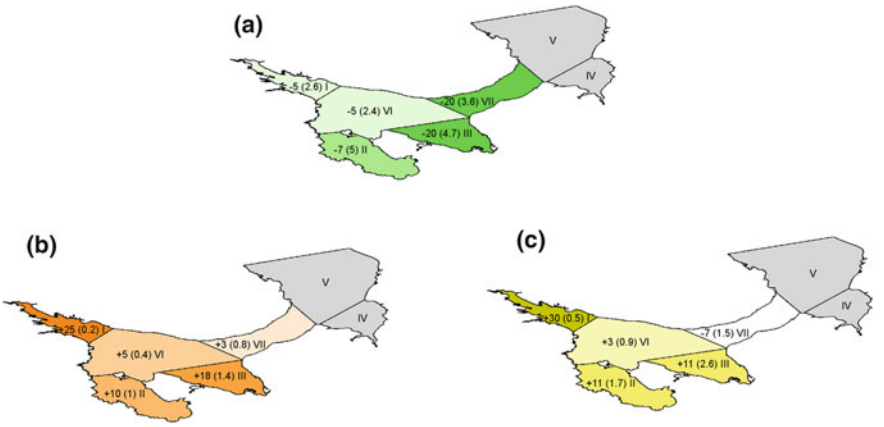

Fig. 2.19 Linear trends (%) in regional variations of concentrations of **a** *chl*, **b** *sm*, and **c** *doc*, in surface waters during the phytoplankton vegetation period, May 1–September 30, in the White Sea, as obtained from SeaWiFS data, 1998–2004. *Numbers in parentheses* are the mean annual baseline concentrations of *chl* (μg l^{-1}), *sm* (mg l^{-1}), and *doc* (mgC l^{-1}) for 1998. *Shading* indicates magnitude of trends. *Roman numerals* in Fig. 2.2a indicate regions specified in the text. *Light gray-shaded areas* IV and V in the northeast indicate insufficient data due to frequent cloudiness

marine area, shows only a few percent increase. Variations of *sm* and *doc* in the channel are governed by the advection of southern bay waters (enriched in both *sm* and *doc*) by persistent coastal currents as well as by the influence of the inflowing Barents Sea waters.

In contrast, the *chl* concentration decreases in the main bays, e.g. in the southern bay with the maximum increase in the content of *sm* and *doc*, the *chl* concentration decrease is 20%. It also strongly recedes in the northwestern-most bay (the decrease percentage is so high because the baseline was low there). For the bays, the revealed decrease in *chl* can also be explained by precipitation-driven higher runoff increasing water turbidity and opacity produced by, respectively, *sm* and allochthonous *doc* (i.e. *doc* brought in with river discharge as opposed to the autochtonous fraction of *doc* generated by the decomposition of phytoplankton by bacterioplankton and consumption by zooplankton).

Regarding the aforementioned optical influence of CPAs, it is known that an increase in the concentration of *sm* leads to a decrease in water transparency, particularly at short wavelengths (e.g. Pozdnyakov and Grassl 2003). Comparing with *sm*, *doc* intercepts even more efficiently the downwelling sunlight propagating through the water column at short wavelengths. Thus the increased concentrations of riverborne *sm* and allochthonous *doc* cut down the amount of subsurface light that phytoplankton can use for their photosynthetic primary production.

Since the cloudiness assessed by us from SeaWiFS data for the seven years did not show any significant increase, only the enhanced concentrations of *sm* and *doc* are responsible for the reduction of sunlight needed for algal photosynthetic production.

Interestingly, the reduction of algal photosynthesis evolves against the background of higher nutrient concentrations in the bay waters also due to the increased land- and river runoff. Obviously, lower sunlight levels are more important than nutrient increase.

Conversely, in the pelagic areas the influence of *sm* and allochthonous *doc* brought in with land- and river runoff is low, whereas the concentration of autochthonous *doc* depends on the concentration of phytoplankton, which in our case is generally low (see the introductory subsection above) and, in addition, is significantly decreased over the study period. Therefore, the water transparency there is affected by variations in atmospheric precipitation over the White Sea catchment area only indirectly through the aforementioned advection of waters enriched in *sm* and *doc* from the major bays.

Our retrievals of interannual SST variations from satellite data for the time period from 1985 to 2004 indicate that there was an overall positive trend across the White Sea, although the amplitude of SST variations was very high: the highest values appearing in 1997, 2000 and 2004 and the lowest values in 1999 and 2002.

Thus, notwithstanding a relatively short time series used in the analyses we conclude that (i) the observed increase in both annual precipitation and air temperature over the catchment of the White Sea during the last decade have changed the state of the marine environment, (ii) these changes are triggered by the increased water turbidity and opacity as a result of enhanced land-, but mostly, river-runoff.

The consequences of this effect are at least twofold: (1) reduction of the indigenous phytoplankton photosynthetic activity and algal biomass accrual, and (2) impairment of the inherent trophic interactions when due to decreased underwater visibility, the fish fail to amply consume zooplankton, and thus unreduced population of the latter graze out more phytoplankton (Asknes et al. 2004).

Therefore, the net result of this twofold effect is a reduction of primary production, which is a key parameter of all aquatic ecosystems. Importantly, this mechanism comes into action nearly immediately with increased runoff, whereas water column warming is a rather inertial process. Based on our study, we contend that the ecosystems of marginal, especially semi-enclosed arctic seas, exemplified by the White Sea, due to the revealed mechanism respond rapidly to regional climate change and therefore are particularly vulnerable to future global warming. However, in order to extend this conclusion and render it more general, similar analyses should be performed for other shelf seas, hopefully with prolonged time series from the MERIS and MODIS sensors extending SeaWiFS data.

2.2.2 Kara Sea

2.2.2.1 General Characteristics

The Kara Sea (for geographic location and names see Fig. 2.20a, b and Volkov et al. 2002) has an area of 883,000 km^2, and approximately 82% of it constitutes

the shelf zone with depths less than 200 m. The mean depth of the Kara Sea is 111 m and the maximum depth of 620 m is located in the northern most province of the sea (80° 26′N and 71° 18′E (Suhovey 1986). The most prominent features of the Kara Sea bathymetry are the St. Anna (with depths up to 610 m) and Voronin (with depths up to 450 m) troughs. Between these toughs is the Central Kara plain with depths of less than 50 m. Along the Novaya Zemlya coast is the Novozemel'sky depression with a depth of more than 400 m. The southern and eastern parts of the Kara Sea, adjacent to the mainland, are shallow. The sea bottom is crossed by numerous minor depressions and is divided by a sill. The bottom is relatively level in the central regions. On the whole, 64% of the Kara Sea area has depths less than 100 m, and 2% have depths greater than 500 m (Suhovey 1986). The coastline of the Kara Sea is complicated and irregular. The eastern shores of Novaya Zemlya are rugged and have numerous fiords. The mainland coast is very rugged, where the Baidaratskaya and Ob Gulfs cut deep inland, between which the Yamal peninsula protrudes into the sea. To the east there are three large bays, Gydansky, Yenisey and Pyasinsky (the latter is at the mouth of the Pyasina River).

The Kara Sea has a unique hydrological feature: it annually receives a record amount of river runoff ($\sim$1350 km^3), which is equivalent to a 1.52 m deep fresh water layer if spread throughout the entire area of the Kara Sea (Lammers et al. 2001; Volkov et al. 2002). This accounts for about 56% of the total river runoff into the coastal seas of the Arctic Ocean. Such an extraordinary rate of fresh water supply into the Kara Sea is due to two inflowing great Siberian rivers, Ob and Yenisey: together with the other two, much smaller rivers, Pyasina and Nizhnyaya Taymyra, they constitute 94.2% of the entire amount of fresh water entering into the Kara Sea. The seasonal variations are significant, with a typical freeze-up period from October to May.

Along with the river runoff impact, inflow of warmer and nutrient-enrich waters from the Barents Sea also affect the hydrological regime in the Kara Sea. However, the presence of Novaya Zemlya and Vaygach Islands in the west, Franz Josef Land in the north and Severnaya Zemlya Islands accentuate the impact of river runoff on the hydrological regime as well as the trophic status of the sea (Matishov and Pavlova 1990).

During the warmest months the ice-free water temperatures rise up to 6–8 °C (and in some years up to 10–12 °C). In the northern regions the temperature in ice-free areas reaches only 2 °C and, under the ice water temperatures rise very little above the freezing point. The thermocline is formed in summer over the entire ice-free area of the Kara Sea.

In warmer seasons, the spring inflow of river water and ice melt reduces the surface salinity in the near north mouth areas and also in the coastal band. River waters in the Kara Sea expand over significant distances from the respective river mouths. The desalination of the surface layer is maximum in summer when large areas are "covered" by water layer whose salinity is as low as 5–10 psu. Further north, the salinity of the surface water increases up to 15–20 psu (Bauch et al. 2003).

Although there is a general transport of waters from west towards east, the pattern of spread of freshened waters in the Kara Sea depends predominantly upon the prevailing winds, and thus can vary from year to year. Either fan-like (Fig. 2.21a), or northern (Fig. 2.21b) or else eastern (Fig. 2.21c) options of distribution of desalinated waters in the Kara Sea can establish in summer. In this time of year, the surface waters contain between 50 and 70% of river water at the northern and northwestern boundaries of the Kara Sea, whereas in the south this share can be in excess of 90%. At depth, under the freshened waters, there is a layer of salinity strong enhancement that restrains wind mixing.

A persistent cyclonic circulation in the south-western part of the Kara Sea (between Novaya Zemlya Island and the Yamal Peninsular) can draw the freshened waters off the northern part of Novaya Zemlya down to Karskie Vorota Strait. The same circulation pattern entrains the Barents Sea waters bringing them further up to the Yamal Peninsular. Waters from the Rivers Ob' and Yenisey spread across the sea in a fan-like pattern: part of these waters form a current moving counter-clockwise to the south-eastern Kara Sea, while the other part turns northward and north-eastward toward Strait Vilkipskogo (Fig. 2.20a).

The swampy soils that are abundant within the watershed of the main rivers flowing into the Kara Sea are the source of significant amounts of dissolved fractions of soil humus brought in along with the river runoff. In addition, owing to land runoff and erosion of river banks and river beds, enhanced amounts of suspended matter and nutrients reach the Kara Sea and eventually become spread over its vast areas.

Invariably suffering from undersampling, shipborne studies fail to produce the desired data at the spatial and temporal resolution. Therefore optical remote sensing from satellites, under favorable weather and light conditions, can efficiently contribute to studies for exploring the spatial and temporal variations of the water quality and trophic status of the Kara Sea.

2.2.2.2 Remote Sensing Observations of the Biogeochemical Features in the Kara Sea

In our pilot studies dating back to 2003 (Pozdnyakov et al. 2005) we used MODIS images taken between August 2 and 12 and processed them with the BOREALI algorithm in conjunction with the Kondratyev et al. hydrooptical model (Chap. 1).

Due to the interference of cloudiness over the Kara Sea in August 2003, only fourteen MODIS images proved to be useful, but none of them was completely free of cloud-screened areas. To obtain spatial distributions of the CPAs (i.e. *chl*, *sm* and *doc*) throughout the entire sea, the results of CPA retrievals were merged and respective image mosaics were generated. For all cloud free pixel the mean value of the CPAs were generated as the arithmetic mean of the values obtained in each MODIS scene.

Figures 2.22, 2.23 and 2.24 illustrate the spatial distributions of *chl*, *sm* and *doc*. The highest *sm* concentrations (Fig. 2.23) are mainly confined to the Ob and Yensei

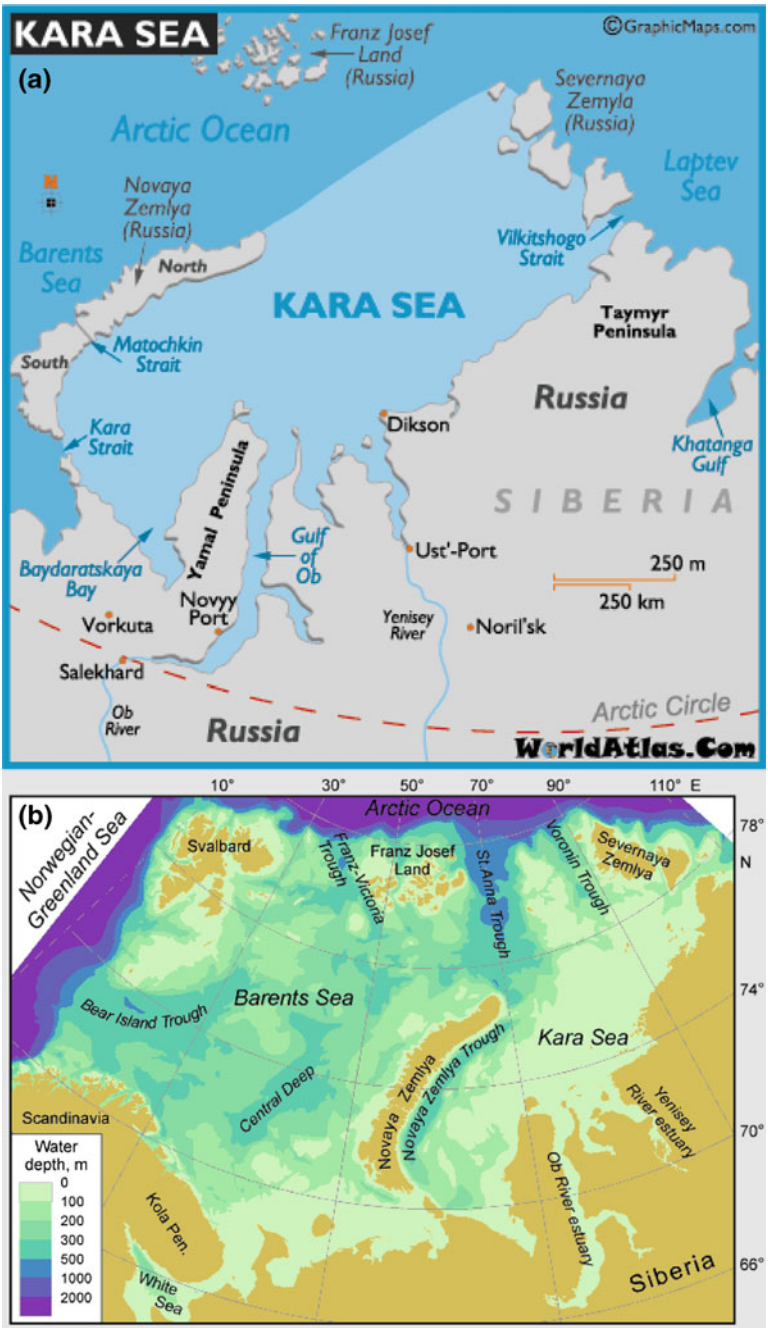

Fig. 2.20 Map (*a*) and bathymetry (**b**) of the Kara Sea (wikipedia.org)

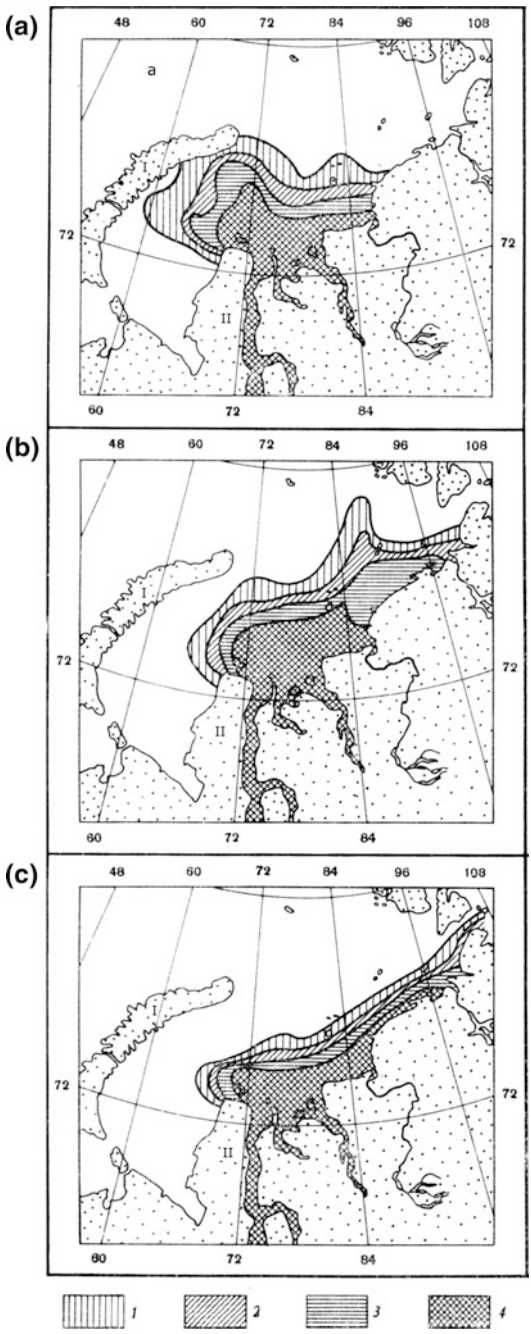

Fig. 2.21 Types of patterns of spread of river runoff waters throughout the Kara Sea in summer: **a** fan-like, **b** northern, **c** eastern; the numbers in the legend stand for: *1* 70–50%; *2* 70–80%; *3* 80–90%; *4* > 90% of desalination of marine waters. Roman numerals 1, and 2 stand, respectively, for Novaya Zemlya and the Yamal Peninsular

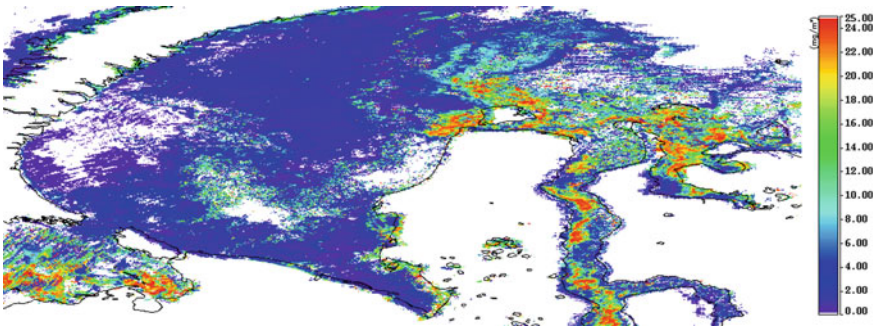

Fig. 2.22 The temporally averaged distribution of *chl* as retrieved from the MODIS images over the Kara Sea during the period 5–12 August 2003

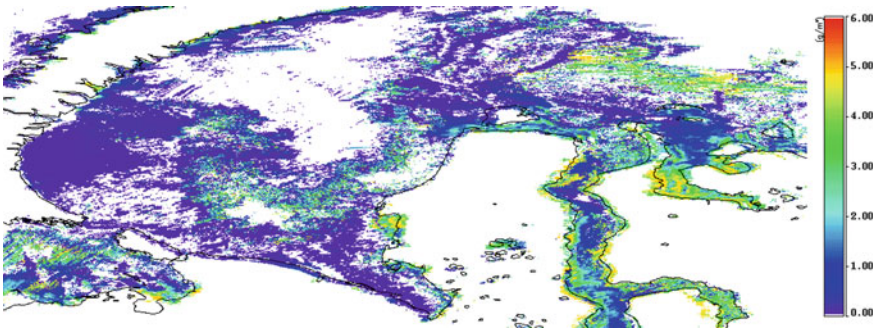

Fig. 2.23 The temporally averaged distribution of *sm* as retrieved from the MODIS images over the Kara Sea during the period 5–12 August 2003

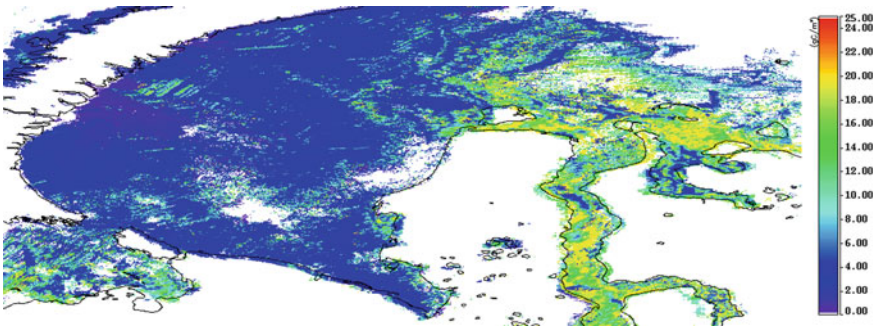

Fig. 2.24 The temporally averaged distribution of *doc* as retrieved from the MODIS images over the Kara Sea during the period 5–12 August 2003

estuaries, in particular to the near shore areas therein. The concentration of *sm* proves to be far less abundant in the central and off-shore parts of the Kara Sea. Somewhat enhanced concentrations of *sm* in the northwestern marine region are probably owing to the immediate proximity to the eroding coastline of Novaya Zemlia. The distributions of *chl* (Fig. 2.22) and *doc* (Fig. 2.24) both exhibit a more patchy structure within the estuaries and a more significant off-shore extension into the Kara Sea. Based upon these data, our overall assessment indicates that the impact of the sediment transport in the surface layer is rather locally confined to the estuaries and their mouth regions. Nevertheless, the plankton blooms, as expressed through high *chl* concentrations, occur both locally in the estuaries and further offshore in the Kara Sea.

The *chl* concentration distribution in the Kara Sea as resolved in our processed MODIS data, indicates that in the summer of 2003 the predominant winds determined a distinctively eastern surface layer spread of the river runoff waters from the Ob and Yenisey Rivers (see section 2.2.2.1). The concurrent spatial distributions of *sm* and *doc* in particular comply very well with this corollary: both constituents are most abundant to the east from the Ob River estuary and adhere to the coastal zone between the Yamal Peninsular and Severnaya Zemlya.

Accordingly, the northern area of the southwestern region of the Kara Sea (west of the Yamal Peninsula in Fig. 2.20a) is rather devoid of any impact of riverine waters. It is poorly productive, and the *doc* and *sm* concentrations are very low.

At the same time, as seen in the low left-hand part of Figs. 2.22 and 2.24, the nutrient rich and warmer Barents Sea waters form the area of respectively high and appreciable *chl* and *doc* concentrations, thus confirming a rather high trophic level of this aquatic area.

These satellite data indicate the presence of large areas with enhanced concentrations of *chl* in the southwestern region of the Kara Sea. It extends from the Karskie Vorota Strait to the northern coast of the Yamal Peninsular. As has been pointed out above, there is a persistent cyclonic circulation in the south-western part of the Kara Sea entraining the productive Barents Sea waters off the northern part of Novaya Zemlya down to the Kara Strait and then further up to the Yamal Peninsular.

The CPA concentrations retrieved by our algorithm can be qualitatively compared with field observations of *chl*, *doc* and *sm* distributions in the Kara Sea (Nöthing et al. 2003; Köhler et al. 2003; Gaye-Haake et al. 2003).

The *chl* concentrations as retrieved from the MODIS data (Fig. 2.22) vary in rather wide ranges, reaching in some locations values as high as 23 $\mu g\ l^{-1}$. According to Nöthing et al. (2003) in some years (e.g. 1999) in situ measurements gave *chl* maximum concentrations up to 13–15 $\mu g\ l^{-1}$.

The retrieved *doc* concentrations also are highly variable with the maximum values up to 20 $mgC\ l^{-1}$. The available in situ data (Kohler et al. 2003) indicate that the maximum *doc* levels were registered at $\sim$13–15 $mgC\ l^{-1}$. This points to the tendency of the ocean color data to overestimate the desired water quality parameters. However, satellite data resolve better the relative spatial distributions in the CPAs.

According to our retrievals, in some areas of the Kara Sea the maximum *sm* concentrations are 3–4 mg l^{-1}. Gaye-Haake et al. (2003) report that the total suspended matter in the waters of the region under discussion can be up to *ca* 4.7 mg l^{-1} with the inorganic component accounting for up to *ca* 72%.

Thus, the above comparisons of in situ and retrieved data indicate that the spatial patterns in *chl*, *sm* and *doc* distributions comply closely with the known oceanographic data. Discrepancies in the absolute values of in situ measured and retrieved concentrations of CPAs are believed owing to the fact that the hydro-optical model used in our algorithm has not been developed specifically for the Kara Sea. This inevitably is bound to introduce some systematic retrieval errors, leaving, however, the general features of the CPA spatial distribution patterns quite adequate.

Consequently, the simultaneously recovered spatial distributions of *chl*, *sm* and *doc* (Figs. 2.17, 2.18 and 2.19) are believed to be the first simultaneous mapping of these three WQP fields in the Kara Sea obtained from optical satellite Earth observation data reflecting the impact of river discharge impact on the trophy of the sea.

Interestingly, the numerical simulations performed with IO RAS model indicate (see Chap. 5) that the initial (still under-ice) growth of phytoplankton (their concentration in the model is measured in mgN m^{-3}) starts in May and located along the western coastline of Novaya Zemlya as well as in the southwestern Kara Sea. It implies that at this stage of the Kara Sea vegetation dynamics, the Barents Sea waters play a leading role. Figure 2.25 illustrates that the phyplankton bloom propagates with the currents moving northward along both coasts of Novaya Zemlya (see section 2.2.2.1), and in late May the bloom occupies a vast area

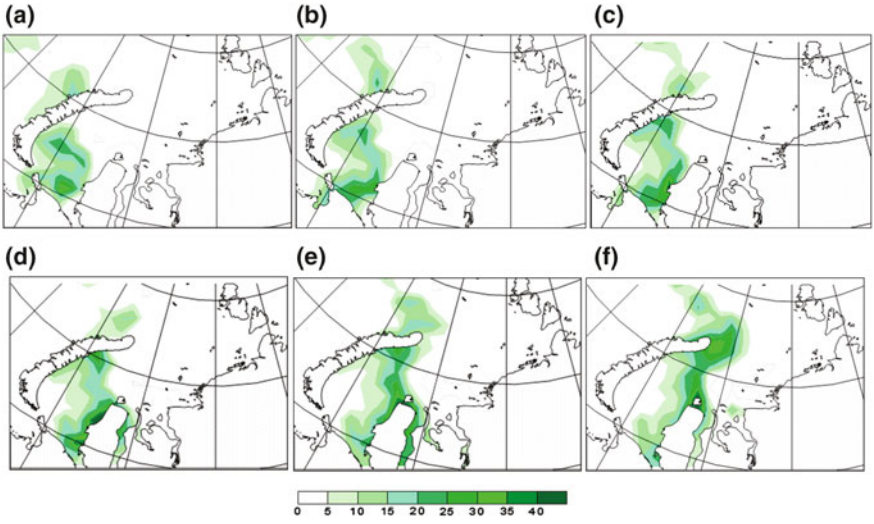

Fig. 2.25 Temporal variations in the concentration of diatomic phytoplankton in May as simulated for 2007. 1—02.05; 2—07.05; 3—12.05; 4—17.05; 5—22.05; 6—27.05 (modeling results)

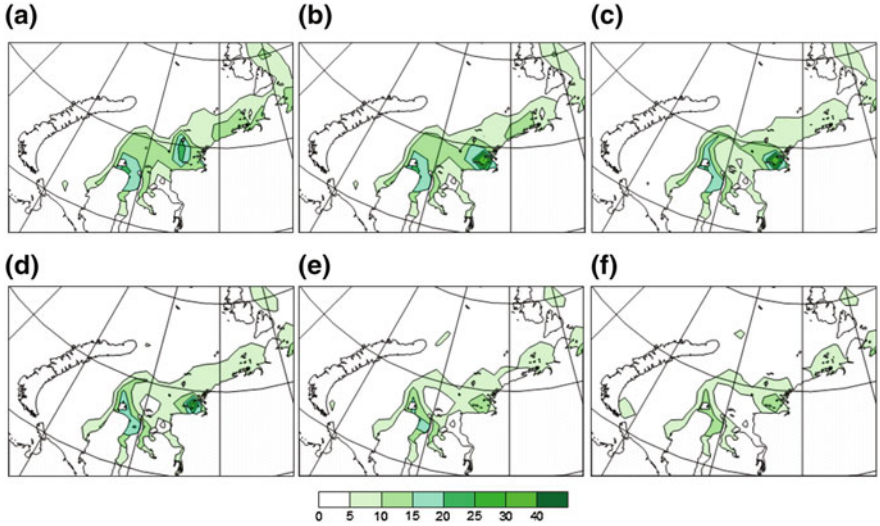

Fig. 2.26 Temporal variations in the concentration of diatomic and flagellate phytoplankton in August simulated for 2007 in August. 1—02.08; 2—07.08; 3—12.08; 4—17.08; 5—22.08; 6—27.08 (results of numerical simulations)

extending from the extreme northern end of Novaya Zemlya till the Yamal Peninsular.

Figure 2.26 illustrates the simulation results for the phytoplankton bloom spatio-temporal dynamics within the ice-free tracts in August. Obviously, at this time the bloom is conditioned by the Ob and Yenisey Rivers, and extends due to the prevailing current (see section 2.2.2.1) to the right along the coast till Severnaya Zemlya. It is noteworthy, that a mere comparison of spaceborne (Fig. 2.17) and simulated (Fig. 2.26) spatial distributions of the phytoplankton bloom in August are appreciably very similar.

Further on in September (Fig. 2.27), the bloom retains its general lay, but more restricted to the coastline and exhibits three centers with enhanced concentration of phytoplankton: these centers are localized at the three main bays in the Kara Sea (Gydansky, Yenisey and Pyasinsky, see section 2.2.2.1).

In October (Fig. 2.28) the life cycle of phytoplankton gradually comes to its end. The bloom area progressively shrinks while the biomass rapidly declines.

Presently it is widely acknowledged (e.g. Carroll et al. 2004) that the role played by *doc* in both the ecology of the world's oceans and global climate is highly essential. In particular, its allochthonous component coming into peripheral seas and inland water bodies with river discharge controls annual fluxes of nitrogen, phosphorus, iron as well as some other nutrients. In marine and lacustrine waters the river-borne nutrients under the action of lytic processes of various nature undergo transformations and acquire chemical forms suitable for the uptake by phytoplankton.

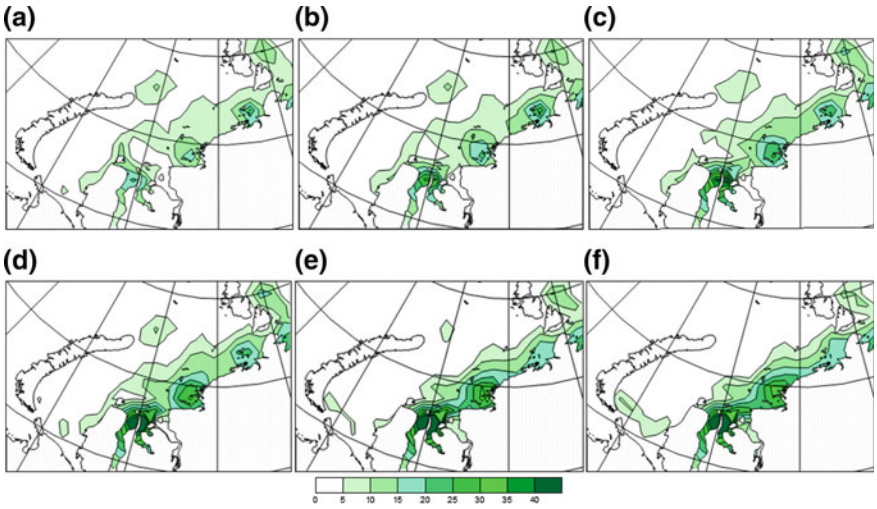

Fig. 2.27 Temporal variations in the concentration of diatomic and flagellate phytoplankton in September simulated for 2007 in September: 1—02.09; 2—07.09; 3—12.09; 4—17.09; 5—22.09; 6—27.09 (results of numerical simulations)

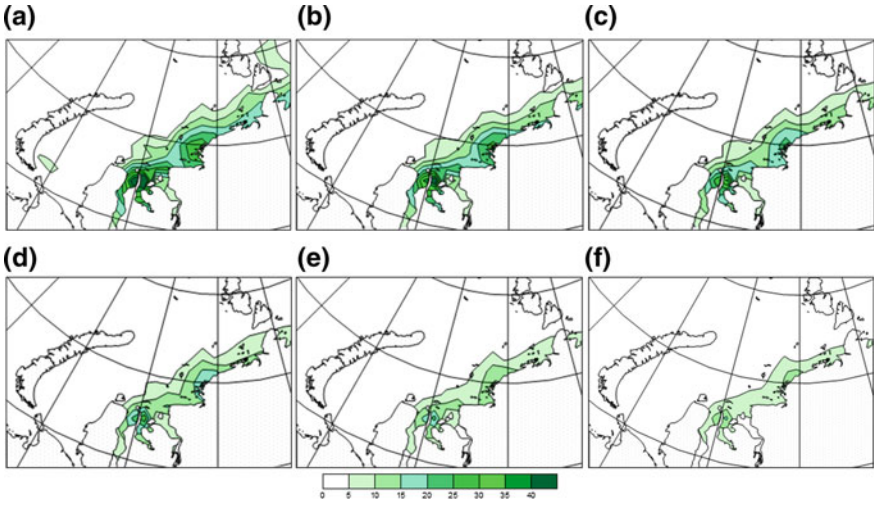

Fig. 2.28 Temporal variations of concentration (mgN m^{-3}) of diatoms plus flagellates in 2007 in October 2007: 1—02.10; 2—07.10; 3—12.10; 4—17.10; 5—22.10; 6—27.10 (results of numerical simulations)

The Siberian sector of the Arctic coastal zone possibly play the determining role in procurement of carbon not only into the Basin of the Arctic Ocean (Stein et al. 2003), but also into other oceans due to the typical of the Arctic basin formation of

deep waters and their entrainment into the global conveyer circulation. Therefore, a quantitative assessment of actual fluxes of organic carbon into the Arctic Basin due to rivers, first of all most fullflowing ones, is important not only on a regional but also the global scale.

Quantitative Assessment of *doc* Fluxes

We applied our biooptical algorithm combining the Levenberg-Marquardt and NN techniques (Chap. 1) to investigate the fluxes of riverine and autochronous *doc* fluxes across the Kara Sea (Korosov et al. 2011).

The available reports in the literature indicate that the waters of the Gulfs of Ob and Yenisey are mixed down to the bottom (Kohler et al. 2003). Hence, the *doc* distribution observed from space making use of our processing tools is practically the same from surface to bottom. Assuming that in river estuaries the entire *doc* is allochthonous (drained from the catchment area), the flux of the allochthonous *doc*, F_{DOC}^{Al} (expressed in thousands of tons of carbon per month, 10^3 tC month^{-1}) is a product of the *doc* (gC m^{-3}) monthly mean concentration and the river runoff, D (expressed in km^3 month^{-1}):

$$F_{DOC}^{Al} = \mathrm{C}_{doc} D. \tag{2.2}$$

This relationship was used for calculating the *doc* fluxes from the Ob and Yenisey Rivers. The values of D were taken from the literature (Kohler et al. 2003; Stein et al. 2003).

The phytoplankton (PH) biomass, BPH (in mg of wet mass contained in a cubic meter, mgPH m^{-3}) has been numerically assessed in three stages. Firstly, the MERIS data were used to calculate the mean phytoplankton biomass in a unit volume in the water top layer:

$$B_{\mathrm{PH}} = K\mathrm{C}_{chl,}, \tag{2.3}$$

where C_{chl} is expressed in mg *chl* m^{-3}, K = 500 is the proportionality coefficient (mgPH μg chl^{-1}) established for the Kara Sea from in situ measurements for the ice-free period (Lavrentieva and Bulion 1984). Secondly, the phytoplankton biomass was calculated at a number of depths within the photic layer by means of multiplying the top-layer phytoplankton biomass by a coefficient corresponding to the considered depth. The vertical profile of this coefficient was drawn taking into account the average data on the Kara Sea vertical distribution of phytoplankton obtained in situ in 2007 and 2008 and reported in the literature (Druzhkov and Druzhkova 1999; Makarevich and Larionov 1999; Larionov and Kodina 2000; Larionov and Makarevich 2000; Nothig et al. 2003). The coefficient is equal to 1 at the surface, lower it rapidly decreases down to ~0.1 at the depth of 12 m, and further on retains this value till at least the depth of 20 m.

To quantify the production of autochthonous *doc*, which is formed as a result of egestion by the phytoplankton in the course of their life cycles, layered values of the phytoplankton biomass were integrated over the entire photic zone for calculating columnar biomass to which the production of autochthonous *doc* must be proportional to phytoplankton biomass. However it proved to be variable depending on the season, geographic location of the water body as well as meteorological, hydrological and biogeochemical conditions.

Nonetheless, for approximate assessments of fluxes of autochthonous *doc*, F_{doc}^{AU} (measured in mgC month^{-1}) the following relationship can be used:

$$F_{doc}^{AU} = K_{\mathrm{PH}} B_{\mathrm{PH}}, \tag{2.4}$$

where K_{PH} is proportionality coefficient (mgC mgPH^{-1} month^{-1}), and B_{PH}, as above, is the phytoplankton biomass.

The value of K_{PH} is obtained empirically (Bardan and Korneeva 2006) for specific conditions (region, season, dominant phytoplankton species, etc.). Thus, satellite data on phytoplankton biomass can be employed to numerically assess the autochthonous *doc* flux given the value of K_{PH}.

Figure 2.29 shows the mean monthly spatial distribution of *doc* (mgC l^{-1}) for July, August and September, 2007.

For the spatio-temporal variability of *doc* across the Kara Sea it is typical that it is conditioned by the propagation of riverine waters: high concentrations of *doc* (12–15 mgC l^{-1}) in the Gulfs of Ob and Yenisey are distributed rather homogeneously in both time and space. Two areas of *doc* high concentrations occurred in August in both the innermost part of the Gulfs of Ob and Yenisey within the zone of mixing of riverine and marine waters (east of Bely Island). Unlike *chl* (Fig. 2.22), enhanced concentrations of *doc* are not observed at distances exceeding 200 km off the outlet of the Gulf of Ob. This is because *doc* acts like a conservative admixture, whose content in the water column declines with the increasing distance from the estuary, whereas *chl* is generated in phytoplankton cells in both off-coastal and pelagic waters.

With due account of the Kara Sea morphometry (see Fig. 2.20b), water masses and the system of currents (see section 2.2.2.1) as well as in light of the revealed specific features of *chl* and *doc* fields, we discriminated 8 zones (Fig. 2.30 and Table 2.2). Application of the procedure of averaging permitted to obtain mean *chl* and *doc* concentrations in July, August and September 2007–2008 in each of the above zones (Fig. 2.30). The results illustrated in Fig. 2.31 reflect the general regularities and tendencies in the seasonal and interannual dynamics of *chl* and *doc* fields. Because of cloudiness, no reliable data for September 2007 could be obtained: that is why they are missing in the respective figures.

Maximum mean concentration of *chl* and *doc* are observed in summer in the Gulf of Ob ($\sim$30 μg l^{-1} and 12.30 μg l^{-1}, respectively). Slightly lower concentrations are recorded for the Gulf of Yenisey ($\sim$25.30 μg l^{-1} and $\sim$10 mgC l^{-1}, respectively), which is most likely because the Gulf of Yenisey is less enclosed, and hence is subject to intense processes of marine and riverine water mixing.

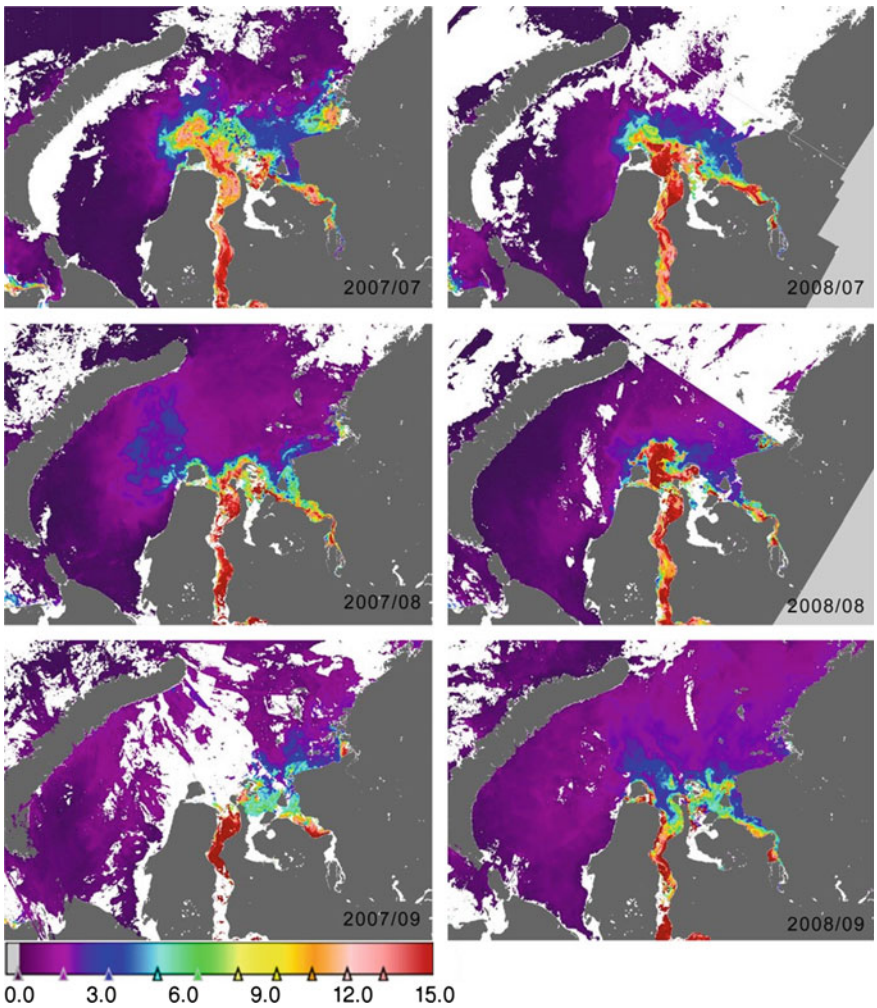

Fig. 2.29 Mean monthly spatial distribution of *doc* (mgC l^{-1}) in July, August, and September 2007 and 2008

In open/essentially off-coastal waters of the Kara Sea, the concentrations of *chl* and *doc* are significantly reduced ($\sim$2 μg l^{-1} and $\sim$1 mgC l^{-1}, respectively). However, the seasonal dynamics of averaged concentrations of *chl* and *doc* is expressed, and is dependent on the specific zone. In the Gulf of Ob, the content of *chl* and *doc* either remain nearly stable or slightly increased. This can be explained by the fact that surficial waters in the Gulf of Ob practically do not mix with marine waters: their chemism is not appreciably influenced by such seasonal factors as wind action and advection.

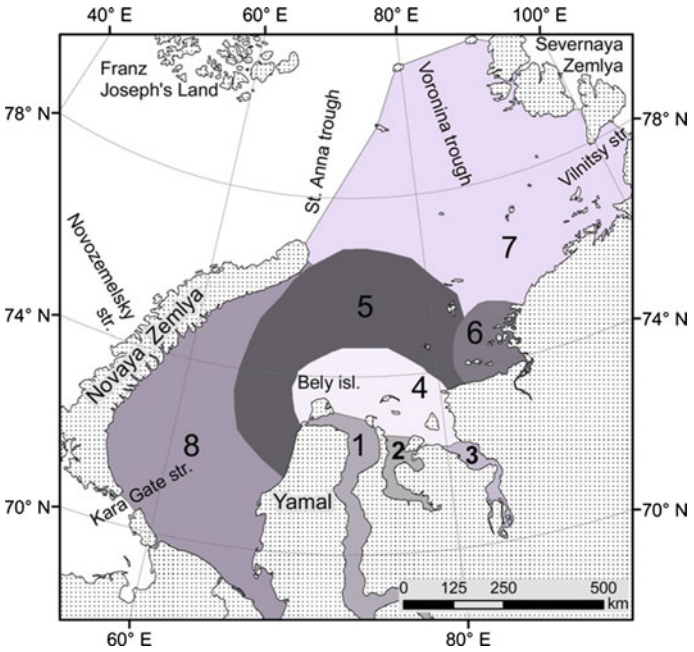

Fig. 2.30 Scheme of the Kara Sea zonation. The numbers stand for: *1* the Gulf of Ob, *2* Gydansky Bay, *3* the Gulf of Yenisey, *4* Zone of mixing riverine and marine waters, *5* Zone of a weak influence of river discharge, *6* Pyasinsky Bay, *7* the Eastern Kara Sea, *8* the Western Kara Sea

Table 2.2 Distigishing features of the discriminated zones in the Kara Sea

Zone	Water salinity	*doc*, mgC l^{-1}	Depth, m	Mixed layer depth, m
1	0–5	12–15	5–10	–
2	0–10	6–15	7–15	–
3	0–10	10–15	1–10	–
4	10–20	2–7	5–20	5–10
5	25–30	0.1–2	20–70	5–15
6	10–20	0.5–8	300	–
7	28–32	0.5–1	5–5	15–30
8	28–32	0.5	300	15–30

In 2007 in the Gulf of Yenisey, a certain increase in *chl* and *doc* during July–September was observed. Contrarily, in 2008 the content of these substances decreased during the above months. Given that the Gulf of Yenisey is less enclosed, it would be reasonable to expect some decrease of *chl* and *doc* with decreasing runoff. However, high north-westerlies in August, 2007 hampered the propagation of riverine waters out in the open sea: these winds "locked up" riverine waters in the Gulf of Yenisey with a result of the aforementioned enhancement of *chl* and *doc* concentrations.

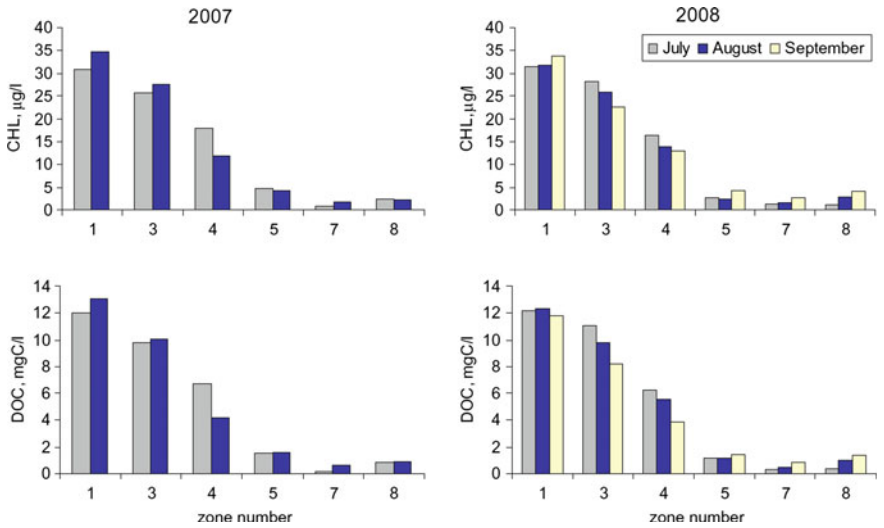

Fig. 2.31 Spatial and temporal dynamics in *chl* and *doc* through July–September. Numbers on the horizontal axis stand for the zones listed in Table 2.2 and illustrated in Fig. 2.30

A certain decrease in *chl* and *doc* is observed within the zone of mixing of riverine and marine waters. This is thought to be due to both a decline of river runoff from July to September and a lessened influence of wind action because of a larger area of this zone.

In open waters, the concentrations of *chl* and *doc* slightly grow, possibly, as a result of the phytoplankton biomass augmentation spurred by rising of deep waters rich in nutrients.

Assumingly the *doc* increment is produced by its autochthonous component. The interannual dynamics (2007–2008) shows itself in the spatial distributions of *chl* and *doc* and is driven by varying winter patters. However, when averaged over the individual zones (Table 2.1), the overall effect is rather mild.

Quantitative assessment of the allochthonous doc flux. Mean monthly values of coloured dissolved organic carbon, *cdoc* in July, August and September, 2007 and 2008, retrieved from satellite data collected over the Gulfs of Ob and Yenisey were employed for quantifying the flux of allochthonous *doc*, F_{doc}^{AL} from the Ob and Yenisey Rivers into the Kara Sea. The obtained values we compared (Table 2.3) with the *doc* flux mean monthly values calculated on the basis of multi-year shipborne measurements conducted in the estuaries of these rivers during the period 1980–2003 (Kohler et al. 2003; Amon and Spitzy 1999; Carroll et al. 2004; Gebhardt et al. 2004).

The above comparison indicates that the *doc* flux calculated by us for the Ob River is by about 250×10^3 tC month^{-1} higher than that reported in the literature. For comparison, in the case of the Yenisey River, such an overestimation constitutes 50×10^3 tC month^{-1}.

Table 2.3 Allochthonous *doc* flux numerically assessed using in situ and remote sensing data

River	Month	River runoff, km^3	F_{doc}^{AL}, 10^{-3} tC $month^{-1}$		
			in situ	Spaceborne, 2007	Spaceborne, 2008
Ob	November–April	82.3	300		
	May	39.5	360		
	June	90.4	980		
	July	79.6	720	958	970
	August	53.5	410	701	658
	September	32.4	210	*514*	381
	Annual	406	3120		
Yenisei	November–April	132.5	480		
	May	77.4	660		
	June	9201.8	2180		
	July	64.3	620		
	August	41.9	380	632	708
	September	41.3	340	420	411
	October	34.9	200	493	339
	Annual	594	4.860		

The entry in italic (the flux assessed for September 2007) is dubious because of frequent overcast conditions

Spatial and temporal dynamics of the phytoplankton biomass (B_{PH}). We used our data on spatial distribution of *chl* for calculating the phytoplankton biomass, firstly, in the top layer. Integration over the water column yielded the columnar biomass, B_{PH}. Our analysis of the obtained results indicates (Fig. 2.32) that maximum values of B_{PH} (>120 gPH m^{-2}) occur in the zone of mixing of riverine and marine waters to the north of the Gulf of Ob Bay.

In the Gulfs of Ob and Yenisey as well as in the open regions of the Kara Sea, B_{PH} is lower (varies between 0 and 50 gPH m^{-2}). Such a distribution is thought to be due to a combined action of two factors: in the region of maximum B_{PH}, the *chl* concentration is fairly high ($\sim$30 μg l^{-1}), whereas the depth is under 20 m. Thus, integration over the entire euphotic depth yields higher values of B_{PH} compared to shallow waters. The obtained distribution is generally in qualitative agreement with in situ measurements of B_{PH} (Nothig et al. 2003; Druzhkov and Druzhkova 1999; Larionov and Kodina 2000).

Seasonal and interannual dynamics of B_{PH} distribution is fairly significant: in 2007 the maximum of B_{PH} is distinctly expressed in the inner-most part of the Gulf of Ob both in July and August; whereas in 2008 it is located to the north from the 2007 position and in August it further shifts in the direction to the open sea.

The observed from space spatial distribution of the phytoplankton biomass controls mean values of B_{PH}, calculated for each discriminated zone. Mean water

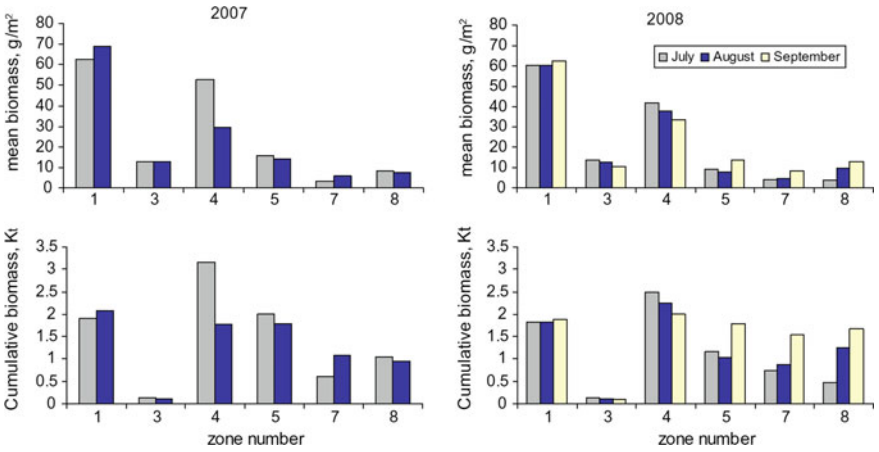

Fig. 2.32 Spatial distribution of the phytoplankton columnar biomass ($g\ m^{-2}$) during July-September in 2007 and 2008. Numbers on the horizontal axis stand for the zones listed in Table 2.2 and illustrated in Fig. 2.30

columnar B_{PH} values were further employed for calculating the zone cumulative phytoplankton biomass by multiplying by the zone area. The most enhanced values of monthly mean phytoplankton biomass are revealed in the Gulf of Ob (1900 tPH), in the zone of mixing of riverine and marine waters (2300 tPH) and in the zone of fresh water weak influence (1500 tPH). In these zones, we observed either high concentrations of *chl* or the zone area is large. In the open waters of the Kara Sea, the total monthly mean biomass is slightly less constituting ca 1000 tPH. The contribution of the Gulf of Yenisey is minimum ($\sim$120 tPH).

The total biomass produced in the Kara Sea during the 3 months amounts up to 25 and 23 thousand tPH in 2007 and 2008, respectively.

Determination of the coefficient employable for calculating the production of autochthonous DOC from the phytoplankton biomass. There are in situ data available at the Marine Biology Institute (Murmansk, Russia) on both the seasonal autochthonous production of *doc* and the monthly mean biomass of phytoplankton (measured as the carbon content in a unit volume, $\mu gC_{PH}\ l^{-1}$) in the Kara Sea. Since the units of the available in situ phytoplankton biomass are incompatible with those provided by satellite data (assessed through the content of phytoplankton *chl*), we could not either compare directly both sets of data or use in situ data for determining the coefficient K_{PH} from Eq. 2.4.

However, as is shown below, firstly, we exploited the in situ data for an indirect assessment of the total autochthonous *doc* production over the months of observations (July, August, September), and then the satellite data were used for calculating the sought for coefficient.

According to the above in situ data collected in summer (Table 2.4), the *doc* egested by phytoplankton accounts for 1433×10^3 tC $month^{-1}$ (Grassl et al. 2007). At the same time, mean phytoplankton biomass in summer (June, July,

Table 2.4 Numerical assessment of the total autochtonous *doc* production per month in the Kara Sea (employing the in situ data of the Mumansk Marine Biology Institute)

Time period	Phytoplankton biomass, $\mu gC_{PH}\ l^{-1}$	Total autochtonous production of *doc*, tC
Summer mean (June, July, August)	921	1433
July	110	1750
August	78	1200
September	29	450
Cumulative for the period of satellite observations (July, August, September)		3400

August) is 921 $gC_{PH}\ l^{-1}$ (Table 2.4). To calculate the monthly *doc* production not only for summer but also for the period of satellite monitoring (July, August, September), we divide seasonal *doc* production by seasonal phytoplankton biomass values and multiply by monthly biomass values (Table 2.4).

In the next stage, we determine the summer cumulative *doc* production during the period of satellite observations, which proved to be 3400 tC (Table 2.4). The cumulative phytoplankton biomass yielded by satellite measurements for the same time-period constituted in 2007 and 2008, respectively, 25 and 23 thousand tons of phytoplankton. Averaged over two years, the ratio of the cumulative *doc* production to the cumulative phytoplankton biomass, yields the value of K_{PH} equal to 142 ± 8 gC gPH $month^{-1}$.

The mean autochthonous *doc* production (in 10^3 tC $month^{-1}$) in the Gulfs of Ob and Yenisey, calculated using Eq. 2.4 and the above value of K_{PH} is about 280 and 18, respectively.

Assessment of the Allochthonous and Autochthonous Components of the Total *doc* Flux

It is not unreasonable to suppose that the *doc* flux quantified above is, indeed, the total *doc* flux, F_{doc}^{AL}. In this case, the flux of sole allochthonous component, (F_{doc}^{AL}) is the difference between F_{doc}^{AL} and F_{doc}^{AL} calculated from the phytoplankton biomass (Eq. 2.4).

A comparison with the respective in situ data (Table 2.5) indicates that the difference between spaceborne and shipborne F_{doc}^{AL} is $\sim 30 \times 10^3$ tC $month^{-1}$ (11%) and 35×10^3 tC $month^{-1}$ (8%) for the Ob and Yenisey Rivers. Indirectly, this result reinforces the developed approach of quantitative determination of both doc components and the value of K_{PH}.

Thus, employing Eq. 2.4 and the determined K_{PH}, we could calculate more accurately the both components of doc fluxes in Kara Sea reaching a better agreement with in situ data.

Table 2.5 Mean values of the total, autochthonous, and allochthonous, fluxes as quantified according to the suggested methodology

River	Month	Flux of *doc*, thousand tons of carbon per month			
		Remote sensing data			in situ
		Total	Autochtonous	Allochtonous	Allochtonous
Ob	July	960	216	743	720
	August	675	227	447	410
	September	445	246	198	210
Yenisey	July	665	15	649	620
	August	415	14	400	380
	September	410	16	393	340

2.2.3 Barents Sea

2.2.3.1 General Characteristics

The Barents Sea (BS) is a marginal sea of the Arctic Ocean located off the northern coasts of Norway and Russia (Ecosystem Barents Sea 2009). The BS is bordered by the shelf edge of the Norwegian Sea to the west and the Archipelagos of Svalbard to the northwest, Franz Josef Land and Novaya Zemlia to the northeast, with the central point located at 75°N 40°.

The morphometry of the BS is very uneven: the average depth is ~300 m plunging to a maximum of 600 m in the major Bear Island Trench.

Due to its geographical layout and specific morphometric features (Fig. 2.28), the BS plays an exceptionally important role in determining the general thermo-hydrodynamic and hydrobiological conditions across the Arctic Basin.

There are three main types of water masses in the Barents Sea: warm, salty Atlantic water (temperature > 3 °C, salinity > 35 psu) from the North Atlantic drift, cold Arctic water (temperature < 0 °C, salinity < 35 psu) from the north, and warm, but not very salty coastal water (temperature > 3 °C, salinity < 34.7 psu).

The BS is characterized by a relatively shallow shelf and fairly complex hydrography: it is subjected to a very strong dynamic influence of both the Arctic Basin and the Atlantic waters, and thus constitutes an arena of very intricate hydrodynamic interactions of water currents (Fig. 2.33). The main water exchange route is between the Barents Gates and the Trough of St. Anna (Fig. 2.34).

Between the Atlantic and Polar waters, a front called the Polar Front (PF) is a permanent feature. In summer it is located at 78°N–80°N extending amid the BS between the Svalbard Islands and the southern coast of Novaya Zemlia. In the western parts of the sea (close to Bear Island), this front is determined by the bottom topography and is therefore relatively sharp and stable from year to year, while in the east (towards Novaya Zemlia) it can be quite diffuse and its position can vary significantly between years. In spring, the PF structure is frequently affected by mesoscale eddies with typical sizes of 25–40 km and the water vertical velocity mounting to 20 m day^{-1}.

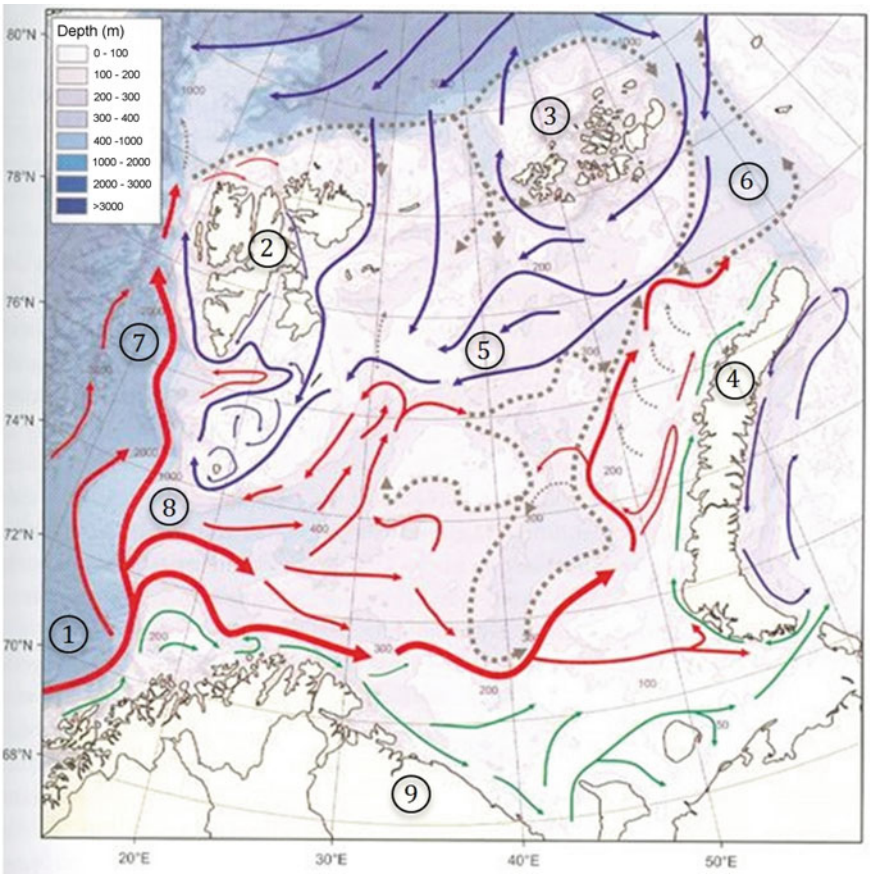

Fig. 2.33 The principal system of surface currents in the BS. *Red*, *blue* and *green arrows* stand for water flows of Atlantic, Arctic and coastal zone origin; *dotted lines* correspond to subsurface currents (The Barents Sea 2011). *1*, *2*, *3*, *4*, *5* designate, respectively, the shelf edge of the Norwegian Sea, the Svalbard Archipelago, Franz Josef Land, Novaya Zemlia, the central point of the BS. *6* Trough of St. Anna, *7* Bear Island, *8* Barents Gates, *9* The Kola Peninsular. Numbers in small fond are depths in meters

As the PF enhances the vertical and horizontal mixing in the region, and hence channels the nutrients up to the euphotic zone, it is a site of high biological activity. It largely explains that, compared to other marine waters of similar latitude, the BS is a relatively productive high-latitude marine ecosystem.

The tidal/ebbing water motions are significant in the Barents Sea with the tidal amplitude and current direction varying greatly. The atmospheric cyclonic activity over the Barents Sea is very pronounced throughout the year.

A significant part of the BS is annually ice-free. In winter (March is the coldest month in the BS basin) the ice-edge is located at ~75°N in the northern and western BS confines. However, in the eastern periphery zone, the ice frontier turns

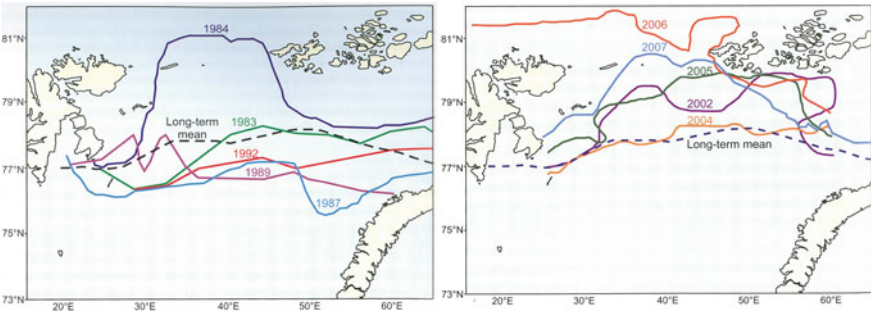

Fig. 2.34 Location of the ice-edge in the BS in various years, and its mean median position over a multi-year period (The Barents Sea 2011). *Dashed line* shows the position of the Polar Front as reported by Reigstad et al. (2002) for July 1999

abruptly to the south reaching the Kola Peninsular coast. This pattern persists till April and even May. During March, an inflow of warm and saline Atlantic waters with the Norway Current and their blending with cold and less saline Arctic waters makes this sea very sensitive to atmospheric, hydrodynamic and, ultimately climate change forcing. In June- September, the ice-edge has a latitudinal placement closer to ~ 77–80°N (Fig. 2.29) (The Barents Sea 2011).

The climatic index of the BS reveals significant interannual variations and a non-linear trend. However, over the last three-four decades there is a distinct indication of climate warming (The Barents Sea 2011).

As to the hydrobiology at low trophic levels, the phytoplankton development does not last long (June–August, very rarely till mid September); the phytoplankton composition is rather variable. It encompasses algae from classes of Bacillariophyta (predominantly), but also Haptophyta, Dynophyta as well as dianoflagelates (Ceratium), depending on the ice regime, daylight duration, and availability of nutrients.

At least during the last decades, extensive blooms of a coccolithophore, *Emiliania huxleyi*, reportedly occur regularly, (although not necessarily each year) in the central and southern regions of the BS. The blooms were observed most frequently in August.

The BS surface *chl* concentration during the vegetation period (April–August, rarely till mid-September) is generally below 1.0–1.5 μg l^{-1} except for the marginal ice zone (MIZ), where it can be in the range ~5 to 15 μg l^{-1} and even higher (Engelsen et al. 2002).

Sea surface temperature (SST) across the BS during the warm period varies generally longitudinally: e.g. the climatological values of SST in June are about −2 °C at the northern boundary of the BS and +5 °C ÷ +6 °C within the Norwegian and Russian coastal zones of the Kola Peninsula (NOAA Atlas 2004), whereas in September the respective values are 0°C and +7°C ÷ +8°C (NOAA Atlas 2004; Parker 2014).

2.2.3.2 Cyclones and Phytoplankton and SST Variability in Time and Space

Deep baric formations in the atmosphere are shown to be able to strongly affect primary production (PP) variations across oceanic/marine tracts (for refs. see Morozov et al. 2014; Tang and Sui 2014). The atmospheric impact on PP is evidenced by quite a number of satellite-based studies employing synergistic approaches. These studies seemingly indicate that the phytoplankton biomass increase provoked by cyclones might arise from a variety in-water processes (Le Fouest et al. 2011).

Predominantly, investigations of cyclone impacts were conducted over low-latitude waters in the northern hemisphere: the Western North Pacific [reportedly, the area of the highest incidence of tropical cyclones (Ying et al. 2012)], and, more specifically, South China Sea, as well as in the Indian Ocean (Bay of Bengal and Eastern Arabian Sea), and northern Atlantic Ocean (Gulf of Mexico and the 24°N–38°N latitudinal belt). This interest in studying specifically low-latitude marine/oceanic tracts is accentuated by the expectations that the incidence of tropical cyclones will steadily grow with ongoing climate warming (Ying et al. 2012).

There are reasons to expect that the effect of deep cyclones on PP in the Arctic Ocean can also be appreciable/consequential (Le Fouest et al. 2011) regardless of the fact that it is a rather low production region of the world's oceans (Arrigo and van Dijken 2011). We are unaware, however, of any satellite-based investigations of this phenomenon at these latitudes.

2.2.3.3 A Concise Overview of Previous Studies

Storm-induced perturbations in the thermohydrodynamic state of the upper ocean were revealed and theoretically investigated back in the 1960s (Leipper 1967). In the early 1980s, airborne means were employed to study the aftermath of hurricane passage, first and foremost, spatio-temporal changes in SST.

Further on, starting from the early 1990s, spaceborne thermal remote sensing came up to largely replace observations from airplanes. In the early 2000s, a synergistic remote sensing approach began to be exploited to widen the scope of variables characterizing this multifaceted phenomenon. It is when the phytoplankton biomass dynamics was found to be one of the very important and highly consequential aftereffects of hurricane translation over oceanic/marine tracts (Robinson 2004).

As mentioned above, the hitherto studies of storm-driven impacts exerted upon upper ocean were nearly entirely confined to low latitudes that are the realm of tropical cyclones/hurricanes/typhoons (Tang and Sui 2014). The latitudinal belt within which the investigations were mostly performed extends between 4°N and 30°N with the only exception of the Sea of Okhotsk (45°N–50°N), which is also studied in connection with the invasion of tropical cyclones (Salyuk et al. 2014).

Similar reports from the southern hemisphere oceans are scarce and mainly target various issues related to SST (see e.g. Jullien et al. 2012).

The studies alluded above revealed that the maximum rainfall and SST cooling are, respectively, in the left and right side parts of the cyclone track. Moving cyclones cause (i) subduction by several tens of meters of the upper quasi-homogeneous layer, (ii) deepening of mixed layer depth, (iii) a hike in primary production (PP) and CO_2 efflux (outgassing) from the ocean to the atmosphere, and (iv) a rise in sea surface height.

These perturbations are thought to be driven by a variety of mechanisms among which are (i) wind mixing (followed by the upward Ekman pumping), (ii) transient upwelling, (iii) entrainment, (iv) bringing of subsurface *chl* to the ocean upper layer, and (v) rapid ventilation of the thermocline and nutricline.

The degree of the perturbations caused by moving tropical cyclones is case/area-specific and varies within rather wide ranges. Thus, the increase in *chl*, and correspondingly PP, reported from the North Atlantic (Hanshaw et al. 2008) was insignificant, whereas in Northwest Pacific the typhoon activity contributed between 0.4 and 40% of summer–fall production (Siswanto et al. 2007). In 2012, also in the North Atlantic, PP reportedly increased by 0.15% due to cyclones.

Interestingly, in an other communication (Lin 2012), of 11 cyclones, the most severe cyclone has not produced any increase in PP. Byjy and Kamar (2011) communicated their finding that the hurricane brought about a relatively low *chl* enhancement (of about 0.5 mg m^{-3}), but a twofold increase in PP in the Bay of Bengal. Rao et al. (2006) report about a cumulative fivefold increase in PP in the same bay due to the cyclone passages, and the increase in *chl* varied from 4 to 9 times. A 2.5 to 3-fold increase in *chl* was established by Walker et al. (2005) in the Gulf of Mexico. Earlier Babin et al. (2004) determined that within the subtropical coastal zone of the US *chl* increased in the range of 5–91% due to strong cyclones. For the South China Sea *chl* increases constituted 30–40 and even 60 times, and PP increments over typhoon periods were 3.5% (Zhao et al. 2008). Kawai and Wada (2011) found that in the waters south of Japan, in the Sea of Okhotsk and in the regions between 35°N and 45°N, especially the Kuroshio-Oyashio Extention (KOE) region, the contribution of cyclones to the annual *chl* increase was generally small; the cyclone induced *chl* increases accounted for a few per cent of the total *chl* increase in some areas. However, a short-term increases accompanied by cyclones provoked 10% to 30% of the accumulated *chl* increase or more in the South China, East China, Yellow, Japan Seas as wells as the Sea of Okhotsk.

Water cooling due to the cyclone passage varied within the range −2–9 °C: −2.5–6 °C in Northwestern Pacific (Lin 2012), −2 °C in the Arabian Sea (Byju and Kamar 2011), −2–3 °C in the Bay of Bengal (Rao et al. 2006; Sarangi 2011), −3–7 °C in the Gulf of Mexico (Walker et al. 2005), −5–9 °C in the South China Sea (Zheng and Tang 2007; Lin et al. 2003).

The lag time between the cyclone passage and ensuing SST and *chl* reaction constituted 3–9 days: 7–9 days in the North Pacific Ocean (Akmaykin et al. 2013), 7 days near the Pearl River estuary and in the Bay of Bengal (Rao et al. 2006),

3–4 days in the Arabian Sea (Byju and Kamar 2011), 3–4 days in the Gulf of Mexico (Walker et al. 2005), 3–6 days in the South China Sea (Liu et al. 2003).

The duration/life-time of the effect is reportedly also very variable ranging between less than 2 weeks and one month: (Akmaykin et al. 2013; Babin et al. 2004; Liu et al. 2003; Zhao and Tang 2006; Zhao et al. 2008, 2009; Kawai and Wada 2011).

Perturbations of SST and *chl* fields grow with increasing above water wind (V); Akmaykin et al. (2013) reported that the effect became noticeable at $V > 33$ m s^{-1}; Hanshaw et al. (2008) found that the increase in wind in the North Atlantic from 16 to 54 m s^{-1} resulted in a 15% greater *chl* response; Babin et al. (2004) reported for the Sargasso Sea that the increase in wind from 40 to 60 m s^{-1} led to a 20% greater *chl* response.

Summing up the findings reported in the publications discussed above, it is possible to generalize that the conditions favoring the impact of hurricanes on SST and *chl* are: deep atmospheric depression (950–980 mb), strong sustained winds above the water surface, low cyclone translation velocity, big cyclone size, absence of warm eddies within the trajectory of cyclone's footprint route, shallow mixed layer depth (MLD), as well as shallow depths of thermocline and nutricline. The impact becomes subdued if two cyclones move consecutively.

Thus, this very brief overview ascertains that the interplay of both atmospheric and oceanic hydrodynamic conditions explains in each concrete case the actual SST and *chl* response to the impact of very strong storms.

2.2.3.4 Remote Sensing Observations

Through the synergistic use of spaceborne optical and microwave data (see Sect. 1.5) nearly one hundred cyclones passing over the BS between early April and late August–early September were registered for the period 2003–2013. As illustrated in Fig. 2.35, the monthly number of cyclones only rarely was in access of 3. Of the overall number of cyclones (96), only 23 were suitable for analysis.

The geopotential height in the "eye" of the 23 selected cyclones varied in the range −187 gmp to −9 gmp. The maximum wind speed above the water surface and the cyclone translation velocity varied within 13–30 and 3–28 m s^{-1}, respectively. A composite presentation of tracts of all 23 cyclones is given in Fig. 2.36.

The direction of propagation of all 23 cyclones is predominantly from west to east. Most of them traversed the BS within the region between southern Spitsbergen and the coastal zone of the Kola Peninsular to eventually go out through a corridor extending from middle to southern Novaya Zemlya. Some of them (lesser in number) leaved the BS waters moving over the summer time Polar Front zone (Fig. 2.36).

Our spaceborne estimations indicate that the intra-seasonal distribution of cyclone incidences is relatively even: the major cases occur during July–August–September. However September, especially its second half, is already a time when the *chl* growth is null.

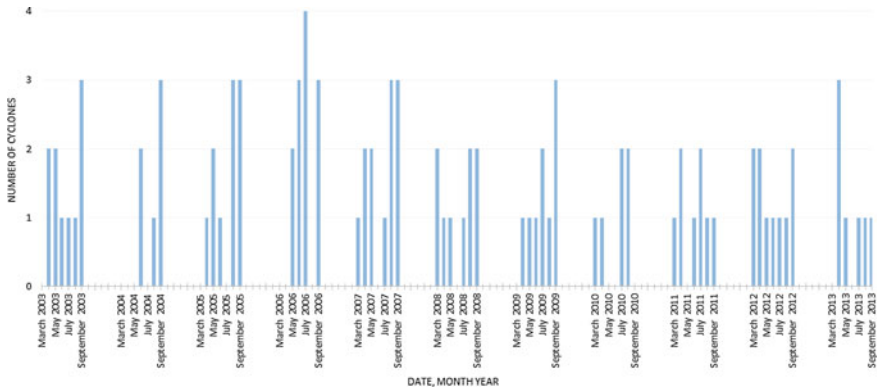

Fig. 2.35 The monthly number of selected cyclones over the BS during the period 2003–2013

It was also found that the distribution of monthly *chl* averaged over the entire BS exhibits a major maximum in late May–early June and a secondary spike in August (Fig. 2.37). Thus, in our analyses we considered the cyclones passing over the BS between April and mid-September assuming this time interval as the BS vegetation season.

There is just one caveat: the absolute values and the placement of the maximum in Fig. 2.37 do not account for the *chl* abundance and temporal dynamics in immediate proximity to the ice-edge. That was done in order to avoid the inaccuracies inevitably arising from the adjacency effect (Sterckx et al. 2011).

It was found for all (i.e. 23) selected cyclones that the fraction of the BS surface covered by the stripe of the moving cyclone footprint varied between 5 and 28% with an average value of about 14%.

Our analysis of *chl* and SST response to moving cyclones indicates that there are two major types of variation patterns that are typical of the BS. The first pattern is characterized, firstly, by a decrease of *chl* that is followed by its enhancement (exemplified in Fig. 2.38).

Illustrated in Fig. 2.39, the second pattern exhibits a short-lived increase in *chl* as well as in SST that is succeeded, firstly, by some growth of both variables, then their decline, and finally a near restitution of *chl* and SST initial (i.e. prior to cyclone passage) values.

The incidence of responses of the first type is more frequent: of all 23 cyclones observed and analyzed there were only 6 cases of the second type responses. For both response types, with respect to the direction of cyclone translation, a more intense surface *chl* enhancement (up to 25%) was observed in the right-hand side of the footprint strip.

Statistical analysis of the *chl* enhancement ($+\Delta chl$, μg l^{-1}) produced by moving cyclones indicates that it significantly correlates with the depression depth (H, gmp) and cyclone translation speed (V, m s^{-1}) with the coefficient of determination equal to 0.75 RMSE = 0.029 [or 16.6%]:

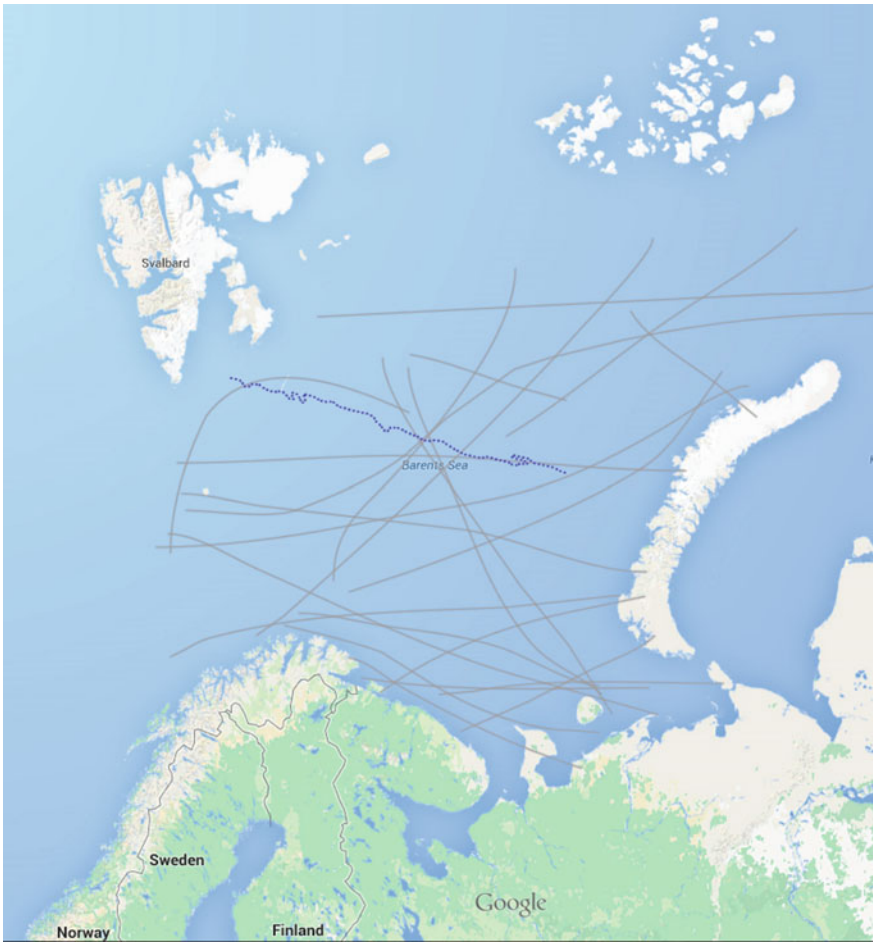

Fig. 2.36 Tracts of the analyzed 23 cyclones in the BS. *Dotted line* exemplifies the summer time location of the Polar Front as reported by Reigstad et al. (2002)

$$+\Delta chl = 0.18 + 0.0052 \cdot H - 0.0007 \cdot V \tag{2.5}$$

In the same vein, the timing of *chl* maximum (see Fig. 2.29a) was significantly ($p < 0.0001$) correlated with the depression depth (H, gmp): the coefficient of determination was equal to 0.56 (RSME = 0.8 [or 47%]):

$$T = 0.89 + 0.0187 \cdot H \tag{2.6}$$

In the cases of response of the first type, the cyclone-driven enhancements of *chl* and SST were in the range (1–2) μg l^{-1} (only rarely reaching 4 μgl^{-1} as it is exemplified in Fig. 2.28) and 1 °C, respectively.

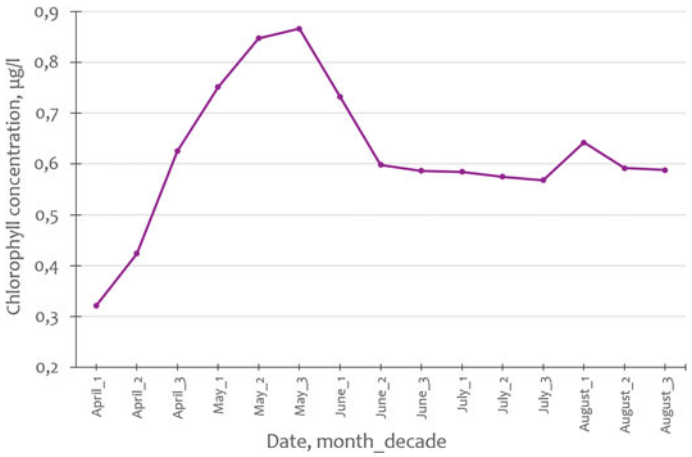

Fig. 2.37 The seasonal variation of *chl* averaged over 10 days and the entire BS area for the time period 2003–2013

The pattern of response of the first type (Fig. 2.38) assumes that although the cyclone's arrival leads (moment A in Fig. 2.38) to inevitable mixing of surface and subsurface layers, the thermal and productivity levels of water within this stratum are very close. However, in the course of several days the cyclone-induced vertical mixing continues propagating lower with a result that a few days after the cyclone onset, the developing vertical mixing brings deeper waters to the surface.

On their arrival to the surface, those deeper waters, being richer in nutrients, find themselves in conditions favorable for phytoplankton development in terms of both water temperature and light availability. It takes a couple of days to appreciably increase the primary production at the surface, which is witnessed by a relatively short-lived spike in *chl*. The lifetime of this spike could not be very long: the pool of newly arrived nutrient resources becomes gradually depleted (point B in Fig. 2.38), eventually bringing *chl* to pre-cyclone values.

The Ekman layer depth (h, m) can be estimated using the following relationship (Chen and Tang 2012):

$$h = 7.12 \cdot \left[\frac{1}{\sqrt{\sin \varphi}}\right].V_{max}, \tag{2.7}$$

where ϕ = latitude (°), V_{max} = maximum wind speed (m s^{-1}) at 10 m above sea level within the footprint area.

For the parameters of cyclones investigated, the Ekman layer depth varied between $\sim$100 m and $\sim$230 m. These assessments indicate that the BS cyclones were actually capable of acting as Ekman pumps entraining waters from very significant depths up to the surface.

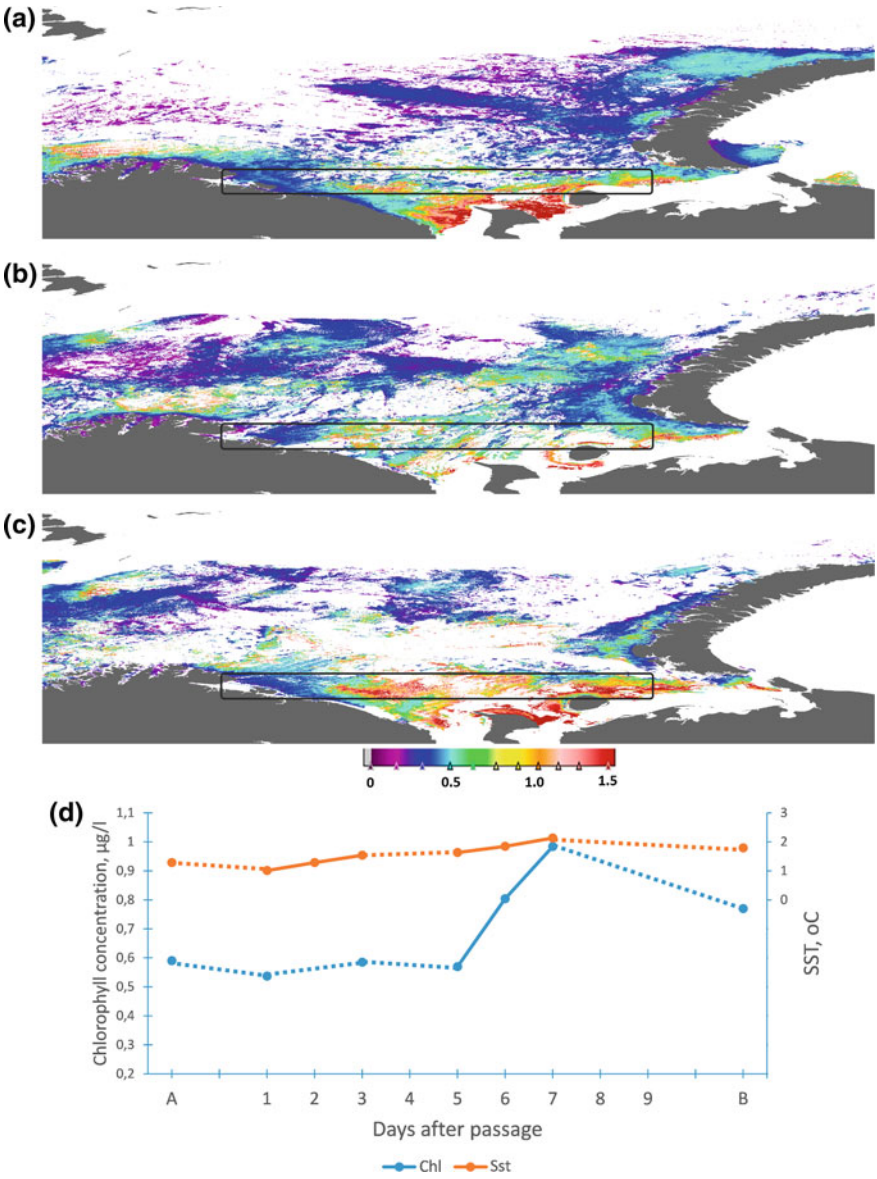

Fig. 2.38 The Barents Sea: 13–14.04. 2012. Spatial distribution of surface *chl* averaged within the cyclone footstep area over **a** 5 days prior to cyclone passage, **b** 5 days after the cyclone passage, and **c** the sixth to ten days after the cyclone passage; graphs **d** illustrate the temporal variations of, respectively, *chl* and SST. Points *A* and *B* on the abscissa designate the period, respectively, 5 days prior to cyclone arrival and 5 days (from the sixth to tenth day) after cyclone departure

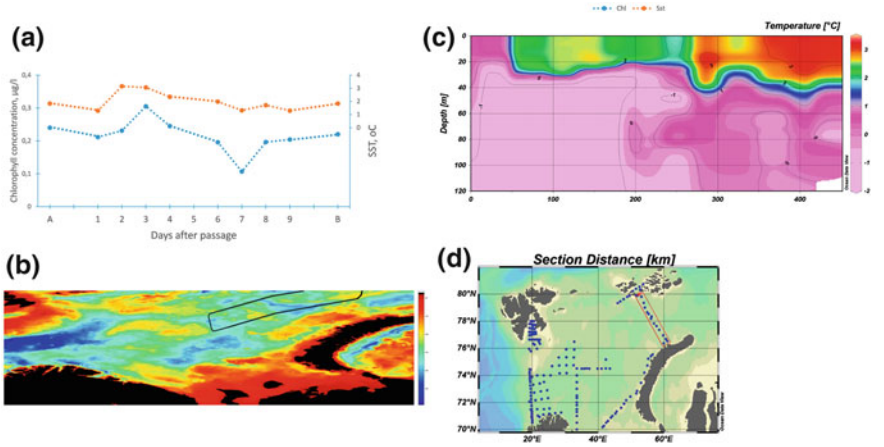

Fig. 2.39 The Barents Sea: 11–12.07.2006. **a** Temporal variations of surface *chl* and SST. Points *A* and B on the abscissa designate the period, respectively, 5 days prior to cyclone arrival and 5 days (from the sixth to tenth day) after cyclone departure, **b** location of the cyclone on the bathymetric map, **c** cross-section of water temperature along the line (**d**) extending from Franz Josef Land to Novaya Zemlya (i.e. the right hand side of plate **c**). The spatio-temporal averaging is performed within the cyclone footstep area

Analysis of the trajectories of cyclones resulted in the first type of response showed that all of them were located within the region encompassing currents originating from the intrusions of Atlantic waters through the Barents Gates (point 8 in Fig. 2.33) and propagating to the east across the BS. Generally, these currents reside in the top ~250 m layer (Reigstad et al. 2002), and drive relatively warm and nutrient enriched waters as compared to both BS proper water sand inflowing Arctic waters.

Thus, the first type response cases should be related to the mechanism suggested above: cyclone-induced pumping of nutrient-rich waters of Atlantic origin to the water surface followed by a relatively short-living enhancement of phytoplankton productivity in the upper layers lasting until the depletion of pools of nutrients brought up from below.

The described sequence is illustrated in Fig. 2.38 (plates a–d). This type of response can be expected to occur within the vast area of Atlantic waters propagating across the southern and central BS (Fig. 2.34). This explains the prevalence of the first type response cases over cases exhibiting the response of the second type.

The suggested mechanism of the first type response can be further underpinned by considerations based on the Redfield ratio paradigm, according to which the stoichiometric ratio of carbon, nitrogen and phosphorus found in the phytoplankton throughout the deep oceans is C:N:P = 106:16:1 (Redfield 1934). The BS nutrient pool is known to be strongly nitrogen limited (The Barents Sea 2011). This can be

exemplified by the results of the field campaigns of two consecutive years conducted by Reigstad et al. (2002) along the Kola Transect: in March (the time when assumingly no consumption does take place, and the nutrient abundance represent true winter concentrations) the N:P ratio in the central Barents Sea and the marginal ice zone (MIZ constituted < 10.4:0.75 as compared to the aforementioned Redfield ratio (16:1), which provides a useful screening criterion.

In the absence of data on biogeochemical shipborne measurements performed during our decadal spaceborne observations of cyclone-driven effects, and in light of the reported studies (The Barents Sea 2011; Reigstad et al. 2002), we assume that the Barents Sea is putatively N-limited.

Smith (2006), assuming the validity of the Redfield ratio and based on a cross-ecosystem comparison of data obtained from 92 marine coastal zone systems worldwide, established a regression model for putatively N-limited sites. In case of availability on data on total phosphorus (TP), the regression equation is as follows:

$$\log chl = 0.99 \log \mathrm{TP} + 0.11, \quad (r^2 = 0.74) \tag{2.8}$$

To apply this relationship, we employed the aforementioned Kola transect shipborne data on TP (Reigstad et al. 2002). The results of our numerical assessments are exemplified in the case displayed in Fig. 2.6 for mid-April and the coastal zone waters of the BS. The concentration of *ch*l prior to the cyclone onset was about 0.6 μg l^{-1}, and the TP value in surface waters putatively constituted 0.4–0.5 μmolTP l^{-1} (Reigstad et al. 2002, their Fig. 4b).

The cyclone impact brought about the increase of *chl*-a up to ~1.0 μg l^{-1}. As a result of associated cyclone-driven vertical mixing (remember that according to our estimations, the cyclones considered in our study were strong enough to mixed up the water column from bottom to surface), the value of TP could rise up to ~0.7–0.8 μmolTP l^{-1}.

Application of Eq. 2.8 to two time periods relating to the situation illustrated in Fig. 2.38, viz. (i) prior to the cyclone arrival, and (ii) the onset of *chl* maximum response has shown that the calculated value of *chl* proved to be, respectively, 0.58, and 0.97 μg l^{-1} as compared to the remotely retrieved values of *chl* (0.6 μg l^{-1} and 1.0 μg l^{-1}).

Thus, we believe that this example supports our interpretation of the nature/mechanism of the revealed from space surface *chl* modulations as an aftermath of the cyclone passage and the ensuing water column vertical mixing.

Therefore, in capsule, the first type response cases should be related to cyclone-induced pumping of nutrient-rich waters of Atlantic origin to the water surface followed by a relatively short-living enhancement of phytoplankton productivity in the upper layers lasting until the depletion of pools of nutrients brought up from below. The described sequence is illustrated in Fig. 2.33 (plates a–d).

This type of response can be expected to occur within the vast area of Atlantic waters propagating across the southern and central BS (see Fig. 2.34). This explains the prevalence of the first type response cases over cases exhibiting the response of the second type.

Observed by us only on limited occasions, the second type of response is thought to be associated with the situations when some cyclones propagating generally from south to north across the BS eventually reach the PF (Polar Front) (whose position is illustrated in Fig. 2.35 for a specific year). If upon coming across the PF zone (compare Figs. 2.35 and 2.39, plate b), the cyclone trajectory overlaps with the BS currents of Atlantic origin, a sequence of dynamic processes unfolds. The water of Atlantic origin (its SST profile is illustrated in the right hand side of plate c, Fig. 2.39) plunges under the surface layers of Arctic water—the phenomenon well established for the BS (The Barents Sea 2011). Because of the subduction, warmer and nutrient richer waters found themselves beneath a "blanket" of cold Arctic waters. With the arrival of the cyclone, the submerged Atlantic water finds itself brought up to the surface due to the aforementioned Ekman pumping mechanism.

Within 1–2 days (plate **a** in Fig. 2.39) the propulsion of submerged waters is manifested in Fig. 2.34 (plate **a**) through the enhancement of both *chl* and SST. However, within a few days this temporary dual increase begins dilapidating to eventually return to the initial thermal and biological situation (point A in plate **a**, Fig. 2.39). We don't have any substantiated explanation for the minima in *chl* and SST that occurred on the seventh day in that specific example. In other observed cases of the second type response this feature did not appear.

The results obtained from the present study indicate that the passage of cyclones at high northern latitudes (with the BS as an example) results in a temporary enhancement of phytoplankton *chl*, which is widely considered as a proxy of the primary productivity level (e.g. Kirk 1983).

The common features are: (i) cyclones modify the thermal and hydrobiological 2D fields along the footstep trajectory, (ii) the major impact is produced by cyclones with the highest depression depth and low translation speed, (iii), a more intense surface *chl* enhancement (up to 25%) was observed in the right-hand side of the footprint stripe as supported by previous studies for the northern hemisphere (e.g. Son et al. 2007).

In the case of high latitudes, the major specific features are as following: (i) there are two types of response to cyclone's impact in the BS: the surface *chl* can increase, but, in some specific instances, decrease, while SST can remain either nearly intact or even increase, (ii) the surface *chl* and SST increase is a rather short-term phenomenon (its duration is between a few days and, a fortnight), (iii) the absolute values of cyclone-induced Δchl and, especially ΔSST are much lower than those generally reported for low latitudes (see Sect. 2.2.3.3). However, this general statement does not imply a close similarity between the major features of response of high and low latitude waters to cyclone impacts as it is demonstrated in the brief review above.

Regarding the total seasonal impact of cyclones on PP in the BS, it should be born in mind that (i) the number of cyclones per vegetation season prone to studying by ocean colour sensors proved to be generally about 2–3 or even less (as compared to the total seasonal number), (ii) the *chl* increase due to the cyclone impact varies in rather wide limits (on average, constituting 0.2 $\mu g\ l^{-1}$ and never

surpassing ~ 0.4 μg l^{-1}), (iii) the average cumulative area covered by a translating footprint generally accounts for about 14% of the Barents Sea area. Also it should be taken into account that the rate of PP is sensibly less in the footprint cloudy areas than in sunlit areas in the wake of the translating cyclone.

All these limitations/uncertainties do not permit to make any quantified assessment of the actual impact of cyclones on PP of the BS based solely on 23 cases. However on a qualitative level, our data seem to imply that cyclones are hardly essential boosters of PP in the BS.

A further substantiation of the above corollary concerning the influence of cyclones on *chl* was obtained through a dedicated correlation analysis performed for 96 cyclones that occurred during the vegetation period over the time period of 11 years (see Fig. 2.35). The repartition of 96 cyclones across the spaceborne observation period was compared with the respective interannual variations of *chl* obtained by us from satellite data and averaged over the ice-free BS area. This analysis has yielded the value of the coefficient of correlation as low as 0.35 (the level of significance $p > 0.1$).

We believe that because the analyzed data include not only the cases prone to optical remote sensing (i.e. relatively cloud-free 23 cases), but also cloudy cases unattainable for optical remote sensing, the results thus obtained reflect more amply the cause and effect correspondence we are looking to. That is why we believe that it is a more robust argument in favour of our above assumption that the interannual variations in *chl* across the BS can be only peripherally affected by passing cyclones. Obviously, other multiple forcing factors collectively control the observed interannual variations in *chl* averaged over the BS.

It could be conjectured that the same conclusion can be made with respect to the pelagic Arctic tracts, which are generally even less productive than the Barents Sea (Petrenko et al. 2013), and for which cloudiness during the vegetation season is very frequent, heavy and extends over immense areas. However, this supposition certainly requires further studies in order to advance our understanding of the actual role of cyclones in modulations of the Arctic Ocean productivity and ecosystem functioning.

References

Akmaykin, D. A., Bukin, O. A., Permyakov, P. A., and Salyuik, P. A. (2013) Assessments of the tropical cyclone influence on chlorophyll-a fields in some regions of the Pacific. In: *Proceedings of the Remote Sensing of Environment: Scientific and Applied Research in Asia-Pacific International Conference (RSAP2013), 24–27 September 2013, Vladivostok, Russia, Publ. Institute of Automation and Control Process, Far eastern Branch, Russian Academy of Sciences*. p. 33.

Airoldi, L., and Beck, M.W. (2007) Loss, status and trends for coastal marine habitats of Europe. *Oceanographical Marine Biological Annual Review* **45**, 347–407.

Amon, R.M.W., and Spitzy, A. (1999) Distribution of dissolved organic carbon during estuarine mixing in the southern Kara Sea. *Berichte zur Polarforschung* **300**, 102–109.

Anonymous. (2005) Reanalyzed data on world-wide precipitation. GPCC website Applications. *Journal of Geophysical Research* **111**, Co3011.

Anonymous (2007) Spatial plan for special purpose coastal zone. (Karajovic, S. Ed.). Kotor-Podgorica: RZUP Republic Institute for Urban Planning and Development. 186 p.

Arrigo, K., and van Dijken, G. (2011) Secular trends in Arctic Ocean net primary production. *Journal of Geophysical Research* **116** (C09011), 1–1 5. doi:10.1029/2011JC007151.

Asknes, D. L., Nejstgaard, J. E., Sædberg, E., and Sørnes, T. (2004) Optical control of fish and zooplankton populations. *Limnology and Oceanograthy* **49**, 233– 238.

Aubry, B., Bertonm A., Bastianinin, M., Socal, G., and Acri, F. (2004) Phytoplabnkton succession in a coastal area of the NW Adriatic, over a 10-year sampling period (1990–1999). *Continental Shelf Reseach* **24**, 97–115.

Babin, S. M., Carton, J. A., Dickey, T. D., and Wiggert, J. D. (2004) Satellite evidence of hurricane-induced phytoplankton blooms in an oceanic desert. *Journal of Geophysical Research* **109**, C03043, doi:10.1029/2003JC001938.

Balestra, B. Maria Marino, M., Simonetta Monechi, Chiara Marano, C., and Francesco Locaiono, F. (2008) Coccolithophore Communities in the Gulf of Manfredonia (Southern Adriatic Sea): Data from Water and Surface Sediments. *Micropaleontology* **54**(5), 377–396.

Bardan, S.I., and Korneeva, G.A. (2006) Interseasonal tendencies of transformation of organic carbon and phermentic activity of water medium in wintertime in Russian Arctic seas on the example of Yenisey River estuary. In: Romankevich, E.A., Vetrov, A.A. (Eds.) *Carbon cycle in Russian Arctic seas, Biological Series* **6**. Moscow: *Izvestia RAN*, pp. 731–745.

Bauch, D., Erlenkeuser, H., Stanovoy, V., Simstich, J., and Spielhagen, R. F. (2003) Freshwater distribution and brinewaters in the southern Kara Sea in summer 1999 as depicted by $\delta^{18}O$ results. *In*: *Siberian river run-off in the Kara Sea* (Eds.R. Stein, K. Fahl, D. K.Fuellerer, E. M. Galimo, and O. V. Stepanets). Amsterdam: Elsevier Science B. V. pp. 73–90.

Bianchi, C. N., and Morri, C. (2000) Marine biodiversity of the Mediterranean Sea: Situation and Prospects for future Research. *Marine Pollution Bulletin* **40**(5), 367–676.

Bukata, R. P., Jerome, J. H., Kondratyev, K. Ya., and Pozdnyakov, D. V. (1995) *Optical Properties and Remote Sensing of Inland and Coastal Waters.* Boca Raton e.a.: CRC Press, 362 pp.

Byju, P., and Kumar, P. S. (2011). Physical and biological response of the Arabian Sea to tropical cyclone Phyan and its implications. *Marine Environmental Research* **71**(5), 325–330.

Carroll, J. Savinov, L., Christensen, V., Blakely, G., Petterssen, P., Sorensen, L., Kjelstad, K., Kohler, B., Spitzy, H., and Hessen, A.D. (2004) Material fluxes from the Russian rivers Ob and Yenisey: interactions with climate and effects on Arctic Seas (MAREAS). *Berichte zur Polarforchung* **479**, 103–113.

Castaing, P., and Allen, G. P. (1981) Mechanisms Controlling Seaward Escape of Suspended Sediment from the Girone: A Macrotidal Estuary in France. *Marine Ecology* **40**, 101–118.

Castaing, P. P., Froidefond, J. M., Lazure, P., Weber, O., Prudhomme, R., and Jouanneau, J. M. (1999) Relationship Between Hydrology and Seasonal Distribution of Suspended Sediments on the Continental Shelf of the Bay of Biscay. *International Council for the Exploration of the Sea* **46**, 1979–2001.

Chen, Y., and Tang, D.L. (2012) Eddy-feature phytoplankton bloom induced by a tropical cyclone in the South China Sea. *International Journal of Remote Sensing* **33**(23), 7444–7457.

Ciavola, P., Mantovani, SimeOni, U., and Tessari, U. (1999) Relation between river dynamics and coastal changes in Albania: as assessment integrating satellite imagery with historical data. *International Journal of Remote Sensing* **20**(3), 561–584.

Colombo, G. (Ed) (1992) *Marine Eutrophication and pollution dynamics: the 25th European Marine Biology Symposium*. Institute of Zoology, University of Ferrara, Olsen & Olsen Pub.

Correggiari, A., Field, M.E., and Trincardi, F. (1996) Late Quaternary transgressive large dunes on the sediment-starved Adriatic shelf. In: De Batist, M., Jacobs, P. (Eds.). *Geology of Siliciclastic Shelf Seas. Geological Society Special Publication* **117**, 155–169.

Cozzi, S., and Giani, M. (2011) River water and nutrient discharges in the Northern Adriatic Sea: Current importance and long-term changes. *Continental Shelf Research* doi:10.1016/j.csr.2011.08.010.

Cushman-Roisin, B., Gačić, M., Poulain, M., and Artegiani, A. (2013) *Physical Oceanography of the Adriatic Sea: past, present and future*. Luwer Academic Publishers: Dordrecht/Boston/London. 245 p.

Dobrovolsky, A. D., and Zalogin, B.S. (1982) *Seas of the USSR*. MGU Pub. Moscow. 198 p.

Druzhkov, N.V., and Druzhkova, E.I. (1999) The composition and distribution of the microplankton community in the Saint Anna trough area. *Berichte zur Polarforschung* **342**, 68–76.

Ecosystem Barents Sea, Egil Sakshaug, Geir Johnsen og Kit Kovacs (eds.), Tapir Academic Press, Trondheim 587 pp., ISBN: 9788251924610.

Engelsen, O., Hegseth, E. N., Hop, H., Hansen, E., and Falk-Peterson, S. (2002) Spatial variability of chlorophyll-a in the Marginal Ice Zone of the Barents Sea, with relations to sea ice and oceanic conditions. *Journal of Marine Systems* **35**, 79–97.

Fain, A. M. V., Ogston, A. S., and Sternberg, R. W. (2007) Sediment transport event analysis on the western Adriatic continental shelf. *Continental Shelf Research* **27**, 431–451.

Fraschetti, S., Bianchi, C.N., Terlizzi, A., Fanelli, G., Morri, C., and Boero, F. (2001) Spatial variability and human disturbance in shallow subtidal hard bottom assemblages: a regional approach. *Marine Ecology Progress Series* **212**, 1–12.

Froidefond, J.-M., Lavender, S., Laborde, A., and Lafon, V. (2002) SeaWiFS Data Interpretation in a Coastal Area in the Bay of P. Biscay. *International Journal of Remote Sensing* **23**, 881–904.

Garcia-Soto, C., and Pingree, R. D. (2009) Spring and Summer Blooms of Phytoplankton (SeawiFS/MODIS) along a Ferry Line in the Bay of Biscay and Western English Channel. *Continental shelf research* **29**, 1111–1122.

Gaye-Haake, B., Unger, D., Nothig, E.-M., Okolodkov, Y. U., Hahl, K., and Ittekkt, V. (2003) Particle fluxes from short-term sediment trap deployments in late summer in the southern Kara Sea. In: *Siberian River Run-off in the Kara Sea. Characterisation, quantification, variability and environmental significance* (Eds. R. Stein, K. Fahl, D. K. Futterer, E. Galimov and O. Stepanets). Amsterdam: Elsevier, pp. 309–328.

Gebhardt, A.C., Gaye-HaaGke, B., Unger, D., Lanajnar, N., and Ittekkot, V. (2004) Recent particulate organic carbon and total suspended matter fluxes from the Ob and Yenisey rivers into the Kara Sea (Siberia). *Marine Geology* **207**, 225–245.

Giakoumi, S., Cebrian, E., Kokkoris, G.D., Ballesteros, E., and Sala, E. (2012) Relationships between fish, sea urchins and macroalgae: The structure of shallow rocky sublittoral communities in the Cyclades, Eastern Mediterranean. *Estuarine Coastal and Shelf Science* **109**, 1–10.

Giani, M., Djakovac, T., Degobbs, D., Cozzi, S., Solidoro, C., and Umani, S. F. (2012) Recent changes in the Marine ecosystems of the northern Adriatic Sea. *Estuarine, Coastal and Shelf Science* **115**, 1–13.

Gonzalez-Pola, C., A. Lavin, and M. Vargas-Yañez. (2005) Intense Warming and Salinity Modification of Intermediate Water Masses in the Southeastern Corner of the Bay of Biscay for the Period 1992–2003. *Journal of Geophysical Research* **110**, C05020.

Grassl, H., Pozdnyakov, D.V., Korosov, A.A., Doerrfer, R., Gordeev, V.V., and Makarevich, P.R. (2007) *MERIS-Based Assessment of Carbon Supply into the Arctic by River RunOff*. Final Report to INTAS. Project Ref. 06-1000025-9142.

Guillaud, J.-F., Aminot, A., Delmas, D., Gohin, F., Lunven, M., Labry, C., and Herbland, A. (2008) Seasonal Variation of Riverine Nutrient Inputs in the Northern Bay of Biscay (France), and Patterns of Marine Phytoplankton Response. *Journal of Marine Systems* **72**, 309–319.

Hanshaw, M.N., Lozier, M.S., and Palter, J.B. (2008) Integrated impact of tropical cyclones on sea surface chlorophyll in the North Atlantic. *Geophysical Research Letters* **35**, LOl60 l.

ICES. (2010) Report of the ICES Advisory Committee, 2010. ICES Advice, 2010. Book **7**, 30–67.

International Hydrographic Organization. (1971) *Limits of Oceans and Seas*. 3rd ed., corrected. 13. Monte-Carlo: IMP Monegasque.

Jullien, S., C. E. Menkes, P. Marchesiello, *et al*. (2012) Impact of tropical cyclones on the heat budget of the Southern Pacific Ocean. *Journal of Physical Oceanography* **42**, 11,1882–11,1906.

Kawai, Y., and Wada, A. (2011) Detection of cyclone-induced rapid increases in chlorophyll-a with sea surface cooling in the northwestern Pacific Ocean from a MODIS/SeaWiFS merged chlorophyll product. *International Journal of Remote Sensing* **32**(24), 9455-9471.

Kirk, J. T. O. (1983) *Light and Photosynthesis in Aquatic Ecosystems*. Melbourn, Australia: Cambridge University Press. 401 p.

Köhler, H., Meon, B., Gordeev, V., Spitzy, A., and Amon, R. (2003) Dissolved organic matter (DOM) in the estuaries of Ob and Yenisei and the adjacent Kara Sea, Russia. In: *Siberian River Run-off in the Kara Sea. Characterisation, quantification, variability and environmental significance* (Eds. R. Stein, K. Fahl, D. K. Futterer, E. Galimov and O. Stepanets). Amsterdam: Elsevier. pp. 28–308.

Komar, P.D., and Miller, M.C. (1975) Sediment threshold under oscillatory waves. In: *Proceedings of the 14th Conference on Coastal Engineering*, pp. 756–775.

Korosov, A. A., Pozdnyakov, D., and Grassl, H. (2011) Speceborne quantitative assessment of dissolved organic carbon fluxes in the Kara Sea. *Advances in Space Research. Special Issue: Oceanography and Cryosphere* doi:10.1016/j.asr.2011.10.008.

Lammers, R. B., Shiklomanov, A. I,,Vorosmarty, C. J., Fekete, B. M., and Peterson, B. J. (2001). Assessment of contemporary Arctic river runoff based on observational discharge records. *Journal of Geophysical Research* **106**(D4), 3321–3334.

Lampert, L., Queguiner, B., Labasque, T., Pichon, A., and Lebreton, N. (2002) Spatial Variability of Phytoplankton Composition and Biomass on the Eastern Continental Shelf of the Bay of Biscay (North-East Atlantic Ocean). Evidence for a Bloom of *Emiliania huxleyi* (Prymnesiophyceae) in Spring 1998. *Continental Shelf Research* **22**, 1225–47.

Larionov, V.V., and Kodina, L.A. (2000) Phytoplankton of the Ob and Yenisey transects. *Berichte zur Polarforschung* **360**, 36–42.

Larionov, V.V., and Makarevich, P.R. (2000) The taxonomic and ecological descriptions of the phytoplankton assemblages from the Yenisey Bay and adjacent waters of the Kara Sea on September. *Berichte zur Polarforschung* **393**, 48–62.

Lavender, S. J., Raitsos, D. E., and Pradhan, Y. (2008) Variations in the phytoplankton of the North-Eastern Atlantic Ocean: From the Irish Sea to the Bay of Biscay. In: *Remote Sensing of the European Seas.* Eds. V. Barale, and M. Gade, 67–78. Dordrecht: Springer Science + Business Media B.V.

Lavrentieva, G.M., and Bulion, V.V., (Eds.) (1984) *Methodological Recommendation on Collection and Processing of Samples for Hydrobiological Research in Fresh Waterbodies. Phytoplankton and its Production*. Leningrad: GOSNIORH Publ.

Le Fouest, V., Postlethwaite, C., Marqueda, M. A. M., Belanger, S., and Babin, M. (2011) On the role of tides and strong wind events in promoting primary production in the Barents Sea. *Continental Shelf Research* **31**, 1869–1879.

Leipper, D. F. (1967) Observed ocean conditions and hurricane Hilda. *Journal of Atmospheric Sciences* **24**, 182–196.

Lin, I. (2012) Typhoon-induced phytoplankton blooms and primary productivity increase in the western North Pacific subtropical ocean. *Journal of Geophysical Research* **117**, C03039.

Lin, I., Liu, W.T., Wu, C.-C., Wong, G.T.F., Hu, C., Chen, Z., Liang, W.-D., YANG,Y., and Liu. K.-K. (2003) New evidence for enhanced ocean primary production triggered by tropical cyclone. *Journal of Geophysical Research Letters* **30**(13),1718–1723, doi:10.1029/2003GL017141.

Ludwig, W., Dumont, E., Meybeckred, M., and Heussner, S. (2009) River discharges of water and nutrients to the Mediterranean and Black Sea: Major drivers for ecosystem changes during past and future decades? *Progress in Oceanology* **80**(3–4), 199–217.

Makarevich, P.R., and Larionov, V.V. (1999) Floristic composition and productivity of the microalgal communities of the Ob Bay and the Yenisei Bay in summer. *Berichte zur Polarforschung* **393**, 34–47.

Manca, B. B., Budillon, G., Scarazzato, P. and Ursella, L. (2003) Evolution of dynamics in the eastern Mediterranean affecting water mass structures and properties in the Ionian and Adriatic Seas. *Journal of Geophysical Research* **108**(C9). doi:10.1029/2002JC001664.

Martin, L. J., Quinn, J. E., Ellis, E. C., Shaw, M. R., Dorning, M. A., Hallett, L. M., Heller, N. E., Hobbs, R. J., Kraft, C. E., Law, E., Michel, N. L., Perring, M. P., Shirey, P. D., and Wiederholt, R. (2014) Conservation opportunities across the world's anthromes. *Diversity and Distributions* **20**, 745–755.

Matishov, G. G., and Pavlova L. G. (1990) *General Ecology of Polar Oceans*. Leningrad: Nauka Publishing (in Russian). 259 p.

Mistri, M., and Rossi, R. (2001) Structure and secondary production in a shallow lagoon (north-eastern Italy). *Estuarine, Coastal and Shelf Science* **52**(5), 605–616.

Morozov, E., Pozdnyakov, D., Smyth, T., Sychev, V., and Grassl H. (2012) Spaceborne study of seasonal, multi-year and decadal phytoplankton dynamics in the Bay of Biscay: geophysical forcing at different time and space scales. *International Journal of Remote Sensing* **34**(4), 1297–1331.

Morozov E., Kondrik, D., Fedorova, A., Pozdnyakov, D., Tang, D., and Pettersson, L. (2014). A spaceborne assessment of cyclone impacts on the Barents Sea surface temperature and chlorophyll. *International Journal of Remote Sensing* **36**(7), 1921–1941.doi:10.1080/01431161.2015.1029098.

Naumov, A.D., and Fedyakov, V.V. (1993) *The Eternally Alive White Sea*. St. Petersburg: St. Petersburg University Publ. 88 p. (in Russian).

NOAA ATLAS. (2004) Climatic Atlas of the Arctic Seas 2004. ftp://ftp.nodc.noaa.gov/pub/data.nodc/woa/PUBLICATIONS/english58.pdf.

Nöthing, E.-M., Okolodkov, Yu., Larionov, V., and Makarevich, P. (2003). Phytoplankton distribution in the inner Kara Sea: a Comparison of three summer investigations. In: *Siberian River Run-off in the Kara Sea. Characterisation, quantification, variability and environmental significance*, edited by R. Stein, K. Fahl, D. K. Futterer, E. Galimov and O. Stepanets (Amsterdam: Elsevier), pp. 163–183.

Orlic, M., Kuzmic, M., and Pasaric, Z. (1994) Response of the Adriatic Sea to the bora and sirocco forcing. *Continental Shelf Research* **14**(1), 91–116.

Paklar, G. B., Isakov, V., Koracin, D., Kourafalou, V., and Prlic, M. (2001) A case study of bora-driven flow and density changes on the Adriatic Shelf (January 1987). *Continental Shelf Research* **21**, 1751–1783.

Parker. A. (2014) Present contributions to sea level rise by thermal expansion and ice melting and implication on coastal management. *Ocean and Coastal Management* **98**, 202–211.

Petrenko, D. Pozdnyakov, D., Johannessen, J., Counilion, F., and Sychov, V. (2013) Satellite-derived multi-year trend in primary production in the Arctic Ocean. *International Journal of Remote Sensing* **34**(11), 3903–3937.

Pozdnyakov, D.V., and Grassl, H. (2003) *Colour of Inland and Coastal Waters: a methodology for its interpretation*. Chichester: Springer-Praxis, 170 p.

Pozdnyakov, D. V., Korosov, A. A., Grassl, H., and Pettersson, L. H. (2005) An advanced algorithm for operational retrieval of water quality from satellite data in the visible. *International Journal of Remote Sensing* **26**, 2669–2687.

Puillat, I., Lazure, P., Jégou, A. M., Lampert, L., and Miller, P. I. (2004) Hydrographical Variability on the French Continental Shelf in the Bay of Biscay, during the 1990s. *Continental Shelf Research* **24**, 1143–1163.

Raiucich, F. (1994) Note on the flow rates of the Adriatic rivers. Taskana, Italy: Technical Report RF 02. 60 pp.

Raiucich, F. (1996) On the fresh balance of the Adriatic Sea. *Journal of Marine Systems* **9**, 305-319. 10.1016/S0924-7963(96)00042-5.

Rao, K.H., Smith, A., and Ali, M.M. (2006) A study on cyclone induced productivity in south-western Bay of Bengal during November-December 2000 using MODTS (SST and chlorophyll-a) and altimeter sea surface height observations. *Indian Journal of Marine Sciences* **35**(2), 153–160.

Rast, M., Bezy, J. L., and Bruzzi, S. (1999) The ESA Medium Resolution Imaging Spectrometer MERIS: A review of the instruments and its mission. *International Journal of Remote Sensing* **20**(9), 1681–1702.

Redfield, A. C. (1934) On the proportions of organic derivations in seawater and their relation to the composition of plankton. In: *James Johnstone Memorial Volume*, (ed. R. J. Daniel). University Press of Liverpool, pp. 177–192.

Reigstad, M., Wassmann, P., Riser, C., Oygarden, W. S., and Rey, F. (2002) Variations in hydrography, nutrients and chlorophyll-*a* in the marginal ice-zone and central Barents Sea. *Journal of Marine Systems* **38**, 9–29.

Robinson, I.S. (2004) *Measuring the oceans from space. The principles and methods of satellite oceanography*. Springer-Praxis. 675 pp.

Rodriguez, F., Varela, M., Fernandez, E., and Zapata, M. (2003) Phytoplankton and pigment distributions in an anticyclonic slope water oceanic eddy (SWODDY) in the southern Bay of Biscay. *Marine Biology* **143**, 995–1011.

Sailot, A. (Ed.) (2005) *The Mediterranean Sea*. Heidelberg: Springer-Verlag Pub. 414 p.

Salyuk, P. A., Golik, I. A., and Stepochkin, I. E. 2014. Tropical cyclones influence on bioproductivity of the North-Western Pacific. *Asia-Pacific Journal of Marine Science and Education*. **4**(1): 111–117.

Sarangi, R. K. (2011) Impact of Cyclones on the Bay of Bengal Chlorophyll Variability Using Remote Sensing Satellites. *Indian Journal of Geo-Marine Sciences* **40** (6), 794–80I.

Siswanto, E., Ishizaka, J., Toratani M., Hirawake, T., and S.-I. Saitoh. (2007) The Effect of Tropical Cyclone on the Primary Production Enhancement: Some Results from the W-PASS (Western Pacific Are-Sea Interaction Study) Project. In: *Proceedings of the PICES MONITOR/BIO Workshop 5, October 27*, edited by E. A. Pakhomov and O. Yamamura. Vladivostok: Biological Oceanography Committee.

Smith, V. H. (2006) Responses of estuarine and coastal marine phytoplankton to nitrogen and phosphorus enrichment. *Limnology and Oceanography* **51**(I, part 2), 377– 384.

Son, S., Platt, T., Fuentes-Yako, C., Bouman, H., Devred, E., Wu, Y., and Sathyendranath, S. (2007) Possible biogeochemical response to the passage of Hurricane Fabian observed by satellites." *Journal of Plankton Research* **29**(8), 687–697.

Somavilla, R., Gonzalez-Pola, C., Rodriguez, C., Josey, S. A., Sanchez, R. F. and Lavin, A. (2009) Large Changes in the Hydrographic Structure of the Bay of Biscay after the Extreme Mixing of Winter 2005. *Journal of Geophysical Research* **114**, C01001.

Sterckx, S., Knaeps, E., and Ruddick, K. (2011) Detection and correction of adjacency effects in hyperspectral airborne data of coastal and inland waters: the use of the near infrared similarity spectrum. *International Journal of Remote Sensing* **32**(21), 6479–6505.

Suhovey V.F. (1986) *Seas of the World Ocean*. Leningrad: Gidrometeoizdat. 288 p. (in Russian).

Surian, N., and Rinaldi, M. (2003) Morphological response to river engineering and management in alluvial channels in Italy. *Geomorphology* **50**, 307–326.

Tang, D., and Sui, G. L. (Eds.) (2014). *Typhoon Impact and Crisis Management*. (Heidelberg e.a. Springer Science+Business Media). 578 p.

The Barents Sea: Ecosystem, Resources, Management. (2011) Eds. Tore Jakobsen and Vladimir K. Ozhin. Tapir Academic Press: Trondheim, Norway. 825 p.

Thiersten, H., and J. Young. (2004) *Coccolithophores – From Molecular Processes to Global Impact*, 3–15. Berlin: Springer-Verlag.

Tyrrell T., and Merico A. (2004) *Emiliania huxleyi*: bloom observations and the conditions that induce them. In: *Coccolithophores–from molecular processes to global impact.*): Berlin: Springer. pp. 585–604.

Volkov, V.A., Johannessen, O.M., Borodachev, V.E. *et al*. (2002) *Polar Seas Oceanography. An integrated case study of the Kara Sea*. Chichester: Springer/Praxis.

Walker, N.D., Leben, R.R., and Balasubramantan, S. (2005) Hurricane-forced upwelling and chlorophyll a enhancement within cold-core cyclones in the Gulf of Mexico. *Geophysical Research. Letters,* **32**, LI8610.

Wang, X. H., and Pinardi, N. (2002) Modeling the dynamics of sediment transport and resuspension in the northern Adriatic Sea. *Journal of Geophysical Research* **107**(C12), 18-1–18-23. doi:10.1029/2001JC001303.

White Sea: its marine environment and ecosystem dynamics influenced by global change (Eds. Nikolay Filatov, Dmitry Pozdnyakov, Ola Johannessen, Lasse Pettersson, Leonid Bobylev). (2005) Chichester: Springer-Praxis, 472 p.

Ying, M., Knutson T. R., Kamahori, H., and Lee, T.-C. (2012) Impacts of climate change on tropical cyclones in the Western North Pacific Basin. Part II: Late twenty-first projections. *Tropical Cyclone Research and Review* **1**(2), 231–241.

Zavatarelli, M., Pinardi, N., Kourafalou, V.H., and Maggiore, A. (2002) Diagnostic and prognostic model studies of the Adriatic Sea general circulation: seasonal variability. *Journal of Geophysical Research* **107** (C1), 3004, 10.1029/2000JC000210.

Zhao, H., and Tang, D. L. (2006). The Spatial Distribution of Chlorophyll-a and Its Responses to Oceanographic Environments in the South China Sea." *Advances in Geosciences* **5**, 7– 14.

Zhao, H., Tang, D. L., and Wang, Y. (2008) Comparison of Phytoplankton Blooms Triggered by Two Typhoons with Different Intensities and Translation Speeds in the South China Sea. *Marine Ecology Progress Series* **365**, 57–65. doi:10.3354/meps07488.

Zhao, H., Tang, D. L., and Wang, D. (2009) Phytoplankton Blooms near the Pearl River Estuary Induced by Typhoon Nuri. *Journal of Geophysical Research* **114**, C12027. doi:10.1029/2009JC005384.

Zheng, G. M., and Tang, D. L. (2007) Offshore and Nearshore Chlorophyll Increases Induced by Typhoon Winds and Subsequent Terrestrial Rainwater Runoff. *Marine Ecology Progress Series* **333**, 61–74. doi:10.3354/meps333061.

http://www.springer.com/978-3-319-30074-0

Exploring the Marine Ecology from Space
Experience from Russian-Norwegian cooperation
Pozdnyakov, D.V.; Pettersson, L.; Korosov, A.A.
2017, XXXVI, 215 p. 117 illus., 73 illus. in color.,
Hardcover
ISBN: 978-3-319-30074-0